

TECHNISCHE UNIVERSITÄT MÜNCHEN

Lehrstuhl II für Technische Chemie

Phosgene-free Synthesis of Diphenyl Carbonate

Bo Peng

Vollständiger Abdruck der von der Fakultät für Chemie der Technischen Universität
München zur Erlangung des akademischen Grades eines

Doktor-Ingenieurs (Dr.-Ing.)

genehmigten Dissertation.

Vorsitzender: Univ.-Prof. Dr.-Ing. Kai-Olaf Hinrichsen

Prüfer der Dissertation:

1. Univ.-Prof. Dr. techn. Johannes A. Lercher
2. Univ.-Prof. Dr. mont. Dr. rer. nat. h. c. Ewald Werner

Die Dissertation wurde am 22.12.2015 bei der Technischen Universität München
eingereicht und durch die Fakultät für Chemie am 12.04.2016 angenommen.

天行健，君子以自强不息。地势坤，君子以厚德载物。

Heaven moving forward and forever, superior person shall accomplish excellence with perseverance. Earth featuring vast and grand, superior person shall embrace objects with virtues.

——《易经》

— *Classic of Changes*

«Мне не нужны доказательства. Законы природы исключений не терпят и этим явно отличаются от правил и правильностей, подобных, например, грамматическим.»

“I have no need of proof. The laws of nature, unlike the laws of grammar, admit of no exception.”

— *Дмитрий Иванович Менделеев*

— *Dmitri Ivanovich Mendeleev*

谨以本论文纪念我已故的外祖父母黄蕴璞先生（1921 ~ 1980）和姚同玉女士（1922 ~ 2011）。

The present thesis is sincerely dedicated to the memory of my beloved maternal grandparents, Mr. Yunpu Huang (1921 ~ 1980) and Mrs. Prof. Tongyu Yao (1922 ~ 2011), who passed away too early to witness the completeness of my doctoral work.

彭博

Bo Peng

2015 年 8 月

August 2015

Acknowledgement

First, my sincere appreciation is expressed to the supervisor of my doctoral work, Prof. Dr. Johannes A. Lercher. Thank you for offering me a position in your international research group and giving me the opportunity to work on challenging and interesting project. During these years, your warm encouragement and thoughtful guidance have always enlightened me. You taught me a lot not only with wisdom and knowledge, but also with maturity of conducting.

I am very grateful to senior scientist Dr. Erika E. Ember. Thank you for your efforts on coordination of every project-related activity and correction of every project-related document. The discussions with you throughout my doctoral work, on the topics of science, food, religion and cat, are really memorable. Furthermore, thank you for all your helps during my adaptation to the culture of Central Europe. I am gratitude especially to your respect on cultural tradition from another continent.

Inside the small team of “small molecule activation”, a close and successful collaboration has been made, owing to the efforts from everybody in the team. Dr. Anastasia V. Pashigreva, Dr. Jieli He, Claudia B. Himmelsbach, Navneet K. Gupta and Benjamin Felkel are acknowledged for their supports and inputs in my work.

Senior members in Chair II of Chemical Technology, both scientific and non-scientific, are important for the smooth and efficient running of organization, supervision, administration, *etc.* Prof. Dr. Andreas Jentys, Prof. Dr. André van Veen, Prof. Dr. Chen Zhao, Dr. Oliver Y. Gutiérrez and Dr. Maricruz Sanchez are acknowledged for their scientific inputs. Franz-Xaver Hecht, Martin Neukamm and Andreas Marx are acknowledged for their technical supports. Stefanie Seibold, Helen Brenner, Heidemarie Hermann, Katharina Thies, Bettina Federmann, Karen Schulz and Ulrike Sanwald are acknowledged for their administrative helps.

A friendly and cooperative circumstance is always positive for office and laboratory. Dr. Herui Dou, Dr. Jeongnam Kim, Dr. Luis F. Gonzalez-Peña, Dr. Yue Liu, Dr. Wenhao Luo, Dr. Hui Shi, Dr. Stefan Schallmoser, Dr. Maximilian W. Hahn, Murat Küçükdişli and Sebastian Müller are acknowledged for scientific discussions. Dr. Despina Tzoulaki, Dr. Yanzhe Yu, Dr. Sonja Wyrzgol, Dr. Baoxiang Peng, Dr. John Ahn, Dr. Sarah Maier, Dr. Christian Gärtner, Dr. Xianyong Sun, Dr. Stefanie Simson, Dr. Robin Kolvenbach, Dr. Yuchun Zhi, Dr. Nathan Hould, Daniela Hartmann, Jennifer Hein, Linus Schulz, Yuanshuai Liu, Edith Berger, Yu Lou and Marco Peroni are acknowledged for supportive helps in the lab. Dr. Lin Lin, Dr. Wenji Song, Dr. Udishnu Sanyal, Dr. Ricardo Bermejo de Val, Monica Markovits, Moritz Schreiber and Kai Sanwald are acknowledged for being good officemates.

In an international research group, without going into details, all following colleagues in Chair of Chemical Technology II are acknowledged for sharing their time with me. Prof. Dr. Xuebing Li, Dr. Yongzhong Zhu, Dr. Roberta Olindo, Dr. Eszter Baráth, Dr. Márta Dömök, Dr. Elena Kondratieva, Dr. Vishnuvarthan Muthusamy, Dr. Yulia Martynova, Dr. Michael Salzinger, Dr. Tobias Förster, Dr. Sabine Scholz, Dr. Florian Schüller, Dr. Ana Hrabar, Anna Lubinus, Eva Schachtl, Phillip Wallis, Elisabeth Hanrieder, Pamina Andrä Sebastian Grundner, Tobias Berto, Sebastian Foraita, Stanislav Kasakov, Sebastian Eckestein, Manuel Wagenhofer, Martina Braun, Guoju Yang, Yang Song, Peter Hintermeier, Sylvia Albersberger, Matthias Steib, Daniel Melzer, Andreas Ehrmaier, Wanqiu Luo, Takaaki Ikuno and Ferdinand Vogelgsang together with our external members – visiting scholars, Prof. Dr. Gary Haller, Prof. Dr. Mirosław Derewiński, Prof. Dr. Xiangyun Guo, Dr. Rino Mukti and Dr. Bruno Dalla Costa, thank you all!

External experimental supports from Division of Physical Chemistry and Chair I of Chemical Technology are acknowledged. Prof. Dr. Sebastian Günther, Dr. Florian Schweinberger, Dr. Robert Reichelt and Dr. Cornelia Ablasser, thank you for your

contributions. I am impressed by your scientific and technical expertise as well as your patience during the time of my measurements.

The work packages of INCAS project from European Commission are acknowledged for financial support and opportunity given to young scientists. The young scientists involved in INCAS project, Dr. Katia Barbera, Dr. Salvatore Abate, Dr. Christina Popa, Dr. Miguel Palomino, Leone Frusteri, Alejandro Prieto and Emila Kertalli, are especially appreciated for exchanging scientific ideas. The inputs from industrial partners, Prof. Dr. Leslaw Mleczko, Dr. Stefan Roggan, Dr. Stefan Grasser, Dr. Konstantinos Metaxas, Dr. René Bos, Dr. Herman Kuipers, Dr. Erik Abbenhuis and Dr. Eoghan McAlpine, are also acknowledged.

During my work for doctoral thesis, I have obtained the supplementary supports from my students. They have transferred their talents and enthusiasms into their theses or internship works with me, being extra supports of my work. Dominik Göppert, Jialei Wu, Sandy Lama, Thilo Kögl, Kenny Yeo, Yizhou Shen, Karan Singh, Xaver Müller and Rasyiqah Mohd, thank you all for your contributions!

Last but not least, I want to express my gratitude to my family for their ceaseless encouragements and supports. The scientific suggestion from my paternal grandfather Mr. Acad. Prof. Shaoyi Peng, the mental support and understanding from my parents and parents-in-law, Mr. Li Peng, Mrs. Xiaomu Huang, Mr. Brig. Prof. Qing Pan and Mrs. Xiaoqing Zhang are acknowledged. Finally, I am indebted to my dearest wife, Mrs. Yuan Pan, for the unconditional love, support, encouragement and understanding. I appreciated and will always cherish the time with you. Thank you!

Bo Peng
August 2015

Abstract

Using a mechanistically guided approach, a two-step synthesis route of diphenyl carbonate has been developed, combining methanol carboxylation to dimethyl carbonate with its transesterification with phenol. The equilibrium constraints are overcome by the selective removal of water or methanol using novel zeolite modifications. The catalytic efficiencies of both steps have been advanced based on mechanistic insights gained from kinetic and spectroscopic studies.

Zusammenfassung

Unter Verwendung einer mechanistisch geführten Herangehensweise wurde eine zwei-stufige Syntheseroute von Diphenylcarbonat entwickelt, die über eine Carboxylierung von Methanol zum Dimethylcarbonat führt und dessen Umesterung mit Phenol die Reaktionssequenz abschließt. Die Gleichgewichtslimitierungen wurden durch selektive Abtrennung von Wasser oder Methanol mittels neuer Zeolithmodifikation überwunden. Die katalytische Effizienz beider Schritte wurde durch mechanistische Erkenntnisse weiterentwickelt, die aus kinetischen und spektroskopischen Untersuchungen gewonnen wurden.

Table of contents

Introduction	1
1.1 Polycarbonates	2
1.2 Brief history of PCs production	2
1.3 Principal synthetic route for PCs production	3
1.4 Alternative pathways for sustainable PCs production	5
1.4.1 Overview of possible routes.....	5
1.4.2 Catalytic DMC synthesis from methanol and CO ₂	9
1.4.3 Catalytic DPC synthesis from phenol and DMC	12
1.4.4 Zeolites as solid state sorbents	16
1.4.5 Molecular diffusion in zeolites	18
1.5 Main challenges and opportunities on sustainable DPC synthesis	19
1.6 Scope of the thesis	21
1.7 References.....	22
Rate enhancement of DMC formation from methanol and CO₂ over ZrO₂-based catalysts by heteroatom doping	27
2.1 Introduction.....	28
2.2 Experimental	31
2.2.1 Catalyst preparation	31
2.2.2 Catalytic reaction	32
2.2.3 Catalyst characterization	33
2.3 Results.....	37
2.3.1 Physico-chemical properties of ZrO ₂ -based catalysts.....	37
2.3.2 Catalytic DMC formation over ZrO ₂ -based catalysts	44
2.4 Discussion	56
2.5 Conclusion	63
2.6 References.....	64

2.7 Appendix	66
2.7.1 Raman spectroscopy of different ZrO ₂ -based catalysts	66
2.7.2 N ₂ physisorption of synthesized catalysts	67
2.7.3 Representative XPS spectra of synthesized ZrO ₂ -based catalysts	68
2.7.4 LAS concentration on ZrO ₂ -based catalysts determined by IR spectra of adsorbed pyridine	69
2.7.5 Determination of reaction orders on different ZrO ₂ -based catalysts	69
2.7.6 Stability test for MgO-ZrO ₂ catalyst under different conditions	70
2.7.7 Results of ICP-OES measurements	71
2.7.8 Activity comparison of different ZrO ₂ phases	72
2.7.9 Characterization of surface Lewis acidic sites on ZrO ₂ and MgO-ZrO ₂ catalysts	73
2.7.10 Change on surface hydroxyl group during methanol adsorption	75
2.7.11 Experimental evidence of water formation during MMC formation	75
2.7.12 Rate expression derivation of different elementary steps	76
2.7.13 Calorimetric study on rate determining steps	84
2.7.14 References in Section 2.7	85

Mechanism of MoO₃ catalyzed transesterification of DMC with phenol: evidence for highly active nanocrystalline phase for selective DPC formation

3.1 Introduction	87
3.2 Experimental	90
3.2.1 Catalysts preparation	90
3.2.1.1 Preparation of MoO ₃ -based catalysts on different supports	90
3.2.1.2 Preparation of MoO ₃ /SiO ₂ catalysts with different MoO ₃ loadings ..	90
3.2.1.3 Preparation of 20 wt. % MoO ₃ /SiO ₂ catalysts at different calcination temperatures	90
3.2.2 Catalytic reaction	91
3.2.3 Catalyst characterization	91
3.3 Results	93

3.3.1 Physico-chemical properties of MoO ₃ catalysts	93
3.3.2 MoO ₃ -catalyzed transesterification of DMC with phenol	98
3.4 Discussion	107
3.5 Conclusion	115
3.6 References	115
3.7 Appendix	117
3.7.1 N ₂ physisorption.....	117
3.7.2 Kinetic analysis.....	117
Optimization of a two-step process for the phosgene-free DPC production	122
4.1 Optimization of DMC synthesis from methanol and CO ₂ using a selective water removal agent.....	123
4.1.1 Introduction.....	123
4.1.2 Experimental	125
4.1.2.1 Structural and composition analysis	125
4.1.2.2 Adsorption isotherms	125
4.1.2.3 Diffusion kinetics.....	127
4.1.2.4 Catalyzed DMC synthesis from methanol and CO ₂	128
4.1.3 Results.....	130
4.1.3.1 Adsorption isotherms	130
4.1.3.2 Diffusion kinetics.....	134
4.1.3.3 Catalyzed DMC synthesis from methanol and CO ₂	139
4.1.4 Discussion	141
4.1.5 Conclusion	143
4.2 Reaction optimization of DPC synthesis from phenol and DMC by <i>in-situ</i> methanol removal.....	144
4.2.1 Introduction.....	144
4.2.2 Experimental	146
4.2.2.1 Direct measurements of mass transportation at high temperature ...	146
4.2.2.2 Catalytic reaction	147

4.2.2.3 Characterization of zeolitic sorbents.....	147
4.2.3 Results.....	148
4.2.4 Discussion.....	152
4.2.5 Conclusion.....	154
4.3 Further development on process technology.....	154
4.3.1 Zeolitic sorbent for <i>in-situ</i> water removal.....	154
4.3.2 Zeolitic membrane for high-performance water / methanol separation.....	156
4.4 References.....	158
4.5 Appendix.....	161
4.5.1 XRD patterns of LTA zeolites.....	161
4.5.2 Chemical composition of LTA zeolites.....	161
Summary.....	162

List of abbreviations

Abbreviation	Elongation
PC	polycarbonate
DPC	diphenyl carbonate
BPA	4,4'-dihydroxy-2,2-diphenylpropane (bisphenol-A)
EO	ethylene oxide
DPO	diphenyl oxalate
DMC	dimethyl carbonate
DMP	2,2-dimethoxypropane
DCC	<i>N,N'</i> -dicyclohexylcarbodiimide
MPC	methyl phenyl carbonate
MMC	monomethyl carbonate
DME	dimethyl ether
PhOH	phenol
MeOH	methanol
Py	pyridine
BAS	Brønsted acidic site
LAS	Lewis acidic site
LBS	Lewis basic site
SBA	Santa Barbara Amorphous
ZSM	Zeolite Socony Mobil
VPI	Virginia Polytechnic Institute
MCM	Mobil Composition of Matter

(Continued)

LTA	Linde Type A
BET	Brunauer-Emmett-Teller
LH	Langmuir-Hinshelwood
ER	Eley-Rideal
KF	Karl-Fischer
TOF	turnover frequency
RDS	rate determining step
MR	-membered ring
PFG-NMR	pulsed-field gradient nuclear magnetic resonance
FT-IR	Fourier transformed infrared spectroscopy
FR	frequency response technology
DMMT	direct measurements of mass transportation
HPLC	high-performance liquid chromatography
GC	gas chromatography
ICP-OES	inductively coupled plasma optical emission spectrometry
XRD	X-ray diffraction
XPS	X-ray photoelectron spectroscopy
ESCA	electron spectroscopy for chemical analysis
UHV	ultra-high vacuum
MS	mass spectrometry
DSC	differential scanning calorimetry
TG	thermogravimetry
AAS	atomic absorption spectroscopy

(Continued)

AG	Aktiengesellschaft
NIST	National Institute of Standards and Technology
Eq.	Equation
wt.	Weight
<i>i.e.</i>	<i>id est</i>
<i>e.g.</i>	<i>exempli gratia</i>
<i>ca.</i>	<i>circa</i>
vs.	<i>versus</i>

Chapter 1

Introduction

1.1 Polycarbonates

Polycarbonates (PCs) are one of the most important engineering materials for their featured temperature resistance, impact resistance and optical properties. Different from most of the thermoplastics, PCs are able to afford large plastic deformation without cracking. The impact resistance of PCs makes them suitable for coatings on automotive components. Moreover, PCs are transparent to visible lights, with even better transmittance compared to a series of glasses. The three main fields of application for this material are as electronic components (*e.g.*, electrical insulator and dielectric capacitor), construction materials (*e.g.*, dome light and noise barrier) and data storage units (*e.g.*, CD, DVD and Blu-ray Disc). Furthermore, PCs are recently applied to high quality windows for automobiles. The versatility on application of PCs is based on their balanced properties allowing more possibilities on their design and handling options. ^[1, 2]

1.2 Brief history of PCs production

The first example of polycarbonate synthesis is dated from 1898, when benzenediols (hydroquinone or resorcinol) and phosgene were used as reactants in a lab-scale reactor. ^[3]

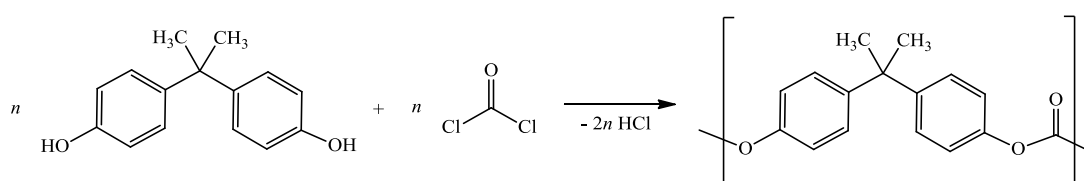
Following this investigation, another synthesis route towards PC without the use of phosgene was developed on lab scale. In 1902, the PC production via the transesterification between benzenediols and diphenyl carbonate (DPC) was reported. ^[4] The use of different benzenediol isomers enabled to have access to PCs with different physicochemical properties. The melting point of polymer produced from hydroquinone is $> 280\text{ }^{\circ}\text{C}$, while low melting point of PCs ($190 \sim 200\text{ }^{\circ}\text{C}$) were

obtained in the case of the synthesis process involving resorcinol. ^[5] For both synthesis pathways, due to their high energy demand of the process, the scaling-up attempts were abandoned for an industrial application.

The research on aromatic carbonates was continued without significant milestones for approximately 50 years. In the second half of 1950s, both Bayer AG and General Electric Company disclosed the invention of new synthesis route independent from each other. As described in the invention disclosure, PC can be synthesized by the use of bisphenol-A (BPA, 4,4'-dihydroxy-2,2-diphenylpropane). ^[6 - 8] In addition, this route allows the synthesis of products with high glass transition temperature and high optical transmittance. ^[9] From then on, the BPA-involved reaction routes became the major industrial approaches for the production of PCs.

1.3 Principal synthetic route for PCs production

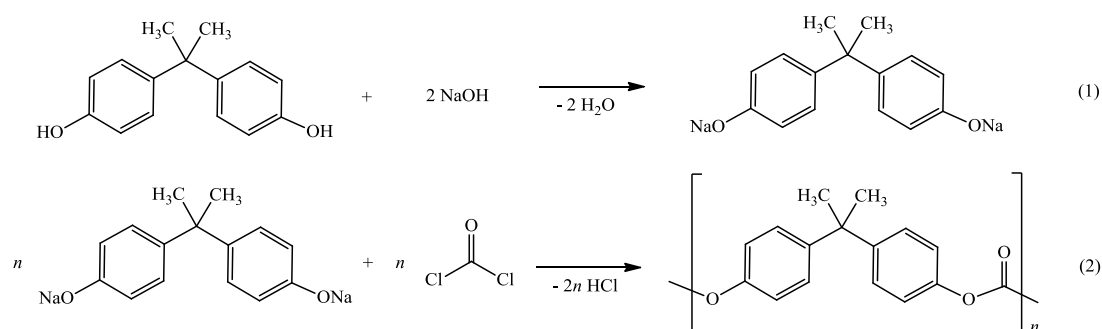
Currently, the most commonly applied polycarbonates production route is the reaction between BPA and phosgene (COCl_2). The overall reaction is shown in Scheme 1-1.



Scheme 1-1 Net reaction of polycarbonate synthesis via phosgenation

Practically, the reaction is not straightforward. The treatment of BPA with NaOH needs to be performed first, allowing the deprotonation of BPA's hydroxyl group, as indicated in Scheme 1-2 (Eq. 1). In the next step, the resulted sodium diphenoxide is

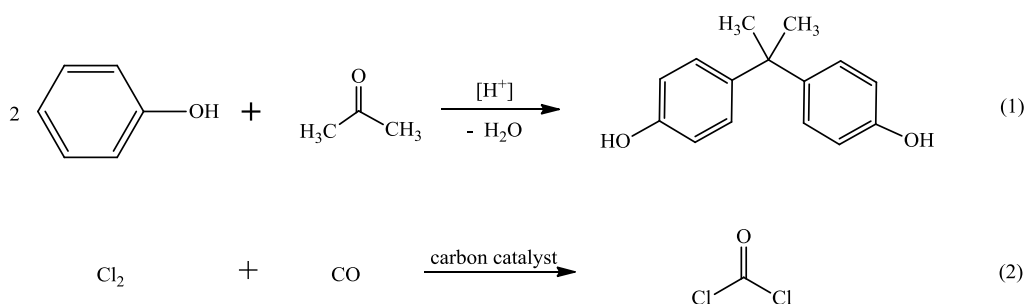
concomitantly reacted with phosgene forming chloroformate, which can rapidly be converted with another phenoxide afterwards to polycarbonate via a net polymerization, as shown in Scheme 1-2 (Eq. 2).



Scheme 1-2 Reaction pathways of the reaction between BPA and phosgene

With respect to process engineering aspects and product quality control, triethylamine was identified as a suitable catalyst, since its nucleophilicity favors the formation of acyl ammonium salt and enhances the conversion of phenolic reagents. Moreover, for controlling the molecular weight of polymer products, different phenolic reagents, such as phenol, 4-tert-butylphenol and 4-cumylphenol, were tested.^[10]

For this process, BPA can be synthesized by the direct condensation of acetone with phenol catalyzed by a strong acid, as prosecuted in Scheme 1-3 (Eq. 1).^[11, 12] An excess of phenol is required at industrial scale to ensure full condensation. In addition, an extra distillation process is also required in order to extract BPA from the reaction mixture containing by-products.



Scheme 1-3 Production pathways of BPA (1) and phosgene (2)

Besides BPA, another important reactant for PC formation is phosgene (COCl_2) in this synthesis route (Scheme 1-3, Eq. 2). The modern industrial COCl_2 synthesis has not changed significantly since 1920s. The entire process comprises the preparation of pure raw materials (Cl_2 and CO), the mixing of these compounds and the reaction of the mixed gases over a solid catalyst bed followed by the purification and condensation.^[13]

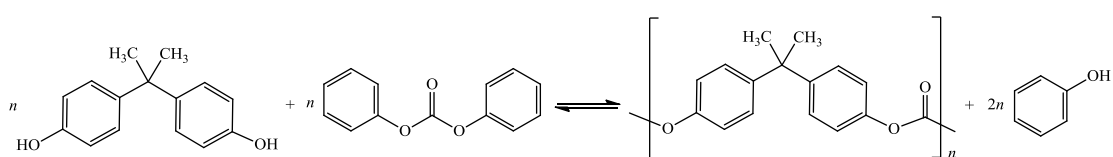
Phosgene is not an environmentally benign chemical due to its high toxicity. However, for its high reactivity, it has extreme importance on carbonylation reactions for pharmaceutical industry.^[14] Moreover, the co-produced huge amount of aqueous Cl^- during PCs synthesis leads to lots of technical efforts and economical costs on reactor maintenance. Hence, the disadvantages of the phosgenation process drove chemical engineers to search for innovative solutions that enable PCs production without the use of hazardous chemicals.

1.4 Alternative pathways for sustainable PCs production

1.4.1 Overview of possible routes

Industrially, an alternative synthesis route, usually called as “melt process”, BPA

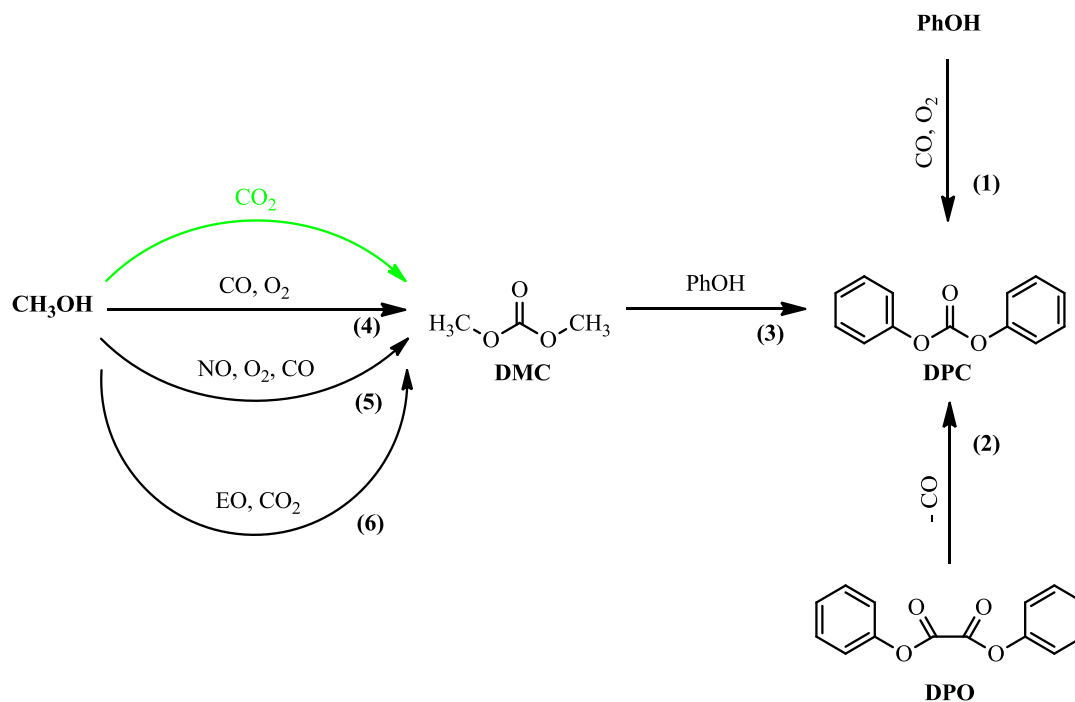
reacts with diphenyl carbonate (DPC), resulting in the formation of PCs and, simultaneously, phenol as the 2nd product via a transesterification reaction (Scheme 1-4). In this process, a little excess of DPC is applied to control the molecular weight of the polymer products. Furthermore, the transesterification reaction of melt process is an equilibrium constrained reaction. Therefore, the co-produced phenol has to be removed from the reaction mixture during the synthesis procedure via high vacuum distillation, in order to favor the forward chain growth reaction.



Scheme 1-4 Phosgene-free synthesis of PCs (melt process)

The melt process allows the conversion of BPA without the use of phosgene. As described in Section 1.3, BPA is produced via the reaction between acetone and phenol, without the use of hazardous chemicals. Thus, in order to reach the target of environmental friendly PCs production, a phosgene-free pathway synthesis of DPC, another starting reagent in melt process, is required.

In this respect, several possibilities without the use of toxic phosgene for DPC synthesis were proposed (Scheme 1-5).^[5]



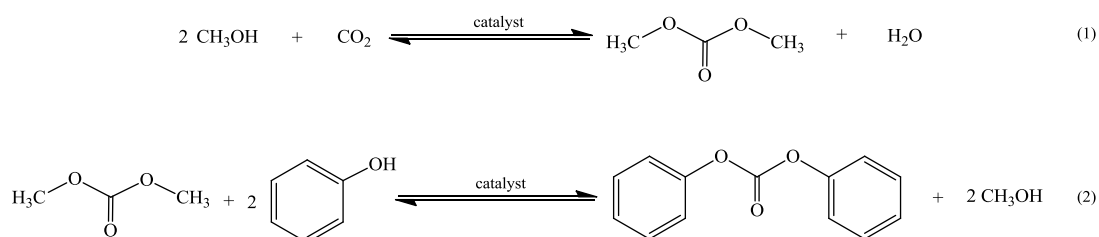
Scheme 1-5 Investigated phosgene-free pathways towards DPC formation (EO: ethylene oxide, PhOH: phenol)

Oxidative carbonylation of phenol and decarbonylation of diphenyl oxalate (DPO) are the mostly considered direct pathway towards DPC (pathways (1) and (2) in Scheme 1-5).^[15] The catalyst deactivation and separation problems in pathway (1) as well as the complexity on obtaining reagent DPO on industrial scale in pathway (2) limit the application of them. Most of the possible production routes involve dimethyl carbonate (DMC) as an intermediate (pathway (3) in Scheme 1-5). As for the production of DMC, methanol is used. CO or CO₂ are considered as a C₁ synthon.

In the industrially most favorable route for DMC synthesis, CO is successfully used as a C₁ building block (pathway (4), Scheme 1-5).^[16] In addition, DMC can be prepared via the formation of methyl nitrite by using CO, NO and O₂ in a catalytic sequence (pathway (5), Scheme 1-5). Subsequently, a transesterification reaction between DMC and phenol is required for obtaining DPC.^[17] However, CO is a toxic and flammable reagent, resulting in the difficulties and technical risks by its handling. In order to

fulfill the demands of sustainable and green chemical production, CO₂, as an environmental benign, renewable and non-toxic reagent molecule, has been considered as a possible C₁ building block. In a first attempt of using CO₂ for the synthesis of value-added chemicals, the transesterification of cyclic carbonates (pathway (6) in Scheme 1-5) has been considered and scaled up.^[18] In spite of the improvements achieved by the two phosgene-free routes (pathways (4) and (6) in Scheme 1-5), high process costs associated with the preparation and complex purification of the reactants and products negatively influence the economic efficiency of the process.

As one of the most relevant green process with the highest atomic efficiency, the catalytic direct carboxylation of methanol with CO₂ to synthesize DMC followed by its transesterification with phenol has been principally considered (detailed reaction sequence is depicted as Scheme 1-6).



Scheme 1-6 Phosgene-free DPC synthesis via DMC as an intermediate

In the reaction pathway shown in Scheme 1-6, the sole co-product in the net reaction is water. However, high atom efficiency is achieved only if the reaction proceeds with high selectivity towards DMC / DPC. Moreover, both of the reaction steps are thermodynamically constrained. These features make the proposed synthesis route very challenging on catalyst and process design. That points to the main target of the present thesis, *i.e.*, 1) mechanistically driven development of catalysts for phosgene-free DPC synthesis using DMC as an intermediate, and 2) reaction

optimization to ensure energy efficient and environment friendly sustainable DPC production.

1.4.2 Catalytic DMC synthesis from methanol and CO₂

DMC is an environmental benign chemical reagent in terms of its low toxicity, applied sometimes also as fuel additive and solvent. ^[19 - 21] Being applied in carbamates and isocyanate productions, DMC reacts with amines (primary or secondary) via gas- or liquid-phase thermolysis, arising potential industrial interests and being pursued by a number of chemical enterprises. ^[22, 23] Moreover, DMC is used as an alternative solvent substituting acetate esters and ketones, as oxygenate to reduce vehicle emission and as a photochemical friendly fuel with the lowest photochemical zone creation potential among all the oxygenated volatile organic compounds. ^[24, 25]

One of the very first attempts towards designing a catalyst for DMC formation from methanol and CO₂ was succeeded on 1979. ^[26] Dialkoxydibutyltin was identified as a suitable homogeneous catalyst for the reactions between corresponding alkyl alcohols (including methanol) and CO₂. This investigation was a result of an earlier study of the reaction between organotin compounds and CO₂. ^[27] The reactions were performed under CO₂ pressure. As for the mechanism of the catalytic cycle, it was assumed that CO₂ is inserted into the Sn-O bond of the organotin catalyst, followed by alcoholysis resulting in carbonate and Bu₂Sn(OH)₂, which in turn reacts with alcohol again, leading to the regeneration of the original catalyst and DMC formation. With concerns of process engineering, removal of the co-formed water from the reaction mixture is necessary to obtain DMC with high yield.

On industrial scale, heterogeneous catalysts are favorably considered owing to their

facilitated separation and regeneration after the catalytic run, albeit the activity and selectivity of homogeneous catalysts are much higher. Various heterogeneous catalytic materials like CeO₂, ZrO₂, Mg-Al hydrotalcite-silica lyogels and functional organotin catalyst tethered on SBA-15 porous materials were proposed for the DMC synthesis directly from methanol and CO₂.^[28 - 31] In the case of CeO₂ and ZrO₂ mixed oxide catalyst, when water was removed from the reaction mixture by using an internal dehydration agent, the methanol conversion was increased to 4.2 %.^[32] Furthermore, in a recent scientific contribution, it was shown that clay supported Cu-Ni bimetallic particles are able to afford 6.2 % DMC yield with 88 % selectivity.^[33] Overall, it is well accepted that the acidic / basic properties of the catalyst surface are the most important factors in designing effective heterogeneous catalysts for the selective DMC synthesis.^[34]

It is stated that the DMC synthesis from methanol and CO₂ is limited by equilibrium (equilibrium constant $K < 10^{-5}$ at a temperature range of 160 ~ 180 °C). Therefore, besides the research conducted for the catalyst development, considerable efforts have also been dedicated to shift the thermodynamic equilibrium towards enhancement of DMC yield. In this respect, two approaches were considered, *i.e.*, increase reactant concentration and the selective water removal. Based on Henry's law, higher partial pressure of CO₂ leads to higher concentration of CO₂ in liquid phase, thus, beneficial for yield enhancement. In a presented extreme instance, 50 % methanol conversion was achieved at 30 MPa CO₂ pressure after 72 hours time on stream.^[35] However, the excess of CO₂ leads to high investment costs on construction and maintenance of high pressure reaction units. Consequently, water removal was taken into consideration as a suitable approach to enhance the DMC yield. It has been reported that 2,2-dimethoxypropane (DMP) and *N,N'*-dicyclohexylcarbodiimide (DCC) can be used as chemical water scavenger.^[36] The chemical water scavengers selectively reacted with the co-formed water during the catalytic DMC synthesis (at same temperature and pressure as the catalytic DMC synthesis). After chemical water

scavengers are fully consumed by stoichiometric reaction with water, they need to be separated from the mixture and regenerated or recycled accordingly. The main disadvantages of the chemical water scavengers, thus, are the separation and regeneration, since they are operated in the same liquid phase as the catalytic reaction. In addition, the high expense of chemical water scavengers also limits their industrial application, because high amount of chemical water scavengers is required due to their low uptake capacity. Therefore, an easy-to-handle water scavenger with high selectivity, low cost and high reusability is still desired for its application in this case. With the above mentioned concerns, in order to overcome the disadvantages of chemical water scavengers, solid state materials have been considered for water removal instead of chemical water scavengers.

A short overview of recent progresses on DMC synthesis is listed in Table 1-1.

Table 1-1 DMC synthesis from methanol and CO₂: overview of literature results

Catalyst	Water trap	DMC yield (%)*	Reference
ZrO ₂	None	0.5	[29]
ZrO ₂ /CeO ₂	Acetal	4.3	[32]
ZrO ₂ /H ₃ PO ₄	None	0.62	[37]
H ₃ PW ₁₂ O ₄₀ /Ce _x Zr _{1-x} O ₂	None	0.4	[38]
Mg	None	1	[39]
ZrO ₂ /KCl	Butylene oxide	7.2**	[40]
ZrO ₂ /CeO ₂	None	0.7	[41]

* DMC yield is calculated on methanol basis.

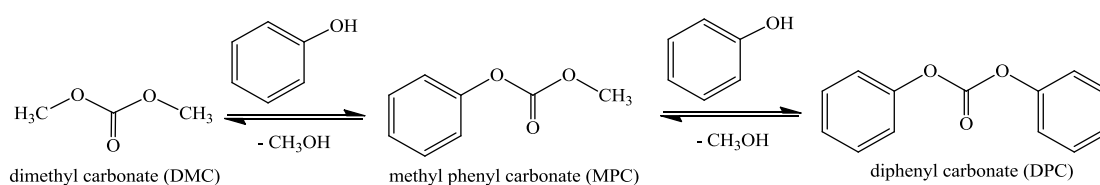
** DMC selectivity is 51 %.

From the results summarized in Table 1-1, it is evident that the DMC yield is rather low without the use of an appropriate water removal technique. Even by using of chemical water scavengers, such as acetal and butylenes oxide, the DMC yield is only enhanced till a limited level. Therefore, novel technical solutions are required.

1.4.3 Catalytic DPC synthesis from phenol and DMC

Besides its application in production of PCs, DPC has also attracted research interests as an intermediate for the synthesis of low molecular weight aliphatic monoisocyanates from ureas or allophenates.^[42 - 45] DPC synthesis can be achieved by the transesterification of DMC with phenol.^[46] Generally, the transesterification between carbonates and hydroxylic compounds involves the substitution of a less nucleophilic component with the more nucleophilic hydroxyl or by the substitution of the less volatile compound by the more volatile one.^[47] The transesterification of DMC with phenol to afford DPC occurs contrary to that and in consequence, a suitable catalyst is required to enable the chemical reaction at a higher rate.^[48]

DPC synthesis from phenol and DMC undergoes in two steps. In the 1st step, DMC reacts with phenol to form methyl phenyl carbonate (MPC). In the 2nd step, further transesterification of MPC with phenol or the disproportionation of MPC takes place (Scheme 1-7).



Scheme 1-7 Transesterification of DMC with phenol for DPC synthesis

Numerous homogeneous catalysts were reported to be efficient, *e.g.*, the

organometallic compounds of Ti, Sn, Si, Pb, Fe, Li and Al. ^[49 - 52] The reaction is carried out in liquid phase with the use of hydrocarbon solvent at a wide temperature range of 150 ~ 250 °C. In the homogeneous catalyzed process, formed co-product in the reaction is removed in the form of an azeotrope mixture with the hydrocarbon solvent or in the form of azeotrope mixture with DMC.

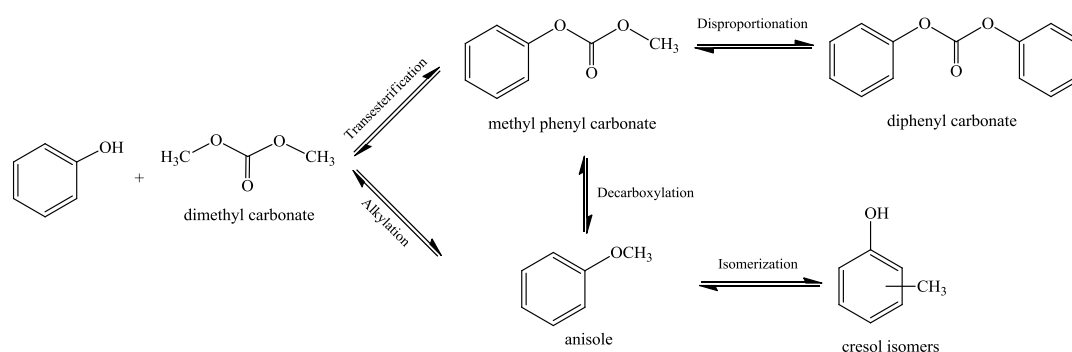
Similar as stated above, the development of heterogeneous catalysts are of considerable industrial interests due to their advantages in separation and regeneration. Various heterogeneous catalysts, *e.g.*, MoO₃/SiO₂, ^[53] TiO₂/SiO₂, ^[54, 55] V₂O₅/SiO₂, ^[56] PbO/MgO ^[57] and CeO₂-based mixed oxide ^[58] were reported for transesterification of DMC with phenol. Based on above listed contributions, it is known that transition metal oxides with mild surface acidic / basic properties are appropriate candidates as heterogeneous catalysts for transesterification of DMC with phenol. An overview of recent progresses on DPC synthesis is summarized in Table 1-2.

Table 1-2 DPC synthesis from phenol and DMC: overview of literature results

Catalyst	Product separation	Yield (%)*	Reference
Sb ₂ O ₃	None	4.8	[55]
V ₂ O ₅ /SiO ₂	Gas-phase reaction	2.8	[56]
PbO/SiO ₂	Reactive distillation	< 13.0	[57]
WO ₃ /SiO ₂	None	3.9	[59]
MgO	Reactive distillation	< 7.2	[59]
SnO ₂ /SiO ₂	None	11.5	[59]

* Yield is calculated for all transesterification products on phenol basis.

In contrast to homogeneous catalysts, in the presence of heterogeneous catalysts, the influence of side reaction becomes more significant as depicted in Scheme 1-8.



Scheme 1-8 Proposed reaction network enabled on the active sites of a heterogeneous catalytic system

In the reaction network shown in Scheme 1-8, strong acidic sites favorably catalyze the alkylation reaction between phenol and DMC, while strong basic sites accelerate the decarboxylation of MPC. Both alkylation and decarboxylation pathways lead to the formation of the main by-product anisole and its isomers. In order to enhance the catalyst performance and improve the overall selectivity for further developments on reaction engineering, a good understanding on the reactions at molecular level is required.

Similar as for DMC synthesis using methanol and CO_2 , the reaction of DPC synthesis is also equilibrium constrained (equilibrium constant $K < 10^{-5}$ at a temperature range of 160 ~ 180 °C). However, since an intermediate compound, MPC, is involved in the DPC formation, the evaluation of thermodynamic parameters on each step is required for defining the bottleneck of the total reaction network. In this respect, a detailed thermodynamic model was proposed, based on combined theoretical and experimental studies.^[60] The determined equilibrium constants of different reaction steps at a wide temperature range are shown in Figure 1-1.

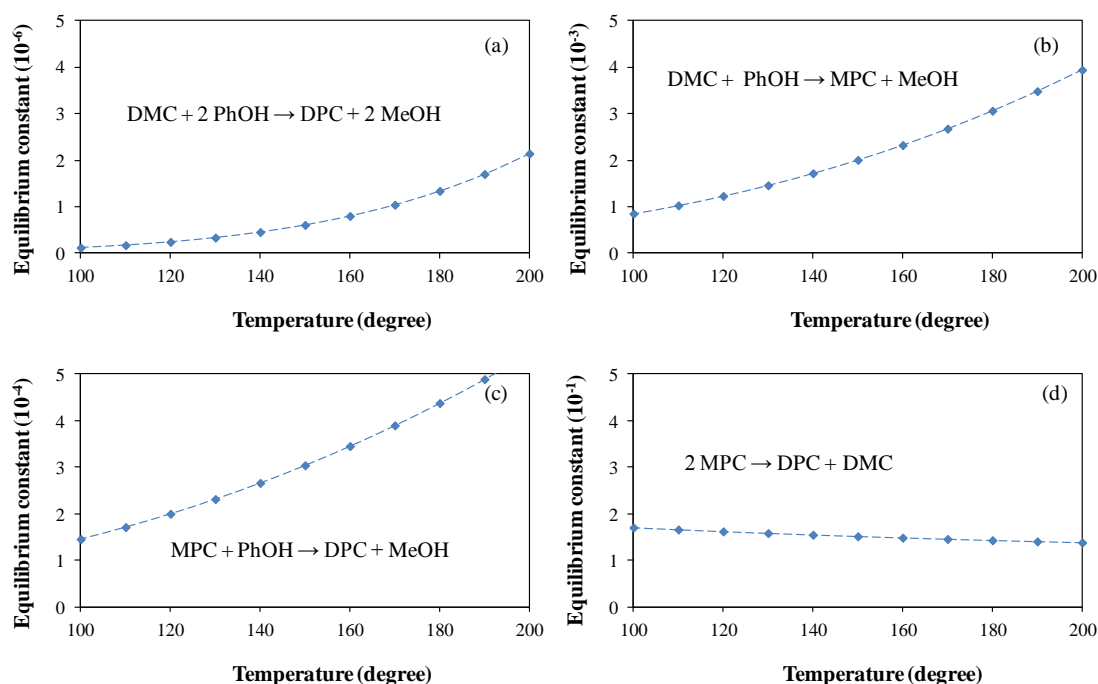


Figure 1-1 Equilibrium constants of different reaction steps involved in DPC synthesis

It is clearly noted that the co-produced methanol minimizes the formation of transesterification products (MPC and DPC, Figure 1-1 (a) ~ (c)). In addition, conversion from MPC to DPC is not strongly limited by the thermodynamic equilibria, if methanol is continuously removed from the reaction mixture (Figure 1-1 (d)). Therefore, it can be stated that the overall 1st step transesterification towards MPC is the bottleneck in DPC synthesis and methanol concentration needs to be minimized over the entire reaction course. Separated reaction zones for different reaction steps involving methanol removal were proposed in order to overcome the thermodynamic limitation.^[61] Hence, a continuous process was developed for the DPC synthesis from phenol and DMC catalyzed by titanium phenoxide. Three successive reaction zones were designed in order to tune the reaction conditions aiming the maximization of the product yield. In the first two reaction zones, MPC formation via the transesterification takes place. The vapors from the first two reaction zones were separated by distillation. The DPC formation was achieved in the third reaction zone.

Although the process based on reactive distillation technology has been already scaled up, the complexity within the process design motivates to the development of a new technology, which allows easier operation. Technologies that use *in-situ* methanol scavenger are convincing alternative solutions for large scale DPC production. Therefore, solid state materials, due to their advantages on separation and regeneration, are highly desired.

1.4.4 Zeolites as solid state sorbents

Zeolites are porous materials consisting of aluminum and silicon connected via oxygen atom bridges with the negative charge on the 4-coordinated aluminum atoms compensated by different cations. Some of them are naturally acquired, while nowadays more and more zeolites are artificially designed and synthesized.^[62] The distinction of zeolites is based on their features of pore / channel structure. Normally, microporous zeolites contain 8-, 10-, 12-membered oxygen ring and dual pore system, while mesoporous materials possess expanded porous structure, such as multi-membered ring and more complicated mesoporous system.

Some representative zeolites and their structural features are summarized in Table 1-3.

[63]

Table 1-3 Characteristics of some typical zeolites and mesoporous materials

Zeolite	Number of ring members*	Pore size (Å)	Pore / channel structure
Erionite	8	3.6 × 5.1	Intersecting
ZSM-5	10	5.1 × 5.6	Intersecting
ZSM-11	10	5.3 × 5.4	Intersecting
Ferrierite	8	3.5 × 4.8	Intersecting
	10	4.2 × 5.4	One-dimensional
Mordenite	8	2.6 × 5.7	Intersecting
	12	6.5 × 7.0	One-dimensional
ZSM-12	12	5.5 × 5.9	One-dimensional
Faujasite	12	7.4 × 7.4	Intersecting
VPI-5	18	12.1 × 12.1	One-dimensional
MCM-41	/	16 ~ 100	One-dimensional

* The number is based on the oxygen atoms contained in the ring.

Owing to the well-defined structure of channels and cages, which covers a wide range of size, zeolites are applied and investigated for their properties on selective adsorption and reaction of molecules with special shape and size, *i.e.*, shape selectivity. Shape selectivity was first described in 1960.^[64] Since then, the study on shape selectivity of porous materials, surely including zeolites, was frequently reported. Among all the porous materials, zeolites with small pores are especially important for the application of selective gas separation and membrane technology due to their selectivity for small molecule transportation.

1.4.5 Molecular diffusion in zeolites

The adsorption and diffusion are with high importance to understand the performance of zeolites on chemical separation. During the process of diffusion / transportation, the hindrance of the molecule movement may come from bulk materials, crystal particles or crystalline structures (pore / channel). As a measure of molecular diffusion, diffusivity (or diffusion coefficient) is defined as a proportional constant between the molar flux driven by molecular diffusion and the gradient on the species concentration (or other driving force for diffusion). For molecular diffusion in zeolitic materials, the relationship between diffusivity and pore size is shown in Figure 1-2.

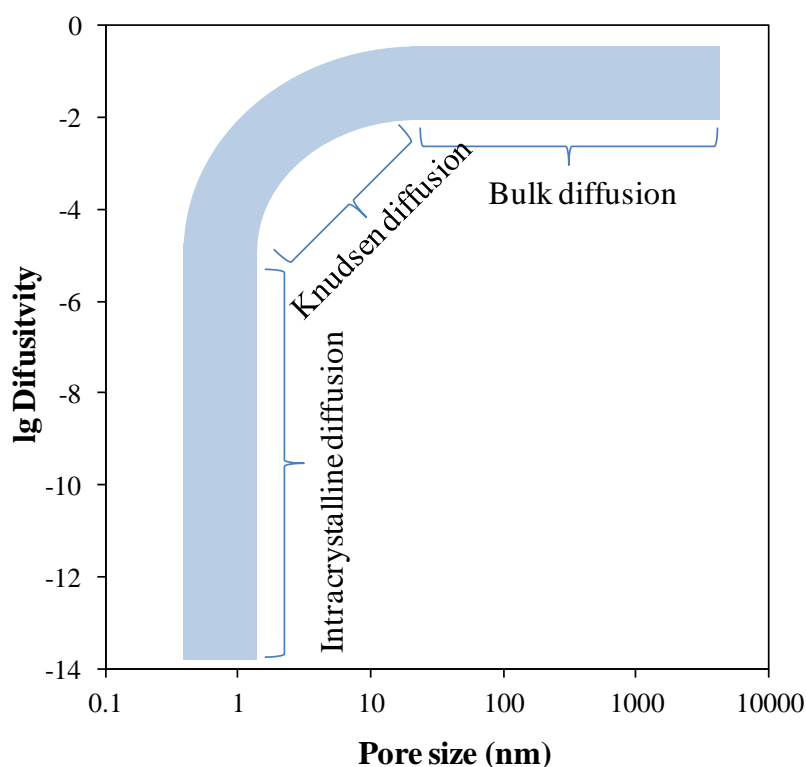


Figure 1-2 Schematic representation of the diffusivity (in $\text{cm}^2 \text{s}^{-1}$) in a porous zeolitic material

Considering molecular diffusion inside of a porous material, three main different regimes, *i.e.*, bulk diffusion, Knudsen diffusion and intra-crystalline diffusion, can be

identified. ^[65] Under a specific condition, only one of the three above mentioned diffusion types is dominating the diffusion process. When the pore diameter of the porous materials is smaller than the free mean path of the molecule, *i.e.*, pore size is large enough, collision among molecules is dominating. Since collisions among molecules have no impact on the porous structure of materials, it is also called as bulk diffusion. When the free mean path of the molecule is comparable or larger than the pore diameter, collisions between molecules and inter-crystalline channel becomes dominant. The process takes place in Knudsen diffusion regime. Only if the kinetic diameter of the molecule (not free mean path) is comparable to the size of the intra-crystalline pore (not inter-crystalline channel), the intra-crystalline diffusion becomes dominant. In most of the well-ordered porous structures, the shape selectivity is a result of the intra-crystalline diffusion.

In order to study the molecular transportation in zeolitic materials, several advanced technologies have been utilized, *e.g.*, pulsed-field gradient nuclear magnetic resonance (PFG-NMR), ^[66] neutron scattering, ^[67] zero-length column, ^[68] Fourier transformed infrared spectroscopy (FT-IR) ^[69] and frequency response technology (FR). ^[70] However, there is no approach able to provide a straightforward scenario of diffusion process, except direct measurement of mass transportation (DMMT). DMMT allows an accurate evaluation of thermodynamic and kinetic parameters on molecular diffusion in porous materials, especially in the case of small diffusivity and small crystal particle size (between 1 and 10 μm). ^[71]

1.5 Main challenges and opportunities on sustainable DPC synthesis

For an industry-oriented research, delivery of convincing technical solution is important. Within the whole synthesis route of phosgene-free production of PCs, the production of BPA has been already demonstrated in industrial scale without the use

of harmful reagents. Therefore, the DPC synthesis from phosgene-free pathway has been identified as the main target of the present thesis. As depicted in Scheme 1-6, two reaction steps are with different challenges from both kinetic and thermodynamic points of view.

DMC synthesis from methanol and CO₂, from kinetic point of view, requires the development of stable and selective catalysts able to enhance the very slow reactions. A key challenge in designing such a catalyst is to understand the complex surface chemistry of CO₂. Previous mechanistic and gas-phase kinetic studies have shown that various transition metals are able to activate CO₂ by forming linear species as σ -coordinated CO₂ and σ -coordinated CO, as well as carbonate and carboxylate surface species.^[72] The formation, stability and reactivity of surface intermediates vary in different chemical reactions. Thus, the relationship between required active forms is complicated and still requires special attention.

On the other hand, from thermodynamic point of view, DMC synthesis requires selective removal of water in a methanol-abundant reaction mixture for yield enhancement. Linde Type A zeolite (LTA or A zeolite) is a typical small-pore zeolite with the unit cell containing 8-membered rings, 6-membered rings and 4-membered rings (8MR, 6MR and 4MR). The pore opening of 8MR varies between 3 Å and 5 Å, which is a little larger than the kinetic diameter of water (2.6 Å), making it suitable for water removal. Nonetheless, the kinetic diameter of methanol is 3.6 Å, which is similar as water, let alone the polarity of them is also similar, making it difficult to separate water from methanol. Therefore, adsorption and diffusion properties of water and methanol, which are lack of reports, are required to be accurately analyzed, in order to propose a technical solution based on the use of zeolitic materials for DMC yield enhancement.

For DPC synthesis from phenol and DMC, similar issues are taken into considerations. A representative heterogeneous catalyst, $\text{MoO}_3/\text{SiO}_2$, was reported for its high selectivity on MPC and DPC formation. However, in-depth kinetic and mechanistic studies of heterogeneous catalysts for this reaction are not available yet. Moreover, the structure – activity correlation of $\text{MoO}_3/\text{SiO}_2$ catalyst is still lack of report. From thermodynamic point of view, the selective removal of methanol from the reaction mixture containing DMC and phenol is less difficult than water / methanol separation, and a similar approach from DMC synthesis can be transferred into this case. Nonetheless, the efficiency of methanol removal needs to be optimized to fit the rate of catalytic reaction.

1.6 Scope of the thesis

The main task of the present thesis is to provide fundamental understanding and a practical approach on the two-step phosgene-free DPC synthesis. Both kinetic and thermodynamic issues are discussed in detail.

In Chapter 2, a thorough experimental study has been carried out to unravel the mechanistic reasons for favorable CO_2 activation and conversion on ZrO_2 -based catalysts. Combining the experimental results from kinetic analysis and IR measurements under *operando* conditions, it was shown that the CO_2 adsorption and activation preferentially takes place on the new basic sites of the MgO-ZrO_2 , leading to the formation of surface-active bidentate bicarbonate and bidentate carboxylates. As a result, the MgO-ZrO_2 catalyst yields a 3-fold improvement of DMC compared to ZrO_2 catalyst.

In Chapter 3, $\text{MoO}_3/\text{SiO}_2$ catalyst was selected for a kinetic and mechanistic study on transesterification of DMC with phenol. The activity-structure correlation was made

by combining reaction and characterization results. It was further concluded that DMC and phenol molecules are competitively adsorbed on surface Lewis acidic sites, leading to the formation of key intermediate, an asymmetrical surface carbonate species.

In Chapter 4, for yield enhancement of DMC synthesis, accurate analysis of adsorption and diffusion parameters for water and methanol inside the microcrystalline zeolite has been conducted by using a demanding analysis technique based on DMMT approach in liquid phase. This enabled the development of a process for DMC synthesis, where a sorbent with excellent water selectivity is used, to enhance the strong equilibrium constrained reaction. Similar approach was further applied to DPC synthesis. *In-situ* methanol removal by zeolitic sorbents allowed significant enhancement of transesterification products. Furthermore, the performance of newly developed zeolitic materials was briefly presented.

At the end, the summary and conclusion are given in Chapter 5.

1.7 References

- [1] V. Serini, *Polycarbonates in Ullmann's Encyclopedia of Industrial Chemistry*, Wiley-VCH, Weinheim, **2000**
- [2] M. Parvin, J. G. Williams, *J. Mater. Sci.* **1975**, *10*, 1883
- [3] A. Einhorn, *Liebigs Annalen der Chemie* **1898**, *300*, 135
- [4] C. A. Bischoff, A. V. Hedenstroem, *Berichte der deutschen chemischen Gesellschaft*, **1902**, *35*, 3431
- [5] D. J. Brunelle, M. Korn, *Advances in Polycarbonates*, American Chemical Society, **2005**

- [6] H. Schnell, *Angew. Chem.* **1956**, 68, 633
- [7] H. Schnell, *Ind. Eng. Chem.* **1959**, 51, 157
- [8] D. W. Fox, *US Patent*, **1964**, 3144432
- [9] W. F. Christopher, D. W. Fox, *Polycarbonates*, Reinhold Publishing Corporation, New York, **1962**
- [10] H. Schnell, *The Chemistry and Physics of Polycarbonates*, Wiley Interscience, New York, **1964**
- [11] А. П. Дианин, *Журнал Русского физико-химического общества* **1891**, 23, 488
- [12] T. Zincke, *Liebigs Annalen der Chemie*, **1905**, 343, 75
- [13] K. L. Dunlap, *Phosgene in Kirk Othmer Encyclopedia of Chemical Technology*, Wiley-VCH, Weinheim, **2001**
- [14] W. Schneider, W. Diller, *Phosgene in Ullmann's Encyclopedia of Industrial Chemistry*, Wiley-VCH, Weinheim, **2002**
- [15] H. Y. Song, E. D. Park, J. S. Lee, *J. Mol. Catal. A: Chem.* **2000**, 154, 243
- [16] G. Illuminati, U. Romano, R. Tesei, *US Patent* **1980**, 4182726
- [17] J. Haubrock, M. Raspe, G. F. Versteeg, H. A. Kooijman, R. Taylor, J. A. Hogendoorn, *Ind. Eng. Chem. Res.* **2008**, 47, 9862
- [18] B. M. Bhanage, M. Arai, *Transformation and Utilization of Carbon Dioxide*, Springer-Verlag GmbH, **2014**
- [19] P. Tundo, M. Selva, *Acc. Chem. Res.* **2002**, 35, 706
- [20] P. Jessop, T. Ikariya, R. Noyori, *Chem. Rev.* **1999**, 99, 475
- [21] S. N. Isaaca, B. O. Sullivan, C. Verhaelen, *Tetrahedron* **1999**, 55, 11949
- [22] F. Mizia, F. Rivetti, U. Romano, *US Patent* **1994**, 5315034
- [23] M. Aresta, E. Quaranta, *Tetrahedron* **1991**, 47, 9489
- [24] M. A. Pacheco, C. L. Marshall, *Energy Fuel* **1997**, 11, 2
- [25] M. E. Jenkin, G. D. Hayman, *Atmos. Environ.* **1999**, 33, 1275

- [26] N. Yamazaki, S. Nakahama, F. Higashi, *Ind. Chem. Prod. Res. Dev.* **1979**, *18*, 249
- [27] S. Sakai, T. Fujinami, T. Yamada, S. Furusawa, *Nippon Kagaku Kaishi* **1975**, *10*, 1789
- [28] M. Aresta, A. Dibenedetto, C. Pastore, A. Angelini, B. Aresta, I. Papai, *J. Catal.* **2010**, *269*, 44
- [29] K. Tomishige, Y. Ikeda, T. Sakaihorii, K. Fujimoto, *J. Catal.* **2000**, *192*, 355
- [30] D. C. Stoian, E. Taboada, J. Llorca, E. Molins, F. Medina, A. M. Segarra, *Chem. Commun.* **2013**, *49*, 5489
- [31] B. Fan, J. Zhang, R. Li, W. Fan, *Catal. Lett.* **2008**, *121*, 297
- [32] K. Tomishige, K. Kunimori, *Appl. Catal. A: Gen.* **2002**, *237*, 103
- [33] Y. Zhou, S. Wang, M. Xiao, D. Han, Y. Lu, Y. Meng, *J. Clean Prod.* **2015**, *103*, 925
- [34] K. T. Jung, A. T. Bell, *J. Catal.* **2001**, *204*, 339
- [35] J. Choi, L. He, H. Yasuda, T. Sakakura, *Green Chem.* **2002**, *4*, 230
- [36] M. Aresta, A. Dibenedetto, E. Fracchiolla, P. Giannoccaro, C. Pastore, I. Pápai, G. Schubert, *J. Org. Chem.* **2005**, *70*, 6177
- [37] Y. Ikeda, T. Sakaihorii, K. Tomishige, K. Fijimoto, *Catal. Lett.* **2000**, *66*, 59
- [38] K. W. La, I. K. Song, *React. Kinet. Catal. Lett.* **2006**, *89*, 303
- [39] Y. Du, L.-N. He, D.-L. Kong, *Catal. Commun.* **2008**, *9*, 1754
- [40] V. Eta, P. Mäki-Arvela, A. R. Leino, K. Kordás, T. Salmi, D. Yu. Murzin, J. P. Mikkola, *Ind. Eng. Chem. Res.* **2010**, *49*, 9609
- [41] H. J. Hofmann, A. Brandner, P. Claus, *Chem. Ing. Tech.* **2011**, *83*, 1711
- [42] V. Schwendemann, D. Mangold, *EP Patent*, **1980**, 50739
- [43] H. Schnell, V. Bollert, G. Fritz, *GB Patent*, **1960**, 958798
- [44] D. W. Fox, D. E. Floryan, *DE Patent*, **1973**, 2359260
- [45] J. E. Telschow, E. D. Weil, *US Patent*, **1993**, 5235085

- [46] A. G. Shaikh, S. Sivaram, *Chem. Rev.* **1996**, 96, 951
- [47] H.-J. Buysch, *Carbonic acid esters* in *Ullmann's Encyclopedia of Industrial Chemistry*, VCH, Weinheim, **1986**
- [48] R. Sridharan, I. M. Mathai, *J. Sci. Ind. Res.* **1974**, 33, 178
- [49] V. Mark, *DE Patent* **1985**, 3445555
- [50] T. Onada, K. Tano, Y. Hara, *JP Patent* **1979**, 125617
- [51] Y. Harauo, *JP Patent* **1986**, 61172852
- [52] Y. Harauo, *JP Patent* **1987**, 62277345
- [53] Z. Fu, Y. Ono, *J. Mol. Catal. A: Chem.* **1997**, 118, 293
- [54] W. B. Kim, J. S. Lee, *J. Catal.* **1999**, 185, 307
- [55] W. B. Kim, J. S. Lee, *Catal. Lett.* **1999**, 59, 83
- [56] D. Tong, J. Yao, Y. Wang, H. Niu, G. Wang, *J. Mol. Catal. A: Chem.* **2007**, 268, 120
- [57] M. Cao, Y. Meng, Y. Lu, *Catal. Commun.* **2005**, 6, 802
- [58] A. Dibenedetto, A. Angelini, L. Bitonto, E. De Giglio, S. Cometa, M. Aresta, *ChemSusChem* **2014**, 7, 1155
- [59] K. Tomishige, K. Kunimori, *Appl. Catal. A: Gen.* **2004**, 260, 19
- [60] J. Haubrock, M. Raspe, G. F. Versteeg, H. A. Kooijman, R. Taylor, J. A. Hogendoorn, *Ind. Eng. Chem. Res.* **2008**, 47, 9854
- [61] G. E. Harrison, A. J. Dennis, M. Sharif, *WO Patent*, **1992**, 18458
- [62] W. M. Meier, D. M. Olson, *Atlas of Zeolite Structure Types*, Butterworth-Heinemann, London, **1992**
- [63] T. Tsai, S. Liu, I. Wang, *Appl. Catal. A: Gen.* **1999**, 181, 355
- [64] P. B. Weisz, V. J. Frilette, *J. Phys. Chem.* **1960**, 64, 382
- [65] J. Xiao, J. Wei, *Chem. Eng. Sci.* **1992**, 47, 1123
- [66] J. Kärger, D. M. Ruthven, *Zeolites* **1989**, 9, 267

- [67] L. E. Cohen, R. Kahn, F. Mezei, *J. Chem. Soc. Faraday Trans. I* **1983**, 79, 1911
- [68] D. M. Ruthven, S. Brandani, *Membr. Sci.* **2000**, 6, 187
- [69] G. Mirth, J. A. Lercher, *J. Catal.* **1993**, 139, 24
- [70] L. V. C. Rees, *Stud. Surf. Sci. Catal.* **1994**, 84, 1133
- [71] R. M. Barrer, *Zeolites and Clay Minerals as Sorbents and Molecular Sieves*, Imperial College, London, **1978**
- [72] H. J. Freund, M. W. Roberts, *Surf. Sci. Rep.* **1996**, 25, 22

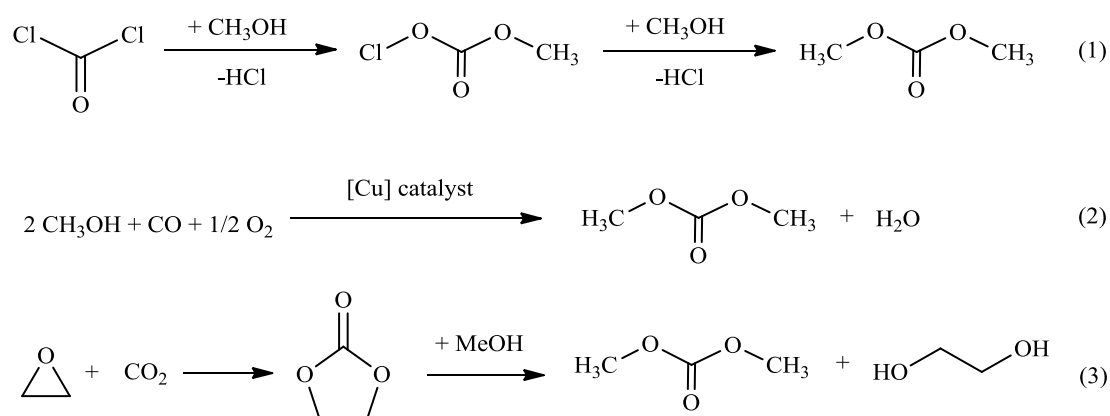
Chapter 2

Rate enhancement of DMC formation from methanol and CO₂ over ZrO₂-based catalysts by heteroatom doping

Within this chapter, a thorough experimental study has been carried out to unravel the mechanistic reasons for favorable CO₂ activation and conversion over MgO-ZrO₂ catalyst. By using XPS analysis, it was possible to show that the heteroatom insertion in the ZrO₂ lattice takes place, leading to the formation of a homogeneous solid solution bearing new sites for catalysis at low doping degrees. Combining the experimental results from kinetic analysis and IR measurements under *operando* conditions, it was shown that the CO₂ adsorption and activation preferentially takes place on the new basic sites of the MgO-ZrO₂, leading to the formation of surface-active bidentate bicarbonate and bidentate carboxylates. The contribution of weak acidic sites and basic sites of the catalysts further facilitates the formation and stabilization of monomethyl carbonate, a crucial intermediate in DMC synthesis. The MgO-ZrO₂ yields a 3-fold improvement on catalytic efficiency compared to ZrO₂.

2.1 Introduction

Sustainable chemical production aiming to design and deliver environmentally preferable products is highly desired. Dimethyl carbonate (DMC) is an environmental benign green chemical achieving increasing importance for the chemical industry due to its versatility and usability as a non-toxic carbonylation and alkylation reagent, fuel additive and polar solvent. ^[1] On industrial scale, there are three main large-scale processes for DMC synthesis, *i.e.*, the methanolysis of phosgene (Scheme 2-1 (Eq. 1)), ^[2] oxidative carbonylation of methanol (Scheme 2-1 (Eq. 2)) ^[3] and transesterification of cyclic carbonate (Scheme 2-1 (Eq. 3)). ^[4]

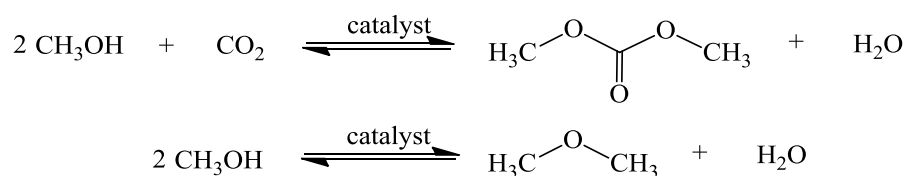


Scheme 2-1 Reaction pathways towards DMC synthesis

As illustrated in Scheme 2-1 (Eq. 1), DMC synthesis via methanolysis of phosgene requires the use of significant amounts of a poisonous and corrosive gas such as phosgene. ^[5,6] To focus on the more specific area of the replacement of harmful and undesirable compounds, the oxidative carbonylation of methanol (depicted in Scheme 2-1 (Eq. 2)) has been considered as an alternative path for the industrial production of DMC. ^[7,8] This reaction route involves the use of copper as a redox catalyst and, thus, requires high partial pressure of CO in order to reduce the oxidized copper species Cu(II) to Cu(I) in an atmosphere containing O₂. Although the use of highly toxic

phosgene has been avoided, a flammable and toxic CO is still required. Moreover, during operation, the formation of acidic by-products gradually causes the failure of plants and the redox catalyst deactivates rapidly. ^[6] Therefore, in order to fulfill the demands of sustainable and green chemical production, CO₂, as an environmental benign, renewable and non-toxic reagent molecule, has been considered as a possible C₁ building block. In a first attempt of using CO₂ for the synthesis of value-added chemicals, the transesterification of cyclic carbonates (illustrated in Scheme 2-1 (Eq. 3)) has been considered and scaled up. In spite of the improvements achieved by the two phosgene-free routes, high process costs associated with the preparation and complex purification of the reactants and products negatively influence the economic efficiency of the process. In this respect, considerable efforts have been made to overcome these drawbacks.

As one of the most relevant green process, the catalytic direct carboxylation of methanol with CO₂ (Scheme 2-2) has been principally considered.



Scheme 2-2 DMC synthesis from methanol and CO₂ and possible side reaction

Various heterogeneous catalytic materials like CeO₂, ZrO₂, Mg-Al hydrotalcite-silica lyogels and functional organotin catalyst tethered on SBA-15 were proposed for the DMC synthesis directly from methanol and CO₂. ^[9 - 12] The major disadvantages of this process are, however, the low methanol conversion and high consumption of energy to consequently shift the reaction equilibrium and favour the DMC formation. ^[10, 12] In the case of CeO₂ and ZrO₂ mixed oxide catalyst, when water was removed from the reaction mixture by using an internal dehydration agent, the methanol

conversion was increased to 4.2 %.^[13] By using mixed Mg-Al oxides supported on silica lyogels 15.9 % conversion and high selectivity to DMC was achieved under controlled experimental conditions.^[12] Furthermore, in a recent scientific contribution, it was shown that clay supported Cu-Ni bimetallic particles are able to afford 6.2 % DMC yield with 88 % selectivity.^[1] Overall, it is well-accepted that the acidic / basic properties of the catalyst surface are the most important factors in designing effective heterogeneous catalysts for the selective DMC synthesis.^[10, 14]

For the design and operation of a sustainable and green process for the direct DMC synthesis, the development of stable and selective catalysts able to enhance the very slow reactions is required. A key challenge in designing such a catalyst is to understand the complex surface chemistry of CO₂. Previous mechanistic and gas-phase kinetic studies have shown that various transition metals are able to activate CO₂ by forming linear species as σ -coordinated CO₂ and σ -coordinated CO, as well as carbonate and carboxylate surface species.^[15] The formation, stability and reactivity of surface intermediates vary in different chemical reactions. Thus, the relationship between required active forms is complicated and still requires special attention.

In order to further optimize the catalytic performance, within this work, heteroatom modification of ZrO₂ with various metal oxides, resulting in the formation of new acidic / basic sites with different strengths, is proposed. Owing to their known properties, Al₂O₃ and MgO were selected as doping agents for this study. The insertion of Al³⁺ or Mg²⁺ into a ZrO₂ crystal lattice are supposed to be able to create new active sites, owing to their different electronegativities, coordination numbers and different doping effects on the crystalline lattice. Herein the results of a systematic multi-technique experimental study on the catalytic formation of DMC from methanol and CO₂ on ZrO₂ as well as MgO-ZrO₂ and Al₂O₃-ZrO₂ mixed oxides are presented. The results from detailed *in-situ* IR study reveal that CO₂ activation on

ZrO₂-based catalysts occurs via the formation of bidentate bicarbonate and bidentate carboxylate species on the surface-active Lewis basic sites (LBS). However, on the surface of ZrO₂ catalyst, only bidentate bicarbonate species can be further converted into the key intermediate monomethyl carbonate (MMC). In contrast to ZrO₂, MgO-ZrO₂ mixed oxide facilitates the CO₂ adsorption and conversion of both bidentate bicarbonate and bidentate carboxylate, leading to the fast formation of the MMC intermediate. The direct reaction of the MMC species with the second methanol molecule enables the DMC formation with very high selectivity (over 99 %). By analyzing the composition of reaction mixture, it is evidenced that DMC is the only detected product. The selectivity of DMC is, therefore, higher than 99 %. Moreover, exceptional catalyst stability was shown by repetitive use of the same material for catalytic DMC formation. As a consequence, it is evidenced that the catalytic rate and catalyst stability of ZrO₂-based catalyst is significantly enhanced by MgO doping, attributed to stabilization of the tetragonal phase as well as generation of new active Lewis basic sites responsible for CO₂ activation and further conversion.

2.2 Experimental

2.2.1 Catalyst preparation

All Al₂O₃-ZrO₂ and MgO-ZrO₂ mixed oxide catalysts with varying contents of alumina and magnesia were prepared by co-precipitation of a solution of zirconyl nitrate (ZrO(NO₃)₂ · H₂O) with the desired amount of aluminum nitrate (Al(NO₃)₃ · 9 H₂O) and magnesium nitrate (Mg(NO₃)₂ · 6 H₂O). The pH of the aqueous solution was maintained constant in the range of *ca.* 9 ~ 10 by dropwise addition of a concentrated aqueous ammonia (NH₃ · H₂O) solution. The total cation concentration of each mixed solution was 0.5 mol L⁻¹. All the samples were aged at room temperature overnight. The isolated precipitates were then thoroughly washed with

bi-distilled water, dried at 120 °C overnight and ground into fine powder. Prior to test, each sample was calcined in synthetic air with a flow rate of 100 mL min⁻¹ at 500 °C for 6 hours in a tube furnace (1 °C min⁻¹ ramp).

2.2.2 Catalytic reaction

Direct DMC synthesis was carried out in a home-made stainless steel autoclave with an inner volume of 70 mL. For maintaining the pressure during catalytic reaction, a stainless steel sample cylinder with an inner volume of 50 mL (Swagelok) was attached to the autoclave reactor. In a typical reaction procedure, various amounts of ZrO₂-based solid catalyst (0.5 ~ 2 g) were suspended in 39.6 g of methanol. The autoclave was then sealed and purged with N₂ several times. Before heating the reactor, N₂ atmosphere with ambient pressure was kept in the autoclave. After the autoclave was heated to the reaction temperature (160 °C, monitored by Eurotherm 2132 temperature controller), 10 g of CO₂ were introduced with a flow rate of 5 mL min⁻¹ by using a syringe pump (Teledyne Isco, model 500) that in this case was set to 80 bar at 20 °C for accurate control. For product analysis, aliquots of the filtered sample were taken every 15 min by using an HPLC pump (Gilson 303). The composition of the reaction mixture was determined by GC (GC 8000 series, Fisons Instrument) equipped with a fused silica (Rtx-5AM) column. For analysis, the column temperature was set to 80 °C and the samples were measured under isothermal conditions.

For testing the chemical and thermal stability of various catalysts under operating conditions, the reaction was repeated by using the same catalyst 6 times. After each catalytic run, the catalyst was collected by filtration and dried at 120 °C overnight. The ICP-OES measurement of the liquid reaction mixture after catalytic reaction was conducted on a SpectroFlame type FTMOA81A (Spectro Analytical Instruments)

setup. In a typical measurement, fine aerosol was created in a nebulizer, and further transferred with Ar flow to plasma. Afterwards, the emission of light was split in the specific wavelengths of certain elements (Zr, Al, Mg *etc.* in this study) by a polychromator and the intensity was detected by a photomultiplier. As the liquid samples had high percentages of methanol so that the vapour pressures were too high to be introduced into ICP-OES setup, the calibration and the quantitative analysis of the metal content in methanol abundant solutions were performed with 100-time water dilution.

In order to determine the correlation between reaction rate and reactant composition, DMC formation catalyzed by ZrO₂-based catalysts was also performed with different amounts of methanol and CO₂. The methanol amounts varied from 25 g to 50 g and the CO₂ amounts varied from 5 g to 12 g.

After the catalytic reaction of DMC formation catalyzed by ZrO₂-based catalysts, the liquid reaction mixtures were collected and filtered for ICP-OES measurement.

2.2.3 Catalyst characterization

The crystal structure of synthesized materials was analyzed by X-ray diffraction (XRD) measurements. Philips X'Pert Pro diffractometer equipped with an X'celerator module using Cu-K α radiation operating at 40 kV / 45 mA was applied. The samples were measured with a scan rate of 3 ° min⁻¹ from 5 ° to 70 ° (2 θ).

X-Ray photoelectron spectroscopy (XPS) spectra were obtained by using a modified VG ESCALAB 220 spectrometer, equipped with a microspot monochromatized Al-K α or Mg-K α source and a homemade ultra-high vacuum (UHV) cell. The Al-K α line (1486.5 eV) was used throughout the present work and the base pressure of the

measuring chamber was below 1.5×10^{-8} mbar. In order not to overlap the signal from samples, a stainless steel support was used to introduce samples (pressed into self-supporting wafers) into a UHV cell. Throughout all the measurements performed, besides Zr, O, Al and Mg lines, C and Fe lines were also found (C as an expected impurity and Fe from the support).

In order to determine the BET specific surface area of all synthesized catalysts, N_2 adsorption-desorption measurements were performed with a Sorptomatic 1990 Series instrument. In all the cases, the samples were activated in vacuum at 300 °C for 2 hours before measurements. The adsorption-desorption processes were conducted at -196 °C.

The nature and concentration of surface acidic sites were analyzed by temperature programmed desorption (TPD) of NH_3 , by using a 6-fold parallel reactor system. Similarly, CO_2 -TPD was applied to characterize surface basic sites. For TPD experiments, 50 ~ 100 mg of samples were pretreated at 500 °C (5 °C min^{-1} ramp) in He stream for 1 hour in order to remove surface contaminants. After cooling at 100 °C, ammonia was adsorbed with a partial pressure of 1 mbar. In contrast, CO_2 adsorption was performed at 40 °C. Subsequently, the samples were purged with 30 mL min^{-1} He for 2 hours in order to remove all physisorbed molecules. Then 6 samples were sequentially heated from 100 to 770 °C with an increment of 10 °C min^{-1} to desorb NH_3 and from 40 to 700 °C to desorb CO_2 . For analysis of the surface bonded species, an attached mass spectrometer (Balzers QME 200) was used. The amount of desorbed NH_3 was determined by the integration of the MS signal calibrated to a standard material (H-ZSM-5 zeolite, Si / Al = 45, number of acidic sites $360 \text{ } \mu\text{mol g}^{-1}$). The response of the CO_2 signal was calibrated by employing the decomposition of $NaHCO_3$.

IR spectroscopy of adsorbed pyridine was used to determine the concentration of Brønsted and Lewis acidic sites (BAS and LAS). The samples were pressed into thin self-supporting wafers and activated at 450 °C for 1 hour in vacuum. Prior to pyridine adsorption, the background spectrum was recorded by an IR spectrometer (Perkin-Elmer 2000) with resolution of 2 cm⁻¹. Subsequently, the activated samples were exposed to pyridine vapors at a pressure of 0.1 mbar for approximately 1 hour at 150 °C. After outgassing for 0.5 hour to remove physisorbed pyridine, another spectrum was recorded. The bands at *ca.* 1540 cm⁻¹ and 1450 cm⁻¹ were used for characterization of BAS and LAS, respectively. The concentrations of the Brønsted and Lewis acidic sites were calculated from the integrated areas of the difference between these two bands with the molar extinction coefficients calibrated as 0.73 cm⁻¹ μmol⁻¹ for BAS and 0.96 cm⁻¹ μmol⁻¹ for LAS, respectively. ^[16]

For studying the surface chemistry and for the identification of intermediates involved in the various elemental steps, *in-situ* vacuum infrared (IR) spectroscopic measurements (Bruker ISF88) were performed. Methanol, CO₂, dimethyl ether (DME) and dimethyl carbonate (DMC) were separately used as adsorbate molecules in independent experiments or concomitantly added for the identification of *in-situ* formed intermediates on the catalyst surface. The temperature-dependent IR measurements, in this study, were performed as follows. With all surface stable intermediates, it was possible to design a temperature programmed measurement on a catalyst sample, in order to track relevant transformations of key intermediates under *quasi*-steady-state conditions. Based on experimental evidence, a temperature ramp of 1 °C min⁻¹ was determined as suitable for the ZrO₂-based catalytic system with all surface intermediates formed during DMC formation. In a typical temperature-dependent IR measurement, the catalyst was first pressed into thin self-supporting wafers and activated under vacuum ($p = 10^{-6}$ mbar) at 450 °C for 1 hour and the reference spectrum was recorded at 40 °C under vacuum. Following that measurement, the adsorbate was also added at 40 °C and spectra were recorded.

Afterwards, the system evacuation at 40 °C was initiated, and IR spectra of treated catalyst were continuously recorded at an interval of 2 min till the surface species reached a steady state (no visible change was observed between two sequential spectra). The heating program was then started (temperature ramp 1 °C min⁻¹), and IR spectra were recorded from 40 °C to 160 °C. The recorded spectra were representative for the steady-state conditions at the recording temperatures.

The adsorbate uptake and the adsorption capacities of various catalysts were studied by using gravimetric uptake measurements combined with differential scanning calorimetry (DSC). For these experiments, a highly sensitive microbalance with detection limit of 10⁻⁷ g was used. For analysis, a quartz holder was filled with solid sample and placed inside a heating block with adjustable temperatures. A non-adsorbing reference was simultaneously measured under identical operational conditions. The corresponding adsorption isotherms and heat of adsorption were calculated from the obtained mass uptake profiles and the heat release during the adsorption processes. Gravimetric sorption isotherms were measured on a modified SETARAM TG-DSC 111 thermogravimetric instrument. The synthesized catalysts were pressed into wafers and broken into small pellets before moving into the sample holder to avoid the contamination of vacuum system by fine powders. The samples were heated to 450 °C with ramp of 10 °C min⁻¹ under vacuum and held at 450 °C for 1 hour before adsorption. Adsorbates were introduced into the sample cell with pressure steps in the range of 10⁻³ to 10 mbar using a Balzers UDV 040 dosing valve. The calibration with an iridium standard was a prerequisite for an accurate measurement. Data analysis was performed with an Agilent-VEE Professional program (Version 8.0).

2.3 Results

2.3.1 Physico-chemical properties of ZrO_2 -based catalysts

In the initial efforts to rationally design a high-performance catalyst for the selective and energy efficient DMC synthesis, all the obtained zirconia materials were unambiguously characterized by techniques that include nitrogen adsorption (BET), powder X-ray diffraction (XRD), X-ray photoelectron microscopy (XPS) and infrared spectroscopy (IR).

It is well known that zirconium oxide exhibits different structural polymorphs.^[17,18] The most common ones are the monoclinic, tetragonal and cubic phases. It is important to note, that the thermodynamically less-stable cubic phase was not present in any of the synthesized materials (experimental evidence by Raman spectroscopy is available in Section 2.7.1, Figure 2-19). Detailed microstructure characterization of the synthesized material revealed that the non-modified ZrO_2 has both monoclinic and tetragonal phases, evidenced by characteristic XRD peaks at 28.2 and 31.5 degree (2θ) for monoclinic phase and at 30.3 degree (2θ) for tetragonal phase.^[19,20] Figure 2-1 shows the XRD patterns of various ZrO_2 -based mixed oxide catalysts.

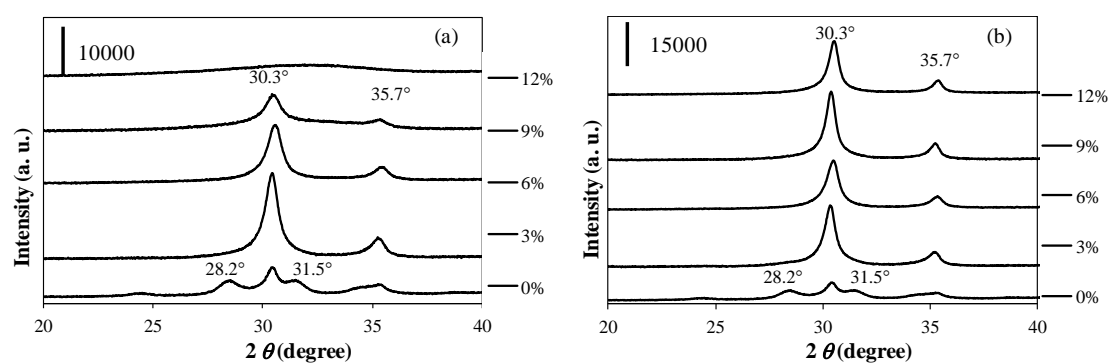


Figure 2-1 Powder XRD patterns of $Al_2O_3-ZrO_2$ (a) and $MgO-ZrO_2$ (b) mixed-oxides

As evidenced by XRD spectra patterns shown in Figure 2-1, the monoclinic phase is not present in the heteroatom modified ZrO_2 . Therefore, both Al_2O_3 and MgO doping favored the stabilization of the metastable tetragonal phase of the crystalline ZrO_2 . Precise measurements of unit-cell parameters indicated that the ZrO_2 crystal lattice suffered a contraction due to the intercalation of Mg^{2+} and Al^{3+} ions in the $\text{Zr}^{4+}\text{-O-Zr}^{4+}$ lattice, since the ionic radius of Mg^{2+} (0.86 Å) and Al^{3+} (0.68 Å) are considerably smaller than that of Zr^{4+} (0.98 Å).^[21] However, at low modification degrees till 12 mol % M^{n+} cation ($\text{M} = \text{Al}, \text{Mg}; n = 2, 3$; respectively), the increase of ion content only has a marginal influence on the unit cell volume of the mixed oxides. In all cases, no additional peaks attributed to the crystalline Al_2O_3 or MgO have been observed, indicating that Al and Mg are integral parts of the ZrO_2 framework. Based on the information obtained from XRD patterns of $\text{Al}_2\text{O}_3\text{-ZrO}_2$ and MgO-ZrO_2 materials, the existence of amorphous Al_2O_3 or MgO deposits on the surface of ZrO_2 or ZrO_2 -based solid solution could not be entirely excluded.

The specific surface areas determined from the N_2 adsorption-desorption isotherms at $-196\text{ }^\circ\text{C}$ by using Brunauer-Emmett-Teller method (Section 2.7.2, Figure 2-20) indicated that BET surface areas increased with increasing heteroatom doping in the range of 0 ~ 12 mol % in both cases of $\text{Al}_2\text{O}_3\text{-ZrO}_2$ and MgO-ZrO_2 . Moreover, the surface areas of materials, synthesized by the co-precipitation method with the heteroatom fraction as high as 12 %, were obviously larger than those of the mechanical mixtures of the two oxides. This can be either due to the heteroatom insertion into crystalline lattice of ZrO_2 leading to the formation of a solid solution or due to the formation of a new porous layer which covers the outer surface of the ZrO_2 crystal particles.

In order to further clarify if the formation of either a solid solution or of a new layer mainly contributes to the increase of the materials' specific surface area, the surface composition and binding energies of ZrO_2 and ZrO_2 -based mixed oxides were further

investigated by XPS. With the reported experimental parameters, XPS spectra of Mg 1s, Zr 3d, Al 2s and Al 2p were able to be obtained with high signal-noise ratio and without visible overlapping (Section 2.7.3, Figure 2-21). The characteristic Zr 3d peak corresponding to ZrO_2 was fitted into two contributions, *i.e.*, $3d_{5/2}$ and $3d_{3/2}$, with the intensity ratio of $\sim 3 / 2$, which is close to the theoretical value. For the position of the Zr 3d main peaks ($3d_{5/2}$ and $3d_{3/2}$), the obtained values also agreed well with the values reported in literature.^[22]

For the investigation of the surface composition, the integrated areas of Al 2s, Mg 1s and Zr 3d XPS signals in each spectrum were compared, as shown in Figure 2-2. In this respect, Al 2s and Mg 1s peak areas have been normalized to the Zr 3d peak area. In Figure 2-2, two different slopes were observed for different Al_2O_3 -doped ZrO_2 , indicating the formation of two distinct phases. In all samples with low Al doping degrees ($< 3\%$), the typical Al 2s peak area increased moderately, indicating the formation of an Al-O-Zr mixed oxide. However, at higher modification degrees ($> 3\%$), the Al 2s peak area increased more accentuated with increasing Al content (Figure 2-2 (a)), suggesting the formation of a different layer on the ZrO_2 surface. In the case of MgO doping, the Mg 1s peak area increased linearly with increasing Mg content in the crystalline ZrO_2 lattice (Figure 2-2 (b)). The binding energy values of Zr $3d_{5/2}$ over different ZrO_2 -based catalysts are listed in Table 2-1. As evidenced in Table 2-1, with increasing MgO content, Zr $3d_{5/2}$ binding energy values were shifted into lower values by approximately 1 eV, indicating the formation of a new Mg-O-Zr unit. By comparison, no similar shift was observed in the case of Al_2O_3 doping.^[23] Combining the experimental results of crystallinity measurements (XRD), pore volumes analysis (N_2 physisorption) and surface composition (XPS), it was shown that the insertion of Mg^{2+} into the ZrO_2 lattice leads to the formation of homogeneous solid solution in the case of MgO- ZrO_2 , while solid deposit on the ZrO_2 -based particles may exist only in the case of Al_2O_3 - ZrO_2 .

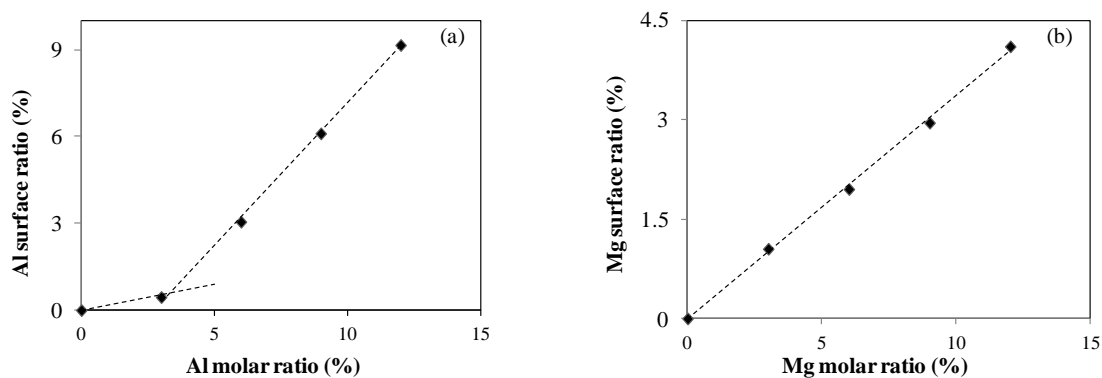


Figure 2-2 Influence of the molar fraction of Al_2O_3 (a) and MgO (b) on surface composition of the bimetallic oxide catalyst determined by surface XPS peak area analysis vs. bulk molar ratio

Table 2-1 Binding energy values of $\text{Zr } 3d_{5/2}$ over ZrO_2 -based catalysts (eV)

Modification ratio (%)	Al_2O_3 - ZrO_2	MgO - ZrO_2
0	182.6	182.6
3	182.5	182.4
6	182.7	182.1
9	182.6	181.9
12	182.7	181.8

It is well known that both acidic and basic sites are simultaneously present on the ZrO_2 surface.^[24] The incorporation of heteroatoms, however, not only influences the concentration and strength of crystalline ZrO_2 's acidic and basic sites, but can also lead to the generation of new sites. In this respect, a rigorous analysis of the synthesized mixed-oxides was made. As a first attempt to analyze the surface acidic sites, NH_3 -TPD measurements were performed. Important results, as summarized in Figure 2-3 and 2-4, evidenced that all the ZrO_2 -based materials contain only weak acidic sites. The use of Al_2O_3 for the synthesis of ZrO_2 -based oxides resulted in an increase of the overall surface acidic sites (Figure 2-3 (a) and 2-4 (a)). Comparison of the results obtained at low Al_2O_3 doping degree (< 3 %) showed that a decrease in the

acidic strength takes place upon incorporation of Al_2O_3 in the crystalline ZrO_2 framework and the formation of new Al-O-Zr units. At higher Al_2O_3 doping degree (> 3 %), the generation of a stronger acidic alumina layer on the outer surface of the parent materials was observed. Interestingly, all the MgO-ZrO₂ mixed oxides showed a lower maximum desorption peak of NH_3 and a narrower distribution, particularly in the case of the 12 % MgO-ZrO₂, than non-modified ZrO₂ (Figure 2-3 (b) and 2-4 (b)).

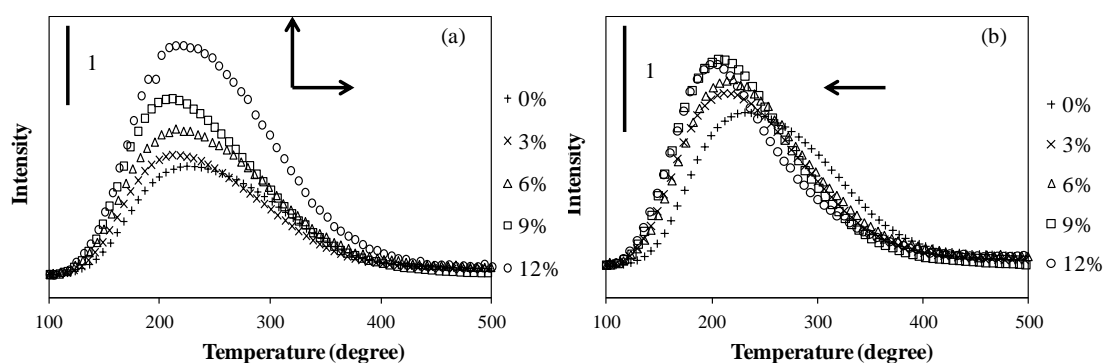


Figure 2-3 NH_3 -TPD profiles of all Al_2O_3 - (a) and MgO- (b) doped ZrO_2 catalysts

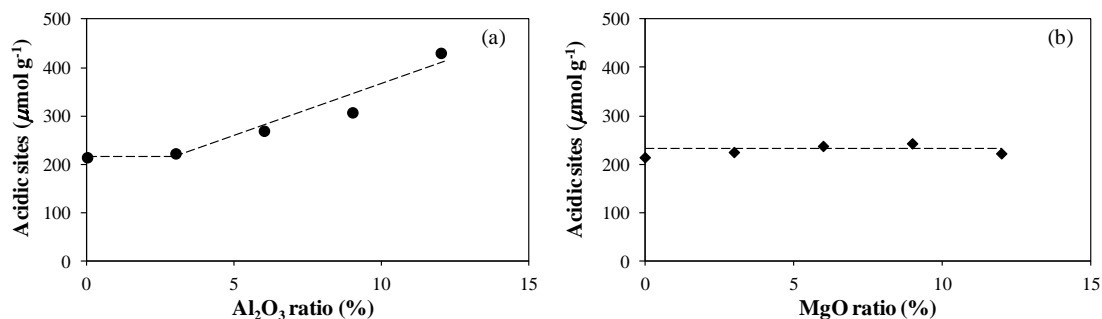


Figure 2-4 Concentrations of total acidic sites of Al_2O_3 - (a) and MgO- (b) doped ZrO_2 catalysts (determined by NH_3 -TPD)

Owing to the variety and heterogeneity of ZrO_2 oxide surfaces, the nature and concentration of acidic sites were analyzed by infrared spectroscopy of adsorbed pyridine. IR spectra of adsorbed pyridine on zirconia surfaces recorded at 150 °C are comparatively shown in Figure 2-5. The different nature of adsorbed pyridine on aprotic (Lewis) and protic (Brønsted) acidic sites could be distinguished by monitoring the characteristic pyridine ring vibrations. The contact of all ZrO_2 -based

catalysts with pyridine revealed typical bands in the range of $1400 \sim 1650 \text{ cm}^{-1}$. The band located at $\sim 1444 \text{ cm}^{-1}$ is assigned to a pyridine coordinatively bound to a Lewis acidic site (LAS), while the band at 1540 cm^{-1} attributed to pyridinium ion referring to surface Brønsted acidic sites (BAS) was not observed from any of the synthesized materials. In addition, a band at $\sim 1604 \text{ cm}^{-1}$, which can be assigned either to hydrogen-bonded or to coordinatively-bonded pyridine, was observed for all measured samples. [25] The total concentration of Lewis acidic sites determined by IR spectra of adsorbed pyridine is in good agreement with the NH_3 -TPD results, since none of the materials have surface BAS (Section 2.7.4, Figure 2-22).

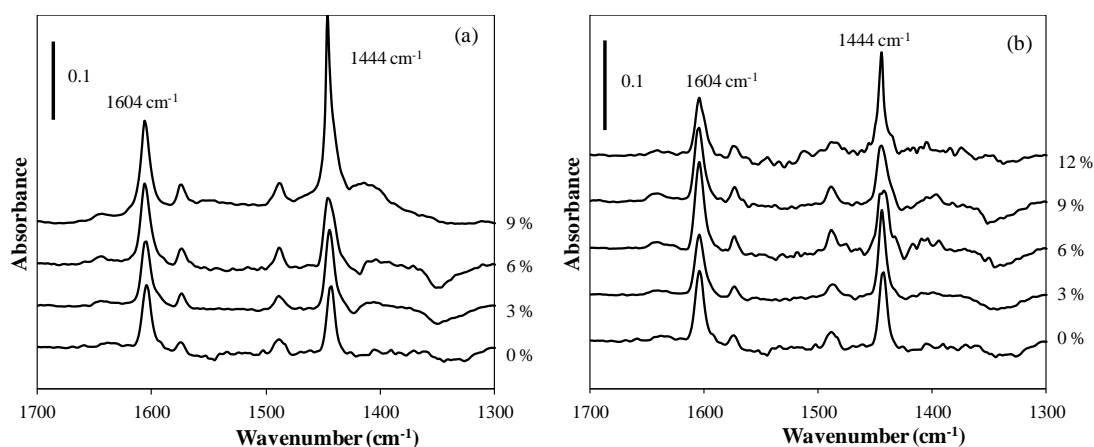


Figure 2-5 IR spectra of adsorbed pyridine on Al_2O_3 - (a) and MgO - (b) doped ZrO_2 catalysts

Temperature programmed desorption (TPD) of CO_2 was used to determine the concentration and the strength of basic sites on the surface of the synthesized catalysts. The CO_2 -TPD profiles and the concentration of basic sites for all ZrO_2 -based catalysts are illustrated in Figure 2-6 and 2-7.

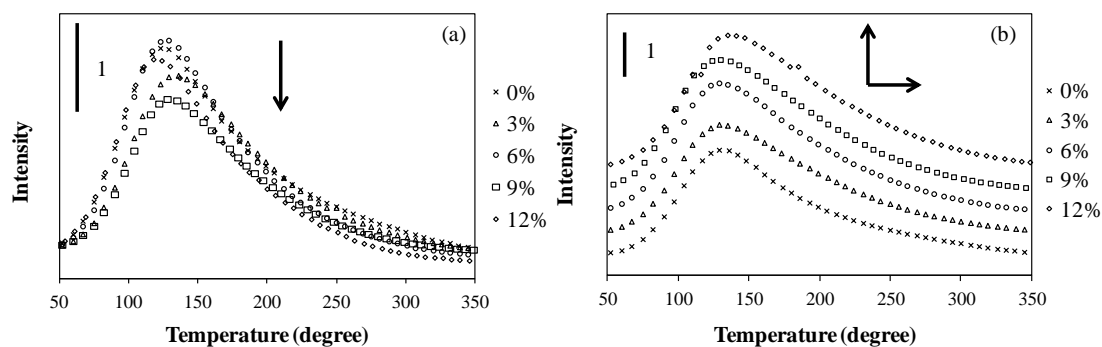


Figure 2-6 CO₂-TPD profiles of all Al₂O₃- (a) and MgO- (b) doped ZrO₂ catalysts

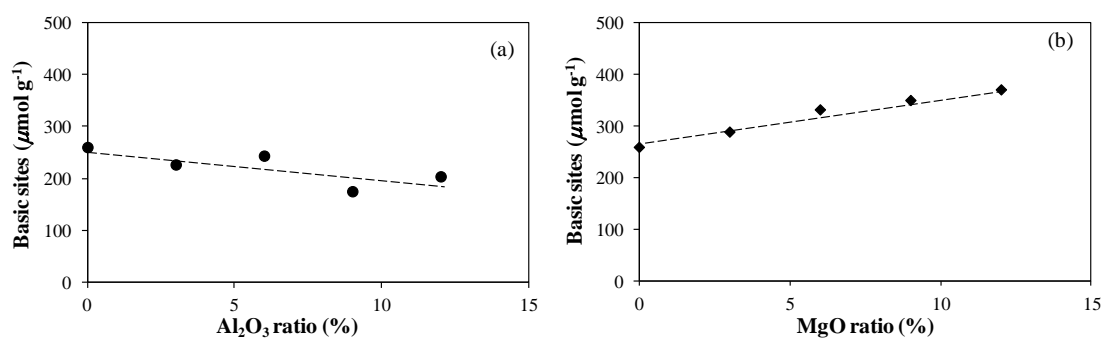


Figure 2-7 Concentrations of total basic sites of Al₂O₃- (a) and MgO- (b) doped ZrO₂ catalysts (determined by CO₂-TPD)

Comparative analysis results reveal that MgO-ZrO₂ catalysts exhibit a higher concentration of basic sites compared to the un-doped ZrO₂, while the concentrations of surface basic sites on Al₂O₃-ZrO₂ decreased with increasing Al₂O₃ modification. The strengths of basic sites stayed approximately constant in the case of Al₂O₃-ZrO₂ catalysts. However, in the case of MgO-ZrO₂, an obvious strengthening of the basicity, due to the formation of non-equivalent Mg-O-Zr bonds, was observed. A brief overview of surface acidic / basic sites on Al₂O₃- and MgO-doped ZrO₂ catalysts is shown in Table 2-2.

Table 2-2 Overview of surface acidic / basic sites on Al₂O₃- and MgO-ZrO₂ catalysts

Catalyst	Al ₂ O ₃ -ZrO ₂	MgO-ZrO ₂	Experimental evidence
Type of acidic sites	Lewis	Lewis	Py-IR*
Concentration of acidic sites	increase	constant	NH ₃ -TPD & Py-IR*
Strength of acidic sites	stronger	weaker	NH ₃ -TPD
Concentration of basic sites	decrease	increase	CO ₂ -TPD
Strength of basic sites	constant	stronger	CO ₂ -TPD

* Py-IR: IR spectroscopy of pyridine adsorption

2.3.2 Catalytic DMC formation over ZrO₂-based catalysts

Under typical reaction conditions, the concentration of DMC initially increased with increasing reaction time before reached an equilibrium level. In all performed reactions, DMC was the only detected product, while dimethyl ether (DME), the only possible by-product during DMC synthesis resulting from the Lewis acid catalyzed dehydration of methanol, was under the GC's detection limit. The initial rates of DMC formation were normalized to the catalyst amount and compared, as shown in Figure 2-8.

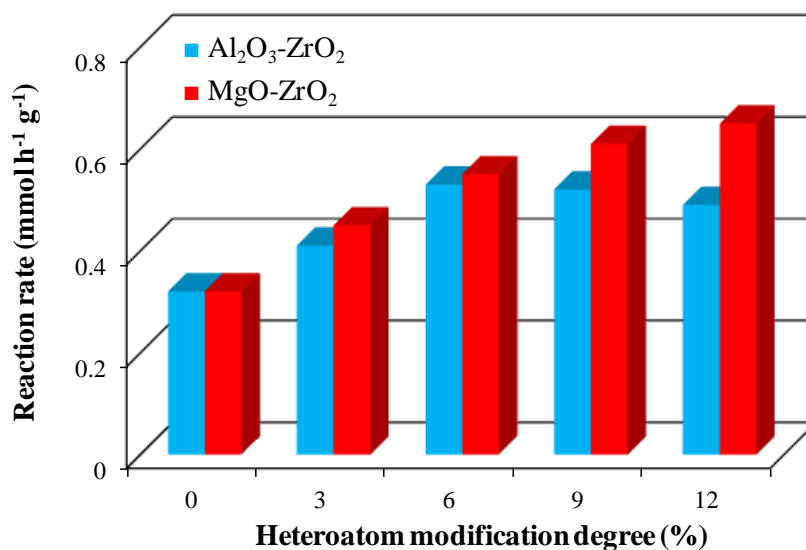


Figure 2-8 ZrO₂ catalyzed DMC formation from methanol and CO₂ (Reaction conditions: 39.6 g methanol, 10 g CO₂, 0.5 ~ 2 g catalyst, 160 °C, total pressure 42 bar.)

Compared to the ZrO₂ synthesized by the precipitation method and containing both monoclinic and tetragonal phases, both Al₂O₃- and MgO-doped mixed-oxides showed a considerably higher catalytic activity, indicating an important contribution of the heteroatoms to the formation and stabilization of the active sites. In the case of Al₂O₃-ZrO₂, the DMC formation rate was enhanced in the presence of ZrO₂ with low percentage of Al₂O₃ doping, reaching a maximum at 6 % concentration at which the outer-sphere Al₂O₃ deposition becomes accentuated (Figure 2-8). Further increase of Al₂O₃ content in the ZrO₂ led to a noticeable decrease on the catalytic activity. In contrast to that, all the MgO-ZrO₂ mixed-oxide catalysts showed approximately two times higher catalytic activities with increasing doping degree.

As one of the most important kinetic features relevant for understanding the nature of interactions between the reactant molecules and catalysts, the reaction orders of both reactants, *i.e.*, methanol and CO₂, were determined by using the double logarithmic plots of the initial rates of DMC formation *vs.* the starting concentration of the corresponding reactant (Section 2.7.5, Figure 2-23 and 2-24). A summary of the

observed reaction orders for both reactants is shown in Table 2-3.

Table 2-3 Observed reaction orders for methanol and CO₂ on ZrO₂-based catalysts

Catalyst	methanol reaction order	CO ₂ reaction order
ZrO ₂	0.06	1.10
3 % Al ₂ O ₃ -ZrO ₂	0.12	1.03
6 % Al ₂ O ₃ -ZrO ₂	-0.05	1.05
9 % Al ₂ O ₃ -ZrO ₂	0.08	1.08
3 % MgO-ZrO ₂	-0.07	1.03
6 % MgO-ZrO ₂	0.02	0.95
12 % MgO-ZrO ₂	0.03	0.89

Reaction conditions: methanol amount varied from 25 g to 50 g, CO₂ amount varied from 5 g to 12 g, reaction temperature 160 °C.

For ZrO₂ synthesized according to the precipitation method, selected as a benchmark for comparison, the DMC formation shows first-order dependence from CO₂ and zero-order dependence from methanol. Kinetic analysis of catalyzed DMC formation revealed that Al₂O₃ doping has no impact on the observed reaction orders for methanol and CO₂. In the case of MgO-ZrO₂ catalysts, the reaction order of methanol was zero, while the overall reaction order of CO₂ decreased with increasing MgO doping degree. This considerable difference concerning the observed reaction order of CO₂ indicate that a more favorable CO₂ activation occurs on the stronger Lewis basic sites of MgO-ZrO₂ catalysts.

It is of essential importance for catalysis to have a good understanding on the elementary steps of CO₂ conversion. The nature of active intermediates on metal oxides surfaces induced by CO₂ interaction was studied in previous research works.

[15] On the surface of metal oxides, the interaction with CO₂ normally leads to different activated forms of the C=O bond, further resulting in the formation of various carbonate species, *i.e.*, non-coordinated, monodentate and bidentate carbonate or bicarbonate. Nonetheless, the reactivity of those species or, more specifically, the contribution of each species to the catalytic DMC formation, has not been reported previously. In addition, MgO-ZrO₂ catalysts showed not only higher activities, but also different kinetic behaviors compared to ZrO₂ and Al₂O₃-ZrO₂. In order to analyze the complex surface reactions enabled on the active sites, comparative temperature-dependent IR measurements on the reactants adsorption and transient formation of reactive intermediates were carried out between the most active MgO-ZrO₂ catalyst and non-modified ZrO₂ catalyst.

First, to understand the elemental activation processes enabled on the catalyst surface, *in-situ* IR studies on the methanol and CO₂ adsorption were performed. Figure 2-9 shows the IR spectra of adsorbed methanol under different measurement conditions.

The interaction of methanol with the active surface of ZrO₂ was investigated by exposing ZrO₂ to methanol vapor for 30 min at 40 °C. The molecular adsorption of methanol primarily occurred on the coordinatively unsaturated Zr⁴⁺, a Lewis acidic site located on the ZrO₂ catalyst surface, to form methoxide species having characteristic bands at 2925 cm⁻¹ and 2825 cm⁻¹ (typical C-H stretching vibration bands of a methoxide species).^[26, 27] In addition to that, two small bands at 2940 and 2840 cm⁻¹ clearly indicated the presence of molecularly adsorbed methanol on ZrO₂ surface. By analyzing the IR spectra recorded during temperature-programmed evacuation of methanol-adsorbed catalyst surface at various temperatures, as noted in Figure 2-9, it was possible to show that the intensities of the characteristic bands for C-H stretching in methoxide species (2925 cm⁻¹ and 2825 cm⁻¹) were almost unchanged over the selected temperature range under the conditions that the physisorbed methanol was entirely removed. The same methanol activation process

was observed in the case of both ZrO_2 and MgO-ZrO_2 catalysts.

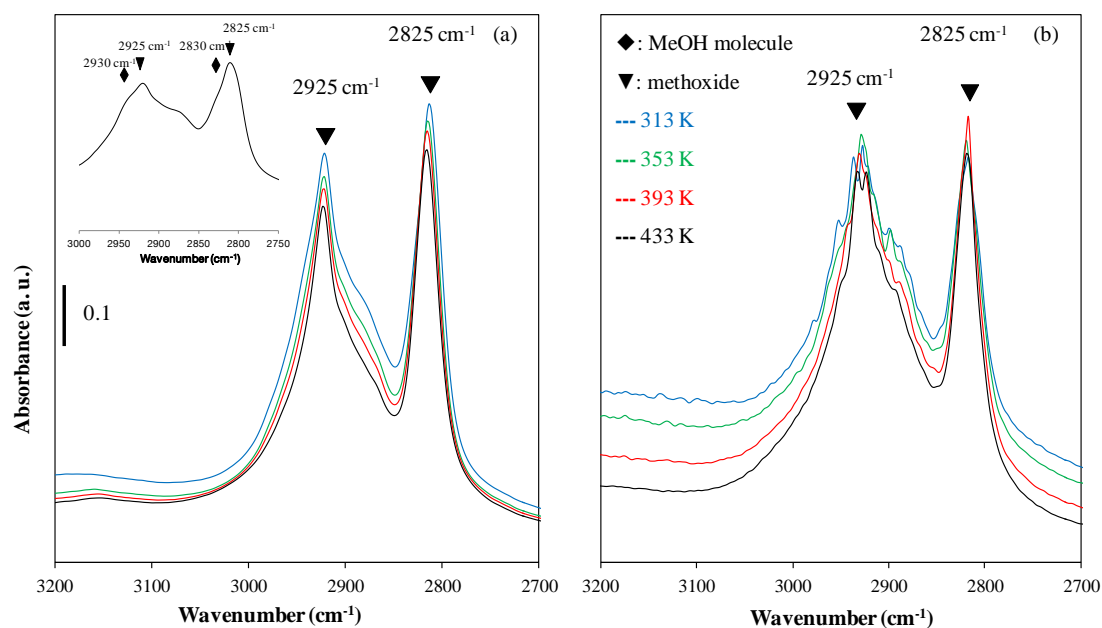


Figure 2-9 IR spectra of adsorbed methanol on ZrO_2 (a) and 12 % MgO-ZrO_2 (b) (The inset in Figure 2-9 (a) shows the spectrum recorded immediately after methanol dosage on ZrO_2 . Further spectra were recorded during the temperature programmed desorption from 40 $^{\circ}\text{C}$ to 160 $^{\circ}\text{C}$.)

The interaction of CO_2 with the active catalyst surface was investigated by exposing ZrO_2 -based materials to CO_2 for 30 min at 40 $^{\circ}\text{C}$. The IR spectra taken during adsorption and evacuation on different catalysts are shown in Figure 2-10.

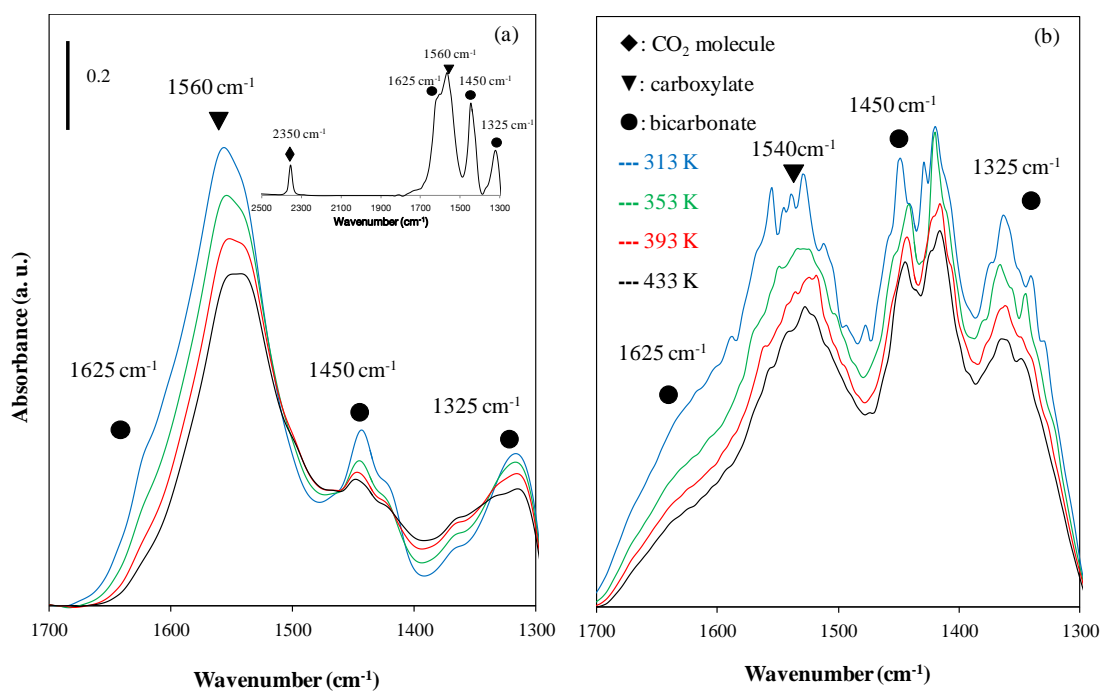


Figure 2-10 IR spectra of adsorbed CO₂ on ZrO₂ (a) and 12 % MgO-ZrO₂ (b) (The figure inset shows the spectrum recorded immediately after CO₂ adsorption on ZrO₂. Further spectra were acquired during the temperature programmed desorption at temperature range between 40 °C and 160 °C.)

CO₂ adsorption on the ZrO₂ surface led to the formation of bidentate bicarbonate species with characteristic IR bands at 1625 cm⁻¹, 1450 cm⁻¹ and 1325 cm⁻¹, as well as to the transient formation of bidentate carboxylate species with a typical IR band at 1560 cm⁻¹. The band at 2350 cm⁻¹ indicated the presence of free molecular CO₂. After evacuation, the characteristic bands of transiently formed surface species, *i.e.*, bidentate bicarbonate and bidentate carboxylate, were observed, while the band at 2350 cm⁻¹ corresponding to gas-phase CO₂ diminished. However, the intensities of both bidentate bicarbonate and bidentate carboxylate species depressed considerably, indicating a significantly lower stability on CO₂-induced intermediates compared to the surface methoxide. Moreover, the intensity of characteristic bands assigned to bidentate bicarbonate species decreased more than that of the bands assigned to bidentate carboxylate species, directly evidencing that bidentate bicarbonate has a lower stability on ZrO₂ surface compared to the bidentate carboxylate. By analyzing the IR spectra recorded during temperature-programmed evacuation of CO₂-adsorbed

catalyst surface at various temperatures (Figure 2-10), the intensities of characteristic bands of the transiently formed intermediates in the range between 1700 cm^{-1} and 1300 cm^{-1} decreased with increasing temperature but still existed at high temperatures. MgO doping resulted in a considerable increase in the CO_2 activation and formation of stable bidentate bicarbonate species on the catalyst surface.

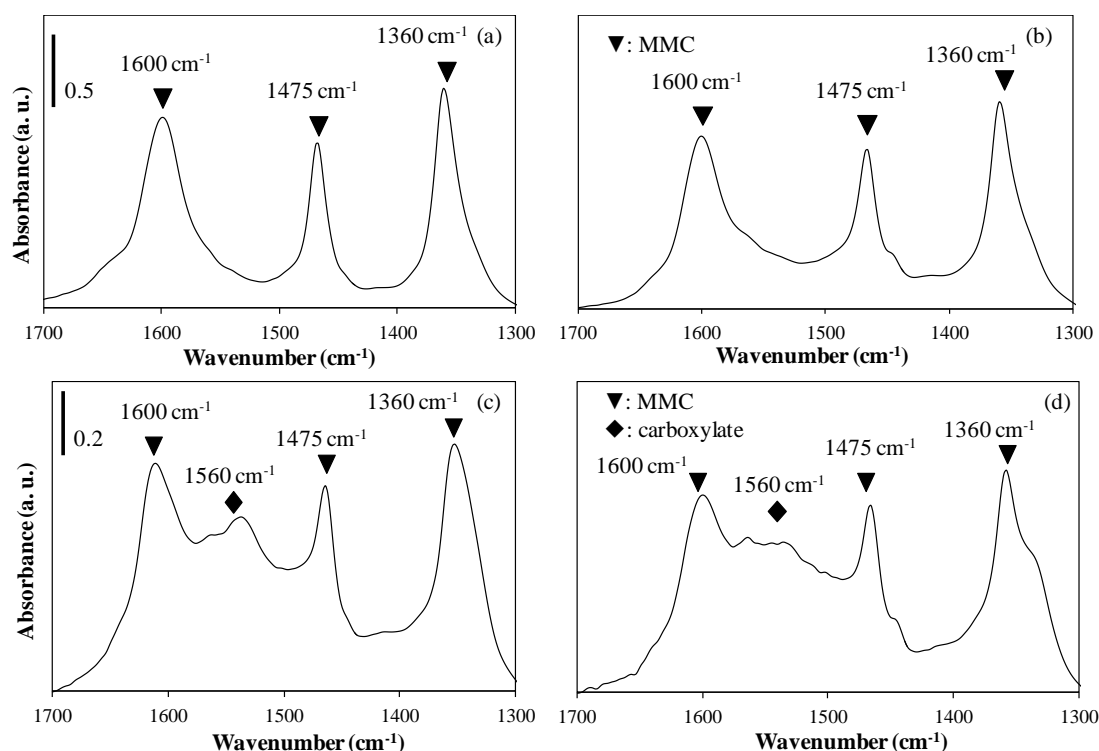


Figure 2-11 IR spectra recorded after CO_2 adsorption on a methanol-saturated ZrO_2 surface before (a) and after (b) evacuation at 10^{-6} mbar and $40\text{ }^\circ\text{C}$ as well as IR spectra recorded after methanol adsorption on a CO_2 -saturated ZrO_2 surface before (c) and after (d) evacuation at 10^{-6} mbar and $40\text{ }^\circ\text{C}$

In a dynamic catalytic reaction, methanol and CO_2 are simultaneously present in the reaction mixture. Therefore, it was of crucial importance to have IR measurements designed to understand the formation of active species under real catalytic conditions. In this respect, IR spectra were recorded when methanol or CO_2 was added in a consecutive step after another reactant was already pre-adsorbed on the ZrO_2 surface. In the case of a subsequent CO_2 addition to a methanol saturated surface, the new bands at 1600 cm^{-1} , 1475 cm^{-1} and 1360 cm^{-1} , corresponding to C=O stretching, C–H

bending and O–C–O stretching modes of surface MMC species were detected (Figure 2-11 (a)). It is important to note that the absence of a surface carboxylate directly points to a competitive adsorption of methanol on those sites where carboxylate formation is facilitated (coordinatively unsaturated Zr^{4+} in close proximity of a surface -OH). In the case of a consecutive methanol addition to the CO_2 pre-treated ZrO_2 catalyst, the rapid formation of MMC occurred. On the other hand, the initial IR bands of the CO_2 -induced bidentate bicarbonate species' characteristic IR bands decreased, while those belonging to bidentate carboxylate remained almost unchanged (Figure 2-11 (b)). This implies that, on the surface of ZrO_2 catalyst, solely bidentate bicarbonate is involved in the formation of surface MMC species.

As one of the main mechanistic aspects, whether CO_2 participates in the reaction following a Langmuir-Hinshelwood (LH) or an Eley-Rideal (ER) mechanism, there is still no consensus reached. In one of the previous scientific reports, the authors stated that the overall reaction of DMC formation from methanol and CO_2 over ZrO_2 catalyst involves the direct reaction of adsorbed methanol with the non-activated CO_2 from the gas phase.^[28] In this case, the main intermediate, monomethyl carbonate, can be formed by CO_2 insertion into the metal-oxygen bond of methoxide species following an Eley-Rideal surface reaction mechanism. In the opinion of other researchers, the LH mechanism would account better for the experimental observations, *i.e.*, CO_2 adsorbed on certain surface active sites is mainly involved in MMC formation, although the active sites required for CO_2 adsorption and the formation of active intermediates were not specified.^[29, 30] In the present study, an accurate analysis of all the experimental data revealed that MMC formation takes place following LH model. This assumption is supported by the following fact that the CO_2 chemisorption on the surface Lewis basic sites leads to the concomitant formation of active intermediates, which are rapidly converted to MMC as methanol is added.

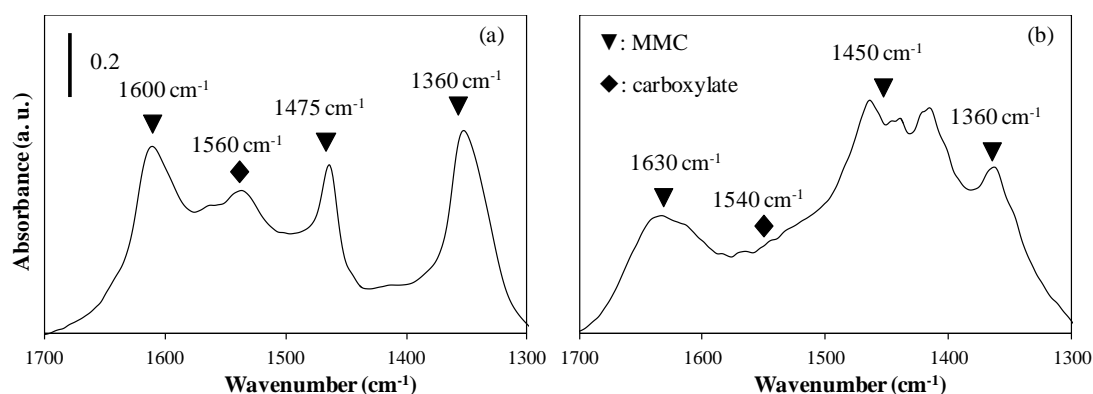


Figure 2-12 IR spectra of methanol addition to a CO_2 -saturated surface of ZrO_2 (a) and 12 % MgO-ZrO_2 (b) catalysts

It is worth mentioning that, compared to ZrO_2 , in the case of MgO-ZrO_2 , the characteristic bands of the transiently formed surface intermediates are shifted, due to the different Lewis basic properties of the tested catalysts (Figure 2-12). In order to investigate the stability of the surface species, temperature dependent *quasi*-static IR measurements were conducted following the evacuation of the selected catalysts. The IR spectra of the MMC adsorbed on ZrO_2 and MgO-ZrO_2 catalysts (with bands assigned to C=O stretching, C-H bending and O-C-O stretching modes) recorded at different temperatures are comparatively shown in Figure 2-13.

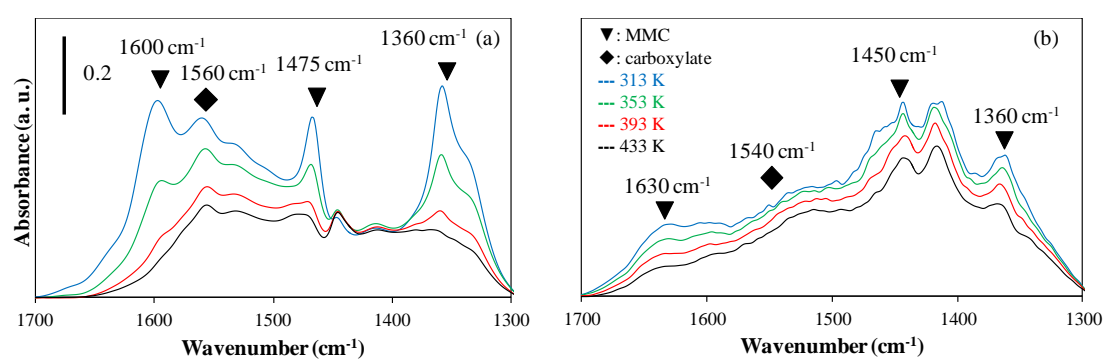


Figure 2-13 IR spectra of surface MMC species on ZrO_2 (a) and MgO-ZrO_2 (b) catalysts during temperature-programmed evacuation (Spectra from the top to the bottom were recorded at gradually increased temperatures from 40 °C to 160 °C. Surface MMC species was formed via methanol exposure to CO_2 -saturated surface. All spectra were recorded in the absence of free molecular CO_2 .)

As shown in Figure 2-13, following methanol addition to CO₂-saturated ZrO₂, the formation of MMC species from bidentate bicarbonate and methanol takes place rapidly. It is important to note that a conversion of bidentate carboxylate is solely occurring in the case of more basic MgO-ZrO₂ catalyst. High temperature IR measurements further indicate that MMC formed on active ZrO₂ surface under reaction conditions ($T = 160\text{ }^{\circ}\text{C}$) is not stable and quickly leads to the back formation of the starting materials. Therefore, at high temperature, MMC on ZrO₂ was only exists in the presence of free gas-phase CO₂ (Figure 2-14), required to shift the adsorption equilibrium of CO₂ and enhance the formation of bicarbonate species. In this case, the formation of the surface bidentate carboxylate was not affected by the addition of free gas-phase CO₂ and was stable over the selected temperature range. In the absence of gas-phase CO₂, the stabilization of MMC was enabled only on the active sites of MgO-ZrO₂ catalyst.

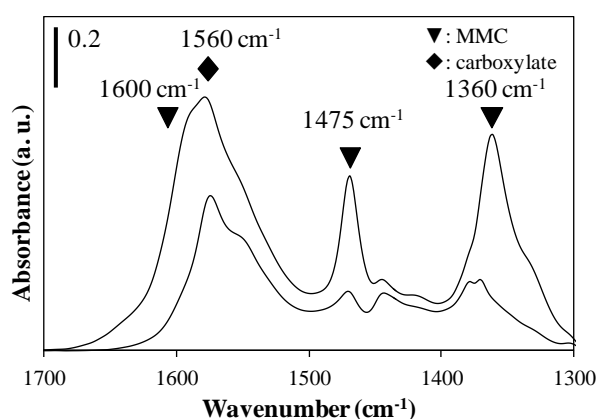


Figure 2-14 IR spectra of surface MMC species on ZrO₂ with (top) and without (bottom) gas phase CO₂ at 160 °C

Even if it has been experimentally confirmed that MMC is formed, following the activation of both methanol and CO₂, its further conversion to DMC is still not well understood. In some previous contributions, MMC was similarly considered as the main intermediate involved in the DMC synthesis. ^[14, 31] However, in the case of ZrO₂-CeO₂ mixed oxide catalyzed reaction, during a Ce³⁺ / Ce⁴⁺ redox catalytic cycle,

a formate surface species was considered as a key intermediate in DMC formation.^[32] In order to shed more light on the ZrO_2 catalyzed reaction, DMC was used as adsorbate and the formation of surface active species was monitored by *in-situ* IR measurements (Figure 2-15).

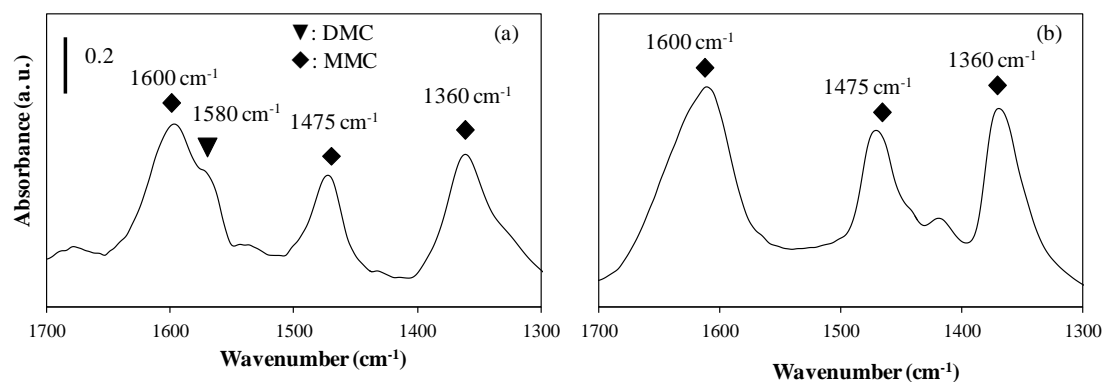


Figure 2-15 IR spectra of ZrO_2 exposed to DMC (Spectrum (a) was recorded immediately after exposure to DMC and spectrum (b) was recorded after exposure to DMC followed by the evacuation of the system at 40 °C.)

The results obtained by careful analysis of the experimental data from IR spectroscopic measurements confirmed that MMC co-exists in a dynamic equilibrium with molecular DMC (characteristic IR band at 1580 cm^{-1}) on the surface. However, if methanol and CO_2 were directly used as adsorbates, a rather low amount of DMC was formed, and the only distinct DMC band at 1580 cm^{-1} appeared only as a weak band next to the main C=O stretching band at 1600 cm^{-1} . It is important to note that the simultaneously formed water, however, disturbs the IR spectral patterns. Thus, to track DMC molecule formed in a forward reaction, the co-existence of water has to be avoided. Therefore, in the next measurements, dimethyl ether (DME) was used as a probe molecule. The IR spectrum after DME, CO_2 and methanol adsorption, as shown in Figure 2-16, clearly demonstrates the co-presence of molecular DMC (1580 cm^{-1}) with MMC, evidencing that MMC is the main intermediate in the DMC formation.

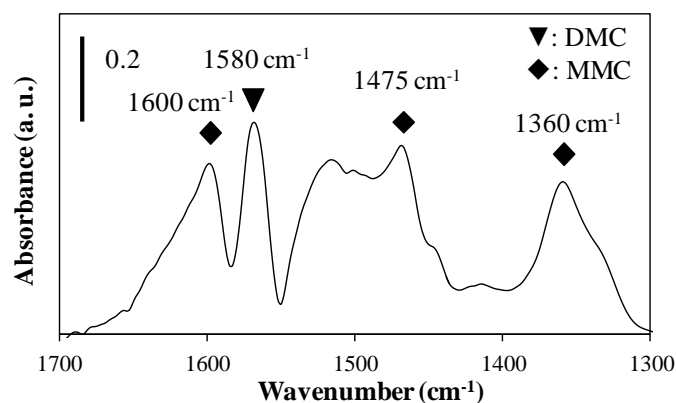


Figure 2-16 IR spectrum of ZrO₂ catalyst after exposure of stepwise DME, CO₂ and methanol

The chemical stability of the most active catalyst for the DMC synthesis was studied by repeating the catalytic cycle for 6 times (Figure 2-17, and more results on stability test are available in Section 2.7.6, Figure 2-25).

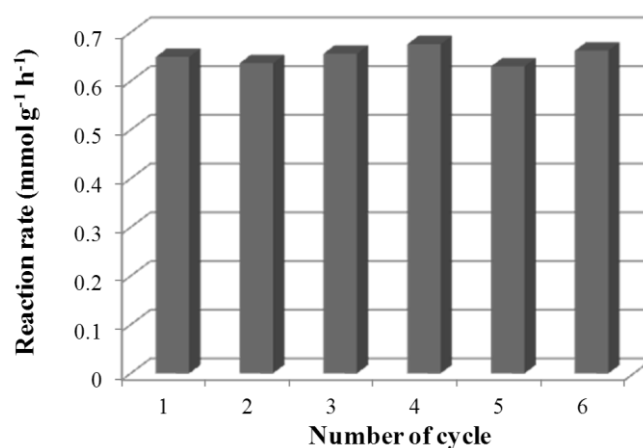


Figure 2-17 MgO-ZrO₂ stability studied over 6 catalytic runs (Reaction conditions for each reaction cycle: 12 % MgO-ZrO₂ catalyst, 39.6 g methanol, 10 g CO₂, $T = 160$ °C.)

After each run of the catalytic reaction, the existence of homogeneous ZrO₂-based organometallic complexes was excluded based on the ICP-OES analysis (available in Section 2.7.7).

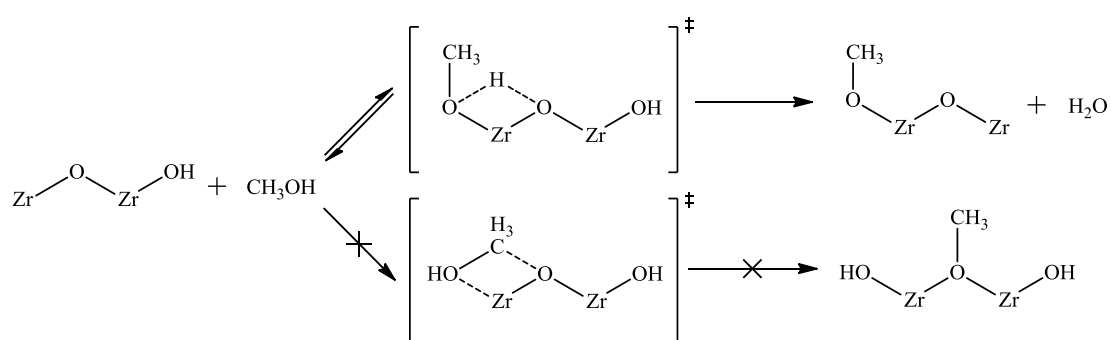
2.4 Discussion

Catalytic formation of DMC from methanol and CO₂ is a reaction with high atomic economy. Among various metal oxide catalysts, ZrO₂ is particularly promising, owing to its acidic / basic bi-functional properties. Elaborated experimental work on the structure optimization of the metal oxides evidenced that it is possible to prepare highly active ZrO₂-based mixed oxide catalysts with long-term operational stability by a simple co-precipitation method. Heteroatom modification of ZrO₂ stabilizes the more active tetragonal phase of ZrO₂ and modulates the acidic / basic properties on the surface (the comparison of different phases is available in Section 2.7.8). Moreover, MgO doping leads to the formation of a homogeneous Mg-O-Zr solid solution and an increase of surface basic sites which are essential for the activation of a thermodynamically and chemically inert CO₂. In contrast to MgO modification, evidenced by XPS measurements, high Al₂O₃ addition to ZrO₂ resulted in the formation of an amorphous monolayer on the outer ZrO₂ surface and caused a decrease in the surface basic sites.

The catalytic transformation involves methanol adsorption, CO₂ activation, transient MMC formation and its conversion to DMC followed by desorption. The formation and release of water, another product molecule in this reaction, takes place during the methanol adsorption as well as during MMC and / or DMC formation. Among all elementary steps, the adsorption of CO₂ and MMC formation were identified as possible rate determining steps (detailed discussion on rate determining step identification is available in Section 2.7.12).

The adsorption of methanol primarily takes place on the Lewis acidic site of the ZrO₂ catalyst. Adsorption of methanol occurs via its oxygen atom to the coordinatively unsaturated Zr⁴⁺ cations, leading to the formation of stable methoxide (Zr-O-CH₃) and

the release of H₂O following the consecutive protonation of a surface hydroxyl group (the determination of coordinatively unsaturated Zr⁴⁺ site and transformation of hydroxyl group are available in Section 2.7.9 and 2.7.10, respectively). In addition to that, Lewis basic sites (O²⁻ center) could similarly contribute to the methanol activation and formation of surface methoxide species. The proposed reaction pathways of methanol adsorption and activation are shown in Scheme 2-3, which is in accordance with previous publications.^[32, 33]

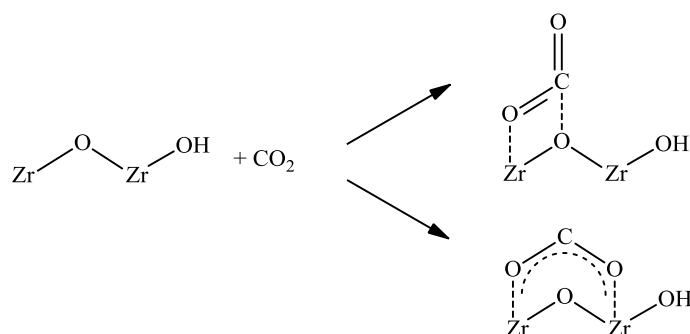


Scheme 2-3 Proposed methanol activation pathways on ZrO₂ catalyst

Detailed kinetic analysis along with results from IR spectroscopic studies evidenced that the rapid methanol activation preferentially takes place on Lewis acidic sites located on the catalyst surface, especially on the edge and terminal positions where coordinatively unsaturated sites are located. Overall, the presence of surface Lewis acidic sites is required for methanol activation, but it has no impact on the overall reaction rate, since methanol activation (adsorption) is not a rate determining step and has an observed reaction order of zero. Furthermore, based on the experimental observation, the possibility of methanol activation on the Lewis basic site can be completely ruled out.

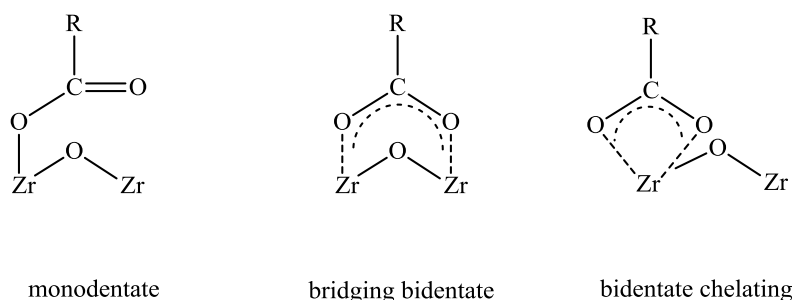
In the second step, CO₂, as a weak acidic molecule, is adsorbed on the Lewis basic sites and leads to the formation of the bidentate carbonate and / or bidentate

carboxylate as depicted in Scheme 2-4.



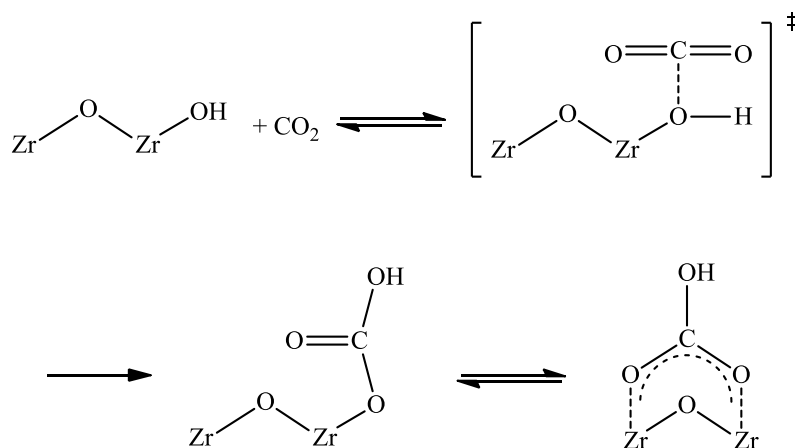
Scheme 2-4 CO₂ adsorption on the ZrO₂ catalyst surface

Considering the binding possibilities of a carboxylate ion, the existence of the following surface species can be assumed (Scheme 2-5).



Scheme 2-5 Coordination types of carboxylate ligands on the ZrO₂ catalyst surface (R = -H, -CH₃, *etc.*)

Furthermore, in the presence of basic surface terminal hydroxyl groups in close vicinity of a Lewis basic site, the insertion of the CO₂ molecule into a reactive surface hydroxyl bond and the subsequent formation of bicarbonate species might similarly be favored on the surface. In this transformation, CO₂ is activated by the basic O²⁻ center of a hydroxyl group, forming the [OH-CO₂] adduct in the transition state which is further converted into surface bicarbonate species, as depicted in Scheme 2-6. ^[34, 35]

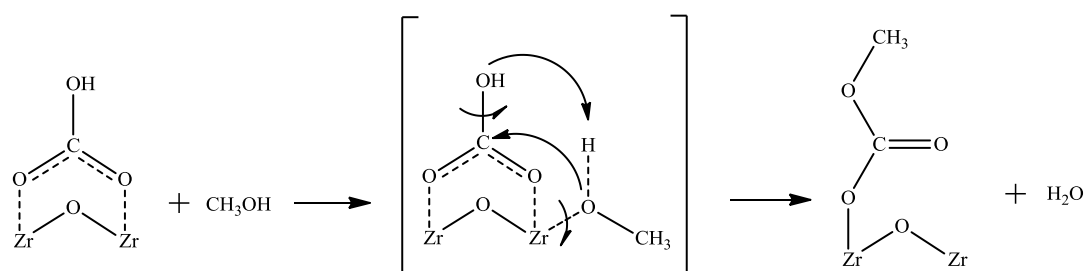


Scheme 2-6 CO₂ activation and formation of bicarbonate species

The stability of bicarbonate and bidentate carbonate on ZrO₂ is rather low, especially at high temperature (160 °C). Therefore, under reaction conditions, the surface coverage of reactive intermediates is low and directly proportional to the CO₂ partial pressure. This situation is, however, different in the case of carboxylate intermediates. Nevertheless, it is important to mention that the formation of carboxylate is considerably hindered in a methanol abundant environment due to the preferred competitive adsorption of methanol on the same active sites. These mechanistic assumptions are strongly supported by the observed first order of CO₂. The modification of MgO in the ZrO₂ lattice enhances the electron density of the neighboring basic O²⁻, favoring the CO₂ adsorption on the Lewis basic sites. The observed slight depression of CO₂ reaction order with MgO-ZrO₂ catalysts can be explained by the better accommodation and activation of CO₂ on the more and stronger basic sites.

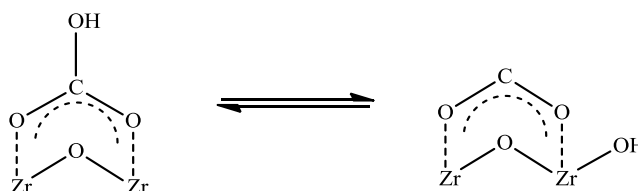
Immediately after intermediate surface-active compounds are formed, the driving force for monomethyl carbonate (MMC) generation is the nucleophilic attack of the oxygen atom of the activated methanol on the electrophilic carbon of surface bicarbonate resulted after CO₂ activation (Scheme 2-7). Noteworthy, the concurrent formation of water was also evidenced by the results of IR measurements (available in

Section 2.7.11).



Scheme 2-7 Surface reaction between adsorbed species of CO₂ and methanol

As evidenced by NH₃-TPD, the strength of Lewis acidic sites of ZrO₂-based catalysts is weakened by MgO doping, so that the reactivity of the activated methanol is considerably increased. This effect counts for the increased reaction rate in the case of MgO-ZrO₂. Moreover, with MgO modification, the dynamic equilibrium between bidentate bicarbonate and carboxylates is favored (Scheme 2-8).



Scheme 2-8 Dynamic equilibrium between surface bidentate bicarbonate and bidentate carboxylate species

In the case of bidentate bicarbonate, compared to bidentate carboxylate species, the neighboring electronegative oxygen atom in the hydroxyl group makes the electropositive carbon more susceptible for nucleophilic additions. Although bidentate carboxylate species has almost no reactivity on ZrO₂ catalyst, by doping with MgO, due to the strong electron donating ability of Mg²⁺, an increased electron density on oxygen atom of the methoxide species is similarly able to further drive the surface reaction.

To further strengthen that MgO doping not only allows a better accommodation and activation of CO₂, but also enables a higher surface coverage concomitantly contributing to the enhancement of the reaction rate constants, the overall rate of DMC formation was normalized to the accessible Lewis basic sites where CO₂ adsorption and following MMC formation occur (Figure 2-18).

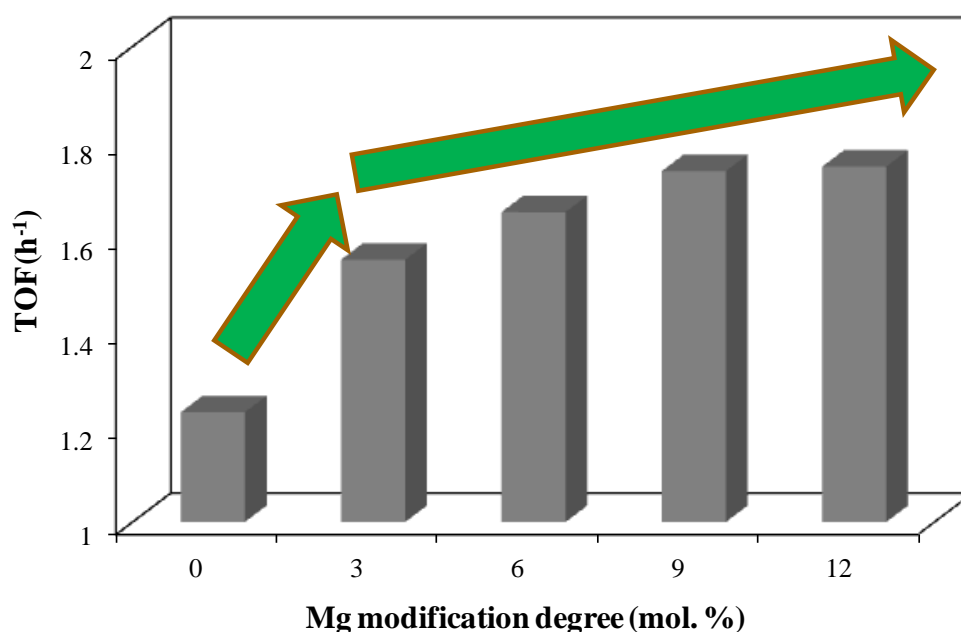
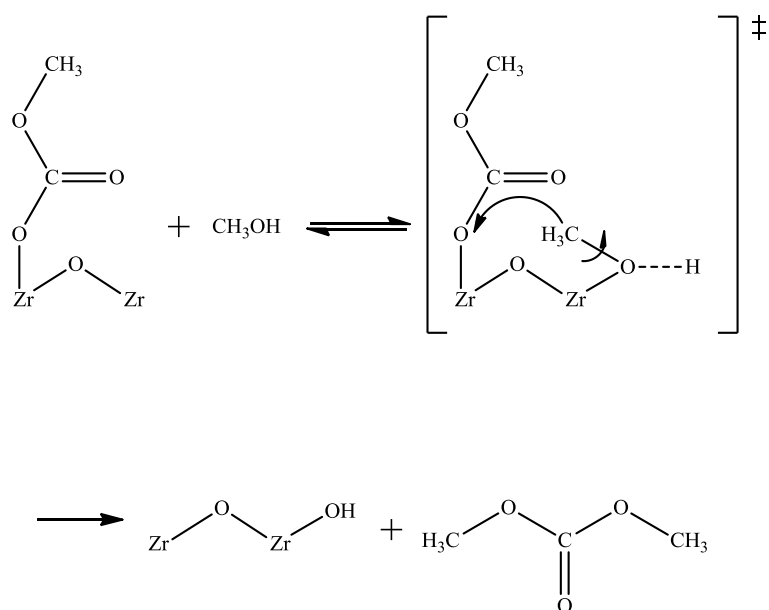


Figure 2-18 DMC formation from methanol and CO₂ over MgO-ZrO₂ catalysts (Reaction conditions: 39.6 g methanol, 10 g CO₂, 160 °C, total pressure 42 bar. The reaction rate is normalized to the concentration of Lewis basic sites determined by CO₂-TPD.)

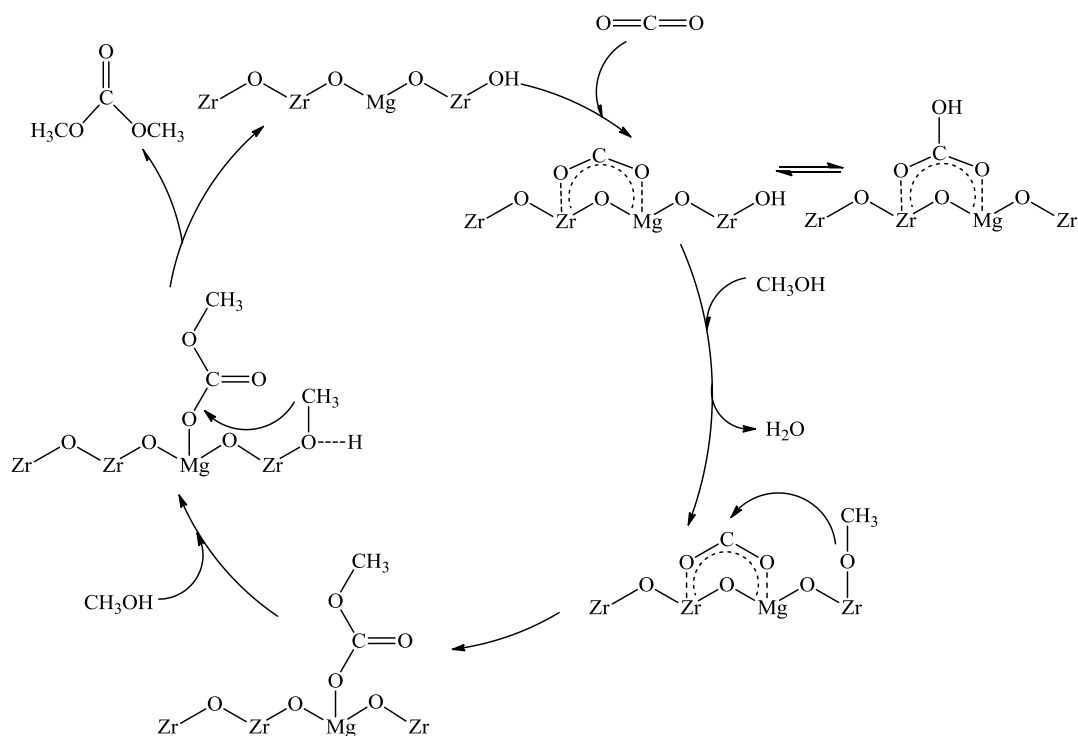
The results clearly evidence an increase in the catalytic activity with increasing MgO modification degree (TOF for ZrO₂ is 1.23 h⁻¹, while for 12 % MgO-ZrO₂ is 1.75 h⁻¹). The influence of MgO doping on CO₂ involved surface reactions (possible rate determining steps) was further evaluated by calorimetric measurements (Section 2.7.13, Figure 2-30). Compared to ZrO₂, higher heats for the rate determining steps were observed when MgO-ZrO₂ catalysts were used, suggesting that the rate determining steps are energetically favored on MgO-ZrO₂.

It is observed from *in-situ* IR measurements that the interaction between methanol molecule and surface MMC rapidly leads to the formation of DMC. Moreover, the interaction between DMC molecule and an activated ZrO_2 catalyst is able to form MMC on the surface. Thus, the DMC formation following the transesterification of surface MMC species with methanol has been demonstrated. In the absence of a vicinal surface -OH group, the protonation of the nucleophilic oxygen in methanol molecule cannot be avoided. Therefore, it can be proposed that the release of CH_3^+ able to further react with the nucleophilic oxygen of the MMC directly bound to the surface, leading to the formation of DMC and regeneration of initial active sites (Scheme 2-9). This reaction mechanism is in agreement with previous work of Pápai *et al.* [9]



Scheme 2-9 DMC formation from MMC and methanol

The proposed overall mechanism summarizing the most important experimentally evidenced reactions on the best performing MgO modified catalyst is presented in Scheme 2-10.



Scheme 2-10 Proposed reaction sequence for DMC formation on MgO-ZrO₂ catalyst

2.5 Conclusion

The rate of ZrO₂-catalyzed DMC formation from methanol and CO₂ has been considerably improved by using newly developed catalysts. It was proved that one important aspect of an efficient catalyst is the concomitant presence of acidic and basic sites on the active material surface. Homogeneous distribution of the new active sites created by heteroatom (Al, Mg) insertion on a highly crystalline ZrO₂ surface were proved to have an important impact on the optimization of the catalyst performance. Critical parameters and key intermediates have been identified and studied by using advanced spectroscopic techniques. It has been shown that new basic active sites considerably favor CO₂ adsorption and activation on the surface. Following methanol adsorption and formation of reactive methoxide species, MMC, a key intermediate, is formed, following the reaction with a surface bicarbonate or carboxylate accommodated on MgO-ZrO₂ surface. Higher activity of MgO-ZrO₂ catalyst is attributed to the higher CO₂ coverage caused by stronger basic sites as well

as to the higher efficiency of nucleophilic attack from oxygen to carbon.

2.6 References

- [1] Y. Zhou, S. Wang, M. Xiao, D. Han, Y. Lu, Y. Meng, *J. Clean Prod.* **2015**, *103*, 925
- [2] H. Babad, A. G. Zeiler, *Chem. Rev.* **1973**, *73*, 75
- [3] U. Romano, R. Tesei, M. M. Mauri, P. Rebora, *Ind. Eng. Chem. Prod. Res. Dev.* **1980**, *19*, 396
- [4] H.J. Buysch, A. Klausener, R. Langer, F. J. Mais, *US Patent*, **1993**, 5231212
- [5] T.A. Ryan, C. Ryan, E.A. Seddon, K.R. Seddon, *Phosgene and related carbonyl halides*, Elsevier, Amsterdam, **1995**
- [6] N. Keller, G. Rebmann, V. Keller, *J. Mol. Catal. A: Chem.* **2010**, *317*, 1
- [7] U. Romano, R. Tesel, G. Cipriani, L. Micucci, *US Patent*, **1980**, 4218391
- [8] G. Paret, G. Donati, M. Ghirardini, *EP Patent*, **1991**, 460735
- [9] M. Aresta, A. Dibenedetto, C. Pastore, A. Angelini, B. Aresta, I. Pápai, *J. Catal.* **2010**, *269*, 44
- [10] K. Tomishige, Y. Ikeda, T. Sakaihorii, K. Fujimoto, *J. Catal.* **2000**, *192*, 355
- [11] D. C. Stoian, E. Taboada, J. Llorca, E. Molins, F. Medina, A. M. Segarra, *Chem. Commun.* **2013**, *49*, 5489
- [12] B. Fan, J. Zhang, R. Li, W. Fan, *Catal. Lett.* **2008**, *121*, 297
- [13] K. Tomishige, K. Kunimori, *Appl. Catal. A: Gen.* **2002**, *237*, 103
- [14] K. T. Jung, A. T. Bell, *J. Catal.* **2001**, *204*, 339
- [15] H. J. Freund, M. W. Roberts, *Surf. Sci. Rep.* **1996**, *25*, 225
- [16] S.M. Maier, A. Jentys, J.A. Lercher, *J. Phys. Chem. C*, **2011**, *115*, 8005
- [17] W. Li, H. Huang, H. Li, W. Zhang, H. Liu, *Langmuir* **2008**, *24*, 8358

- [18] A. G. Evans, R. M. Connon, *Acta Metallurgica* **1986**, 34, 761
- [19] J. D. McCullough, K. N. Trueblood, *Acta Crystallographica* **1959**, 12, 507
- [20] G. Teufer, *Acta Crystallographica* **1962**, 15, 1187
- [21] R. D. Shannon, *Acta. Cryst.* **1976**, A32, 751
- [22] M. B. Gawande, P. S. Branco, K. Parghi, J. J. Shrikhande, R. K. Pandey, C. A. A. Ghumman, N. Bundaleski, O. M. N. D. Teodoro, R. V. Jayaram, *Catal. Sci. Technol.* **2011**, 1, 1653
- [23] H. Guan, J. Liang, Y. Zhu, B. Zhao, Y. Xie, *Acta. Phys. -Chim. Sin.* **2005**, 21, 1011
- [24] T. Yamaguchi, *Catal. Today* **1994**, 20, 199
- [25] E. P. Parry, *J. Catal.* **1963**, 2, 371
- [26] J. C. Lavalley, *Catal. Today* **1996**, 27, 377
- [27] G. Busca, *Catal. Today* **1996**, 27, 457
- [28] V. Eta, P. Mäki-Arvela, J. Wärnä, T. Salmi, J. Mikkola, D. Yu. Murzin, *Appl. Catal. A: Gen.* **2011**, 404, 39
- [29] B.A.V. Santos, C.S.M. Pereira, V.M.T.M. Silva, J.M. Loureiro, A.E. Rodrigues, *Appl. Catal. A: Gen.* **2013**, 455, 219
- [30] B.A.V. Santos, C.S.M. Pereira, V.M.T.M. Silva, J.M. Loureiro, A.E. Rodrigues, *Appl. Catal. A: Gen.* **2014**, 471, 106
- [31] Y. Ikeda, M. Asadullah, K. Fujimoto, K. Tomishige, *J. Phys. Chem. B* **2001**, 105, 10653
- [32] H. J. Hofmann, A. Brandner, P. Claus, *Chem. Eng. Technol.* **2012**, 35, 2140
- [33] L. Chen, S. Wang, J. Zhou, Y. Shen, Y. Zhao, X. Ma, *RSC Adv.* **2014**, 4, 30968
- [34] A. A. Tsyganenko, E. A. Trusov, *Russ. J. Phys. Chem.* **1985**, 59, 2602
- [35] M. Bensitel, V. Moravek, J. Lamotte, O. Saur, J. C. Lavalley, *Spectrochim. Acta* **1987**, 43A, 1487

2.7 Appendix

2.7.1 Raman spectroscopy of different ZrO₂-based catalysts

All the Raman spectroscopic measurements were performed with a Renishaw spectrometer (Series 1000). After calibration of the spectrometer using a Si (111) single crystal, Raman spectra were recorded with the use of green line of an argon-ion laser (514.53 nm, 2.41 eV). For *ex-situ* measurement, the activated samples were prepared over glass slits. Up to 10 accumulations between 100 and 4000 cm⁻¹ were recorded for obtaining high signal-to-noise-ratio spectra. Raman spectra of ZrO₂, Al₂O₃-ZrO₂ and MgO-ZrO₂ catalysts are shown Figure 2-19.

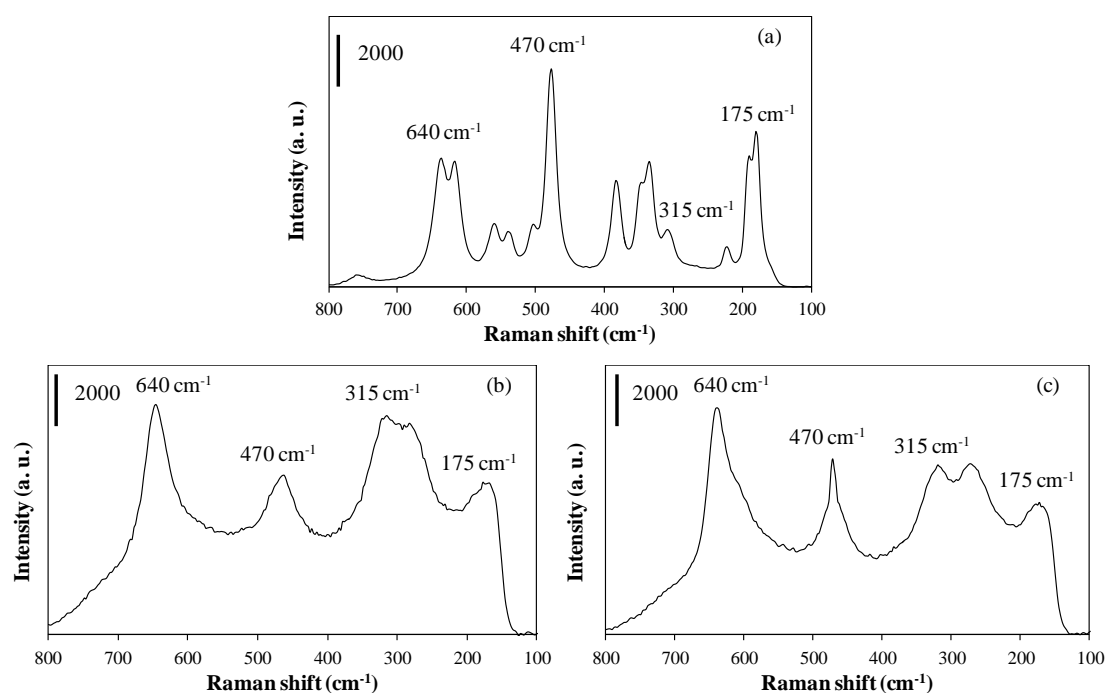


Figure 2-19 Raman spectra of different ZrO₂-based catalysts (a: ZrO₂, b: 6 % Al₂O₃-ZrO₂, c: 12 % MgO-ZrO₂)

The Raman spectrum of ZrO₂ synthesized via precipitation method showed both

characteristic bands of monoclinic and tetragonal phases. In contrast, $\text{Al}_2\text{O}_3\text{-ZrO}_2$ and MgO-ZrO_2 showed only characteristic bands of the tetragonal phase. For all measured ZrO_2 -based materials, the exclusive Raman band for cubic phase at 490 cm^{-1} was not observed, indicating that both $\text{Al}_2\text{O}_3\text{-ZrO}_2$ and MgO-ZrO_2 present only tetragonal phase. ^[1, 2]

2.7.2 N_2 physisorption of synthesized catalysts

The specific surface areas and pore volumes determined from the N_2 adsorption-desorption isotherms at $-196\text{ }^\circ\text{C}$ by using Brunauer-Emmett-Teller method are shown in Figure 2-20.

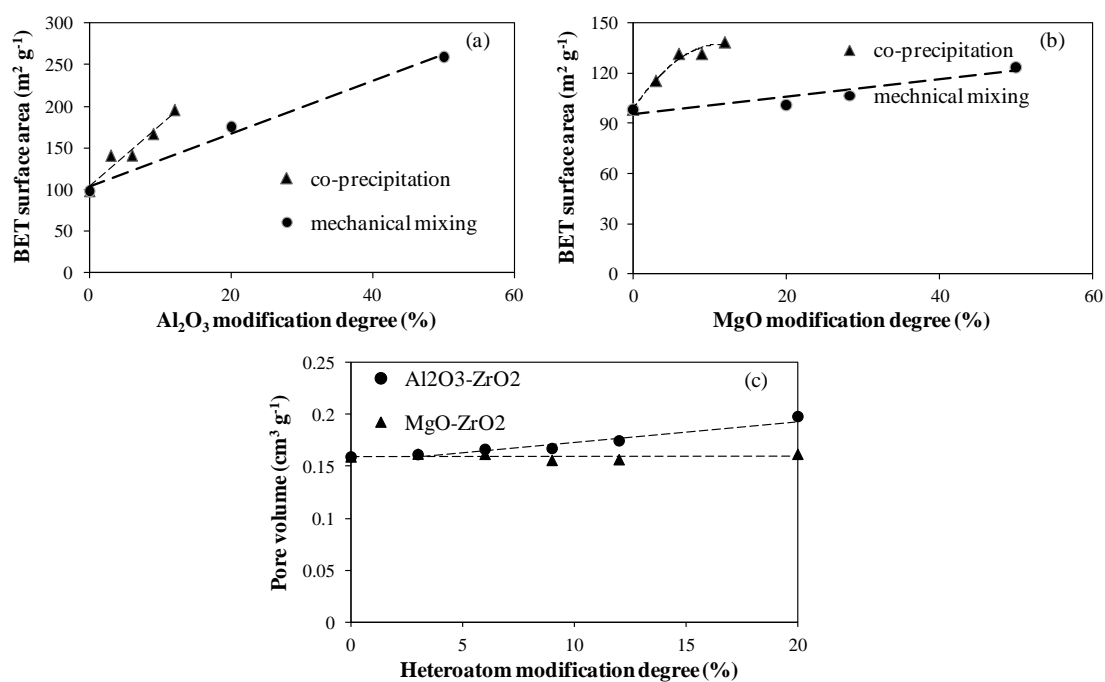


Figure 2-20 BET surface areas (a: $\text{Al}_2\text{O}_3\text{-ZrO}_2$, b: MgO-ZrO_2) and pore volumes (c) of synthesized ZrO_2 -based catalysts

Figure 2-20 (a) and (b) indicate that BET surface areas increase with increasing heteroatom doping in the range $0 \sim 12\%$ for both $\text{Al}_2\text{O}_3\text{-ZrO}_2$ and MgO-ZrO_2 .

Moreover, the linear correlation between heteroatom modification ratio and the extrapolated surface area for the simple mechanical mixture of $\text{Al}_2\text{O}_3 / \text{MgO}$ and ZrO_2 is similarly shown for comparison (dashed line in Figure 2-20 (a) and (b)). The surface area of the catalysts synthesized by co-precipitation method with a heteroatom fraction up to 12 % was obviously greater than that of the mechanical mixture of two oxides. The significant increase on the surface area of $\text{Al}_2\text{O}_3\text{-ZrO}_2$ catalysts shown in Figure 2-20 (c) implies the formation of amorphous deposits with high porosity. In contrast, no extra amorphous layer is formed in the case of MgO-ZrO_2 catalysts, and, therefore, no change on the pore volume is observed.

2.7.3 Representative XPS spectra of synthesized ZrO_2 -based catalysts

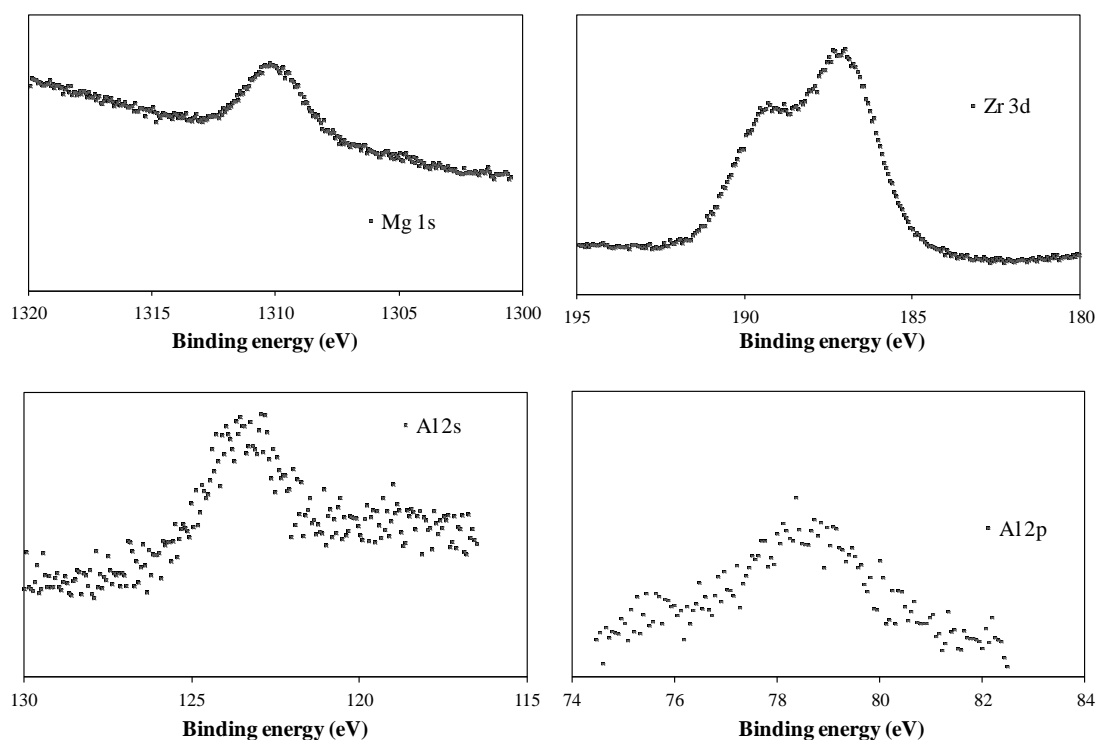


Figure 2-21 XPS spectra sample of ZrO_2 -based catalysts

2.7.4 LAS concentration on ZrO₂-based catalysts determined by IR spectra of adsorbed pyridine

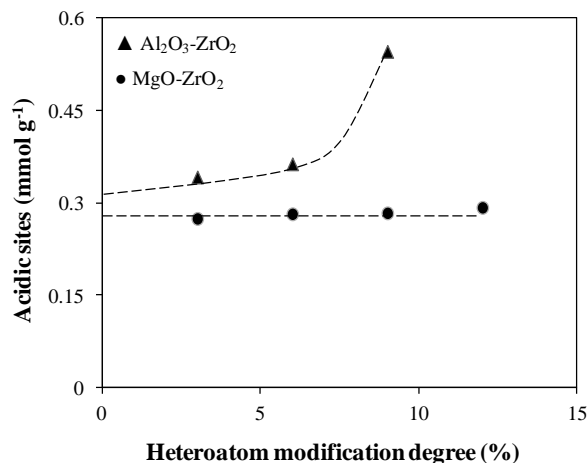


Figure 2-22 LAS concentration on ZrO₂-based catalysts determined by IR spectra of adsorbed pyridine

2.7.5 Determination of reaction orders on different ZrO₂-based catalysts

For the determination of the reaction order, the formula shown in Eq. 2-1 was used.

$$r = \frac{d[\text{DMC}]}{dt} = k [\text{MeOH}]^a [\text{CO}_2]^b$$

Eq. 2-1

Reaction orders of both reactants, *i.e.*, methanol and CO₂, were determined by using the double logarithmic plots of the initial rates of DMC formation *vs.* the starting concentrations of the respective reactant (Figure 2-23 and 2-24).

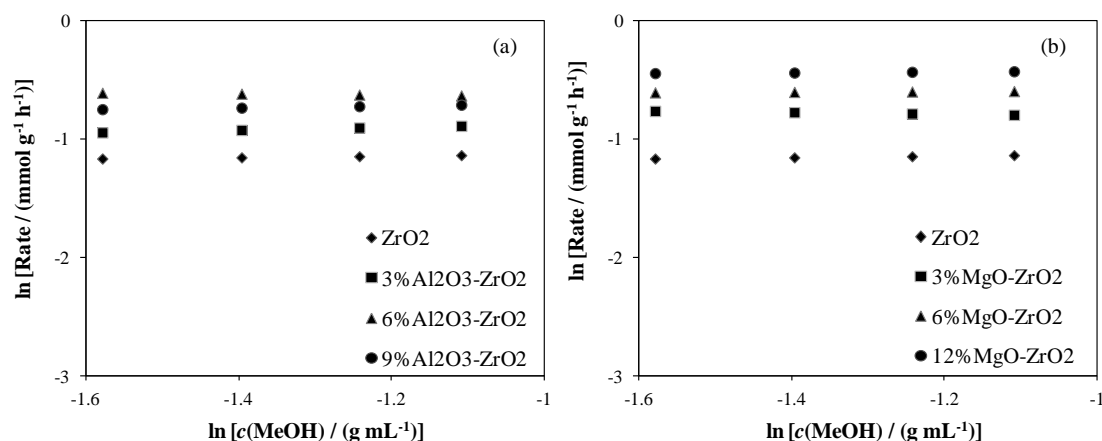


Figure 2-23 Determination of methanol reaction order on Al₂O₃-ZrO₂ (a) and MgO-ZrO₂ (b) catalysts (Reaction conditions: $T = 160$ °C, 10 g CO₂, methanol amounts vary from 25 g to 40 g.)

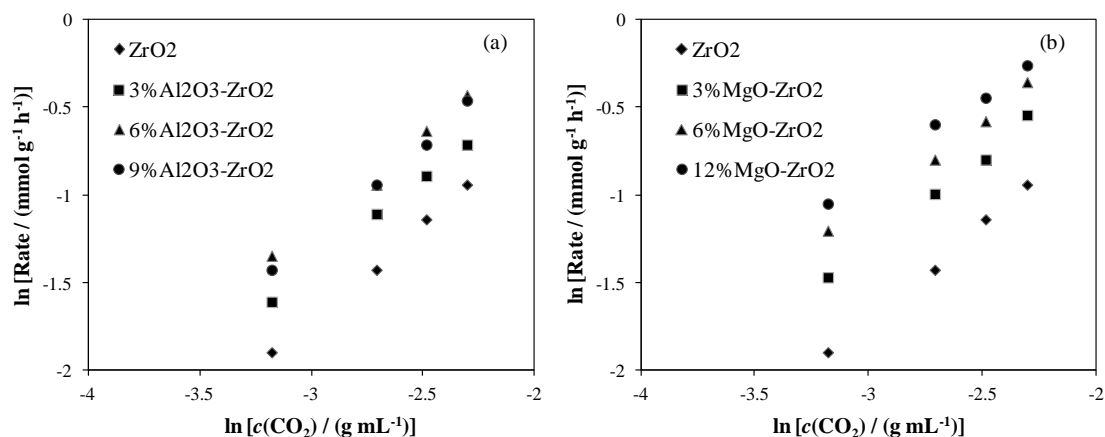


Figure 2-24 Determination of CO₂ reaction order on Al₂O₃-ZrO₂ (a) and MgO-ZrO₂ (b) catalysts (Reaction conditions: $T = 160$ °C, 39.6 g methanol, CO₂ amounts vary from 5 g to 12 g.)

2.7.6 Stability test for MgO-ZrO₂ catalyst under different conditions

To test the stability of the prepared catalysts under different reaction conditions, the catalytic reaction was performed using different approaches. In the stability test, 0.1 g fresh prepared MgO-ZrO₂ (12 % doping) catalyst was loaded in the autoclave and 39.6 g methanol were added. In the following step, the reactor was purged by N₂ (10 bar, 5 times) in order to avoid possible complications caused by the presence of

oxygen. As soon as the temperature of the reactor reached 160 °C, CO₂ was introduced by a syringe pump and the stirring was started. During the reaction, new portions of CO₂ were fed several times with the interval of 5 hours, leading to an overall increase of pressure. The measured rate of DMC formation was compared with the rate of the reaction where fresh catalysts were used (Figure 2-25). The pressure increase during repeated CO₂ addition is similarly shown in Figure 2-25. It is also worth mentioning that the catalyst amount was very small, the DMC yield was below 0.1 % and the overall catalytic reaction was conducted far away from the equilibrium level so that measured reaction rate was not affected by the thermodynamic constrains.

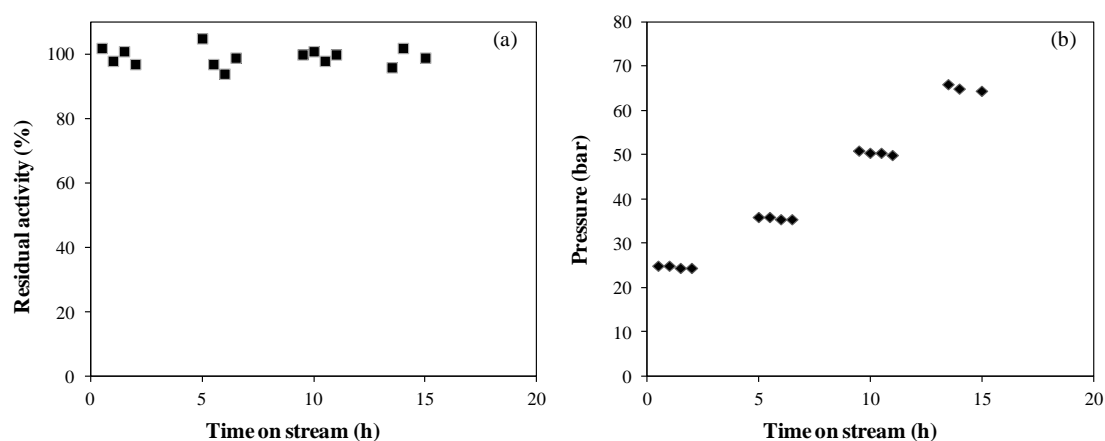


Figure 2-25 Stability test on MgO-ZrO₂ catalyst (a: Reaction rate is normalized by the rate obtained with the use of fresh catalyst under the same conditions. b: The pressure change during the stability test is accordingly presented.)

The stability tests clearly evidence that the catalytic activity of MgO-ZrO₂ is not depressed under various reaction conditions, demonstrating the excellent stability of the material.

2.7.7 Results of ICP-OES measurements

The results from ICP-OES measurements showed that Zr⁴⁺ concentration in liquid

phase was under the detection limit (10^{-6} weight fraction). The results support that DMC is formed in a direct heterogeneous catalyzed reaction of methanol and CO_2 .

2.7.8 Activity comparison of different ZrO_2 phases

To examine the effect of zirconia phase on the performance of ZrO_2 for DMC synthesis from methanol and CO_2 , mixed phase and pure phase ZrO_2 catalysts were synthesized.

Pure-phase monoclinic ZrO_2 was prepared by solvo-thermal method according to the procedure described in reference.^[3] For synthesis of pure monoclinic ZrO_2 , zirconyl nitrate and urea were dissolved into water, resulting 80 mL solution with concentration of zirconyl nitrate and urea of 0.4 and 4 mol L^{-1} , respectively. Then the prepared solution was sealed in a Teflon container with volume of 100 mL adapted inside a stainless steel autoclave and kept at 160 °C for 20 hours. During the solvo-thermal treatment, precipitate was formed under self-generated pressure and pH. After that, recovered precipitate was washed several times with deionized water, dried and calcined at 400 °C in synthetic air (1 °C min^{-1} ramp). Pure-phase tetragonal ZrO_2 was obtained in a methanol solution following the same procedure as described above. The isolated precipitate was washed with methanol and calcined at 400 °C in N_2 atmosphere (1 °C min^{-1} ramp).

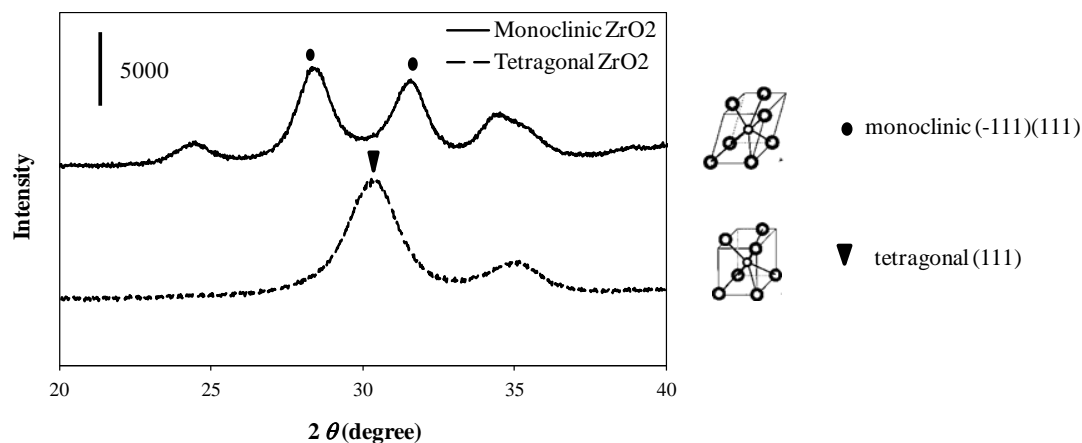


Figure 2-26 Powder XRD patterns of pure-phase ZrO_2

The formation of pure-phase ZrO_2 under synthesis conditions is evidenced by XRD patterns as shown in Figure 2-26. Their catalytic performance was tested with the procedure described in experimental section ($T = 160\text{ }^\circ\text{C}$, 39.6 g methanol, 10 g CO_2). The rate of DMC formation was determined as $0.09\text{ mmol g}_{\text{cat}}^{-1}\text{ h}^{-1}$ for monoclinic ZrO_2 and $0.40\text{ mmol g}_{\text{cat}}^{-1}\text{ h}^{-1}$ for tetragonal ZrO_2 . Since the acidic / basic properties of these two phases of ZrO_2 are quite similar,^[3] this difference in the observed catalytic activity is attributed to the better accessibility of the active sites located in tetragonal crystalline arrangement.

2.7.9 Characterization of surface Lewis acidic sites on ZrO_2 and MgO-ZrO_2 catalysts

For more detailed characterization of ZrO_2 -based catalysts' Lewis acidity, IR spectroscopy with adsorption of CO as a probe molecule was applied. CO is a weak basic molecule. Its interaction with either the Lewis acidic zirconium cation or hydroxyl group was investigated.^[4] In this chapter, the use of IR spectroscopy of CO adsorption is to further elucidate Lewis acidic site from methanol activation.

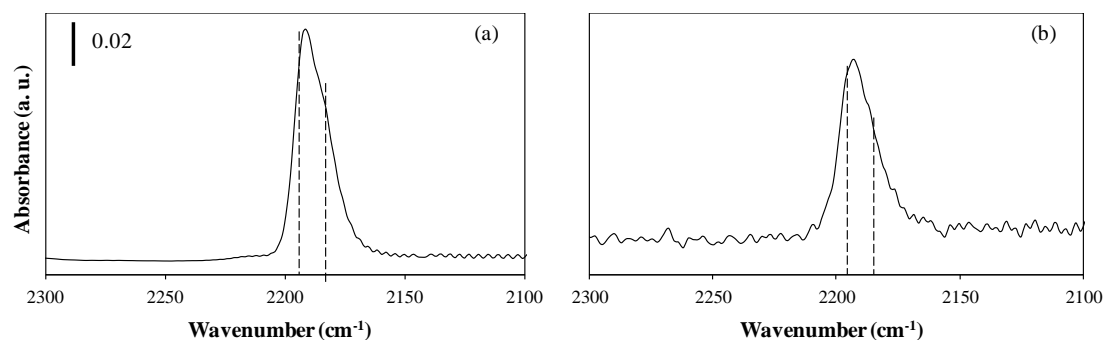
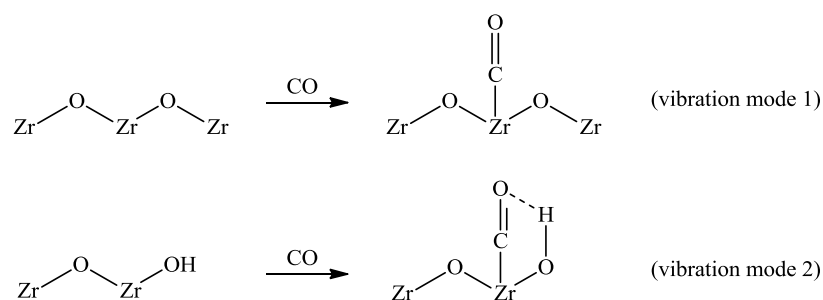


Figure 2-27 The IR spectroscopy of ZrO_2 (a) and MgO-ZrO_2 (b) catalysts with CO adsorption

In the IR spectra of different ZrO_2 -based catalysts with CO adsorption, the band at $\sim 2193 \text{ cm}^{-1}$ and another shoulder band at lower wavenumber ($\sim 2180 \text{ cm}^{-1}$) were observed (Figure 2-27). The band at $\sim 2193 \text{ cm}^{-1}$ is the finger print of coordinatively unsaturated Zr^{4+} (Lewis acidic sites). Furthermore, the wavenumber of CO vibration bands indicates the strength of this Lewis acidity. MgO-ZrO_2 showed no difference compared with ZrO_2 ($\text{ZrO}_2 \sim 2193 \text{ cm}^{-1}$, $\text{MgO-ZrO}_2 \sim 2192 \text{ cm}^{-1}$). Therefore, the Lewis acidity of MgO-ZrO_2 is also entirely contributed by coordinatively unsaturated Zr^{4+} . In addition, the shoulder bands at lower wavenumbers indicate the existence of terminal hydroxyl groups which interacts with adsorbed CO, as shown in Scheme 2-11 (vibration mode 2).



Scheme 2-11 Two different CO vibration modes of CO adsorbed on coordinatively unsaturated Zr^{4+} (The wavenumbers of IR bands attributed to mode 1 and 2 are ~ 2193 and $\sim 2180 \text{ cm}^{-1}$, respectively.)

2.7.10 Change on surface hydroxyl group during methanol adsorption

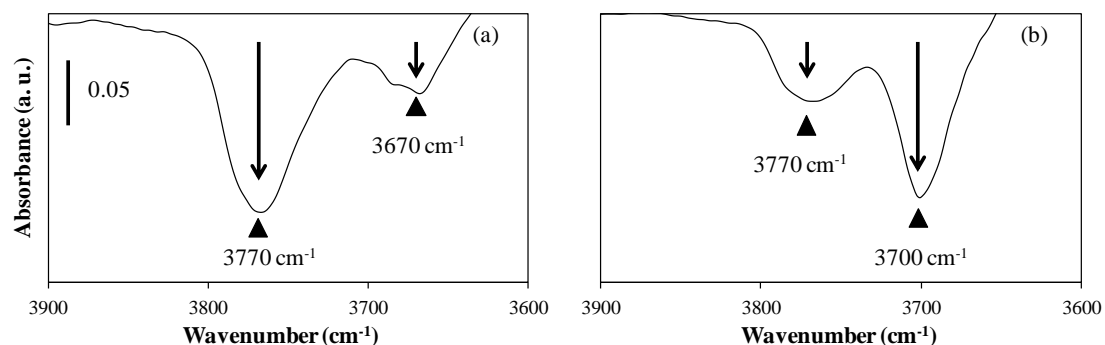


Figure 2-28 IR spectra of adsorbed methanol on ZrO_2 (a) and 12 % MgO-ZrO_2 (b) (Presented spectra are the results of subtracting the spectra following methanol adsorption from the spectra before methanol addition, ▲: surface hydroxyl group.)

IR spectra during methanol adsorption in the range of $3900 \text{ cm}^{-1} \sim 3600 \text{ cm}^{-1}$ are shown in Figure 2-28. The consumption of surface hydroxyl groups is evidenced by the inverted characteristic bands in this range.

2.7.11 Experimental evidence of water formation during MMC formation

In IR spectroscopy, the signal of O-H stretching vibration in the range of $3000 \sim 3500 \text{ cm}^{-1}$ is used for the characterization of water formed during surface reactions. However, in this spectral region, the contribution of the hydroxyl groups needs to be similarly considered. Therefore, methanol was solely introduced into the IR cell to enable the interaction with ZrO_2 catalyst. The same amount of catalyst was interacted with CO_2 followed by methanol addition, in order to mimic the formation of surface MMC. The results of these two measurements are shown in Figure 2-29.

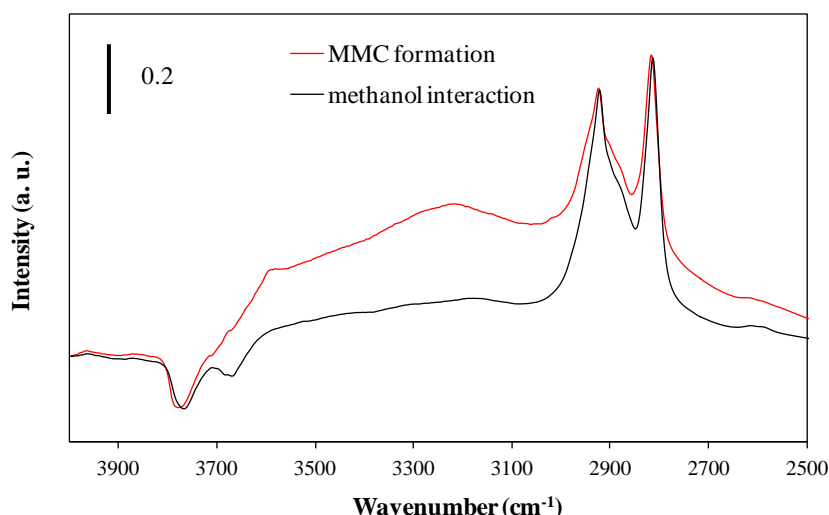


Figure 2-29 Comparison on water formation between methanol interaction and MMC formation on ZrO_2 catalyst (Red: IR spectrum of methanol addition to a CO_2 -saturated surface of ZrO_2 . Black: IR spectrum of methanol addition to activated ZrO_2 followed by desorption. All spectra were recorded at $160\text{ }^\circ\text{C}$.)

Since the amount of catalyst for the two measurements was identical, it is not surprising that the intensities of the bands at 3775 cm^{-1} (surface hydroxyl group), 2925 and 2825 cm^{-1} (surface methanol-induced species) were close to each other. In contrast, in the range of $3000 \sim 3500\text{ cm}^{-1}$, two recorded spectra showed a huge difference on intensity. The intensity of IR line recorded after MMC formation is almost as high as twice the intensity of the methanol induced species. The explanation for this observation is the additional water formed during MMC formation. Noteworthy, the different IR band intensities of C-H stretching in the range of $2700 \sim 3000\text{ cm}^{-1}$ on different spectra are due to different molar extinction factors of different surface species, based on the results of previously performed calibration.

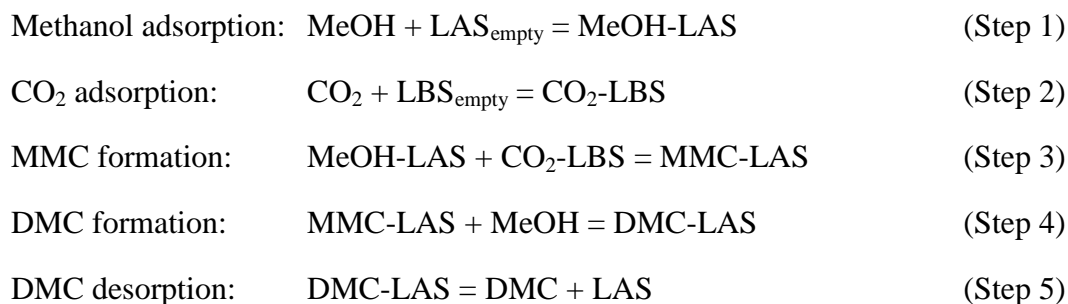
2.7.12 Rate expression derivation of different elementary steps

In order to establish the correlation between surface properties and observed catalytic activity, the overall assumption was made as that all tested ZrO_2 -based catalysts have to be operated under the same kinetic regime, *i.e.*, the same surface reactions are

taking place with comparable rates in the assumed reaction sequence. The rationality of the above assumptions is based on the similarity of measured kinetic parameters and detected surface species. It is further assumed that all methanol-involved intermediates are accommodated on surface Lewis acidic sites. CO₂ adsorption is, however, opposite to methanol, enabled on the surface basic sites and is relatively weak. Therefore, it can be assumed that the surface coverage of methanol is considerably higher compared to that of CO₂.

In order to identify the rate determining step, a steady state assumption was made. In this respect, we assumed that the overall rate of DMC formation is identical with the rate of the slowest reaction step (rate determining step). For an accurate analysis, the rate each step was presented compared with the experimental determined rate expression.

In the overall catalytic transformation, following 5 elemental steps were considered.



The rate of step 1 can be expressed as Eq. 2-2.

$$r_1 = k_1 [\text{MeOH}] [\text{LAS}_{\text{empty}}]$$

Eq. 2-2

Here $[\text{LAS}_{\text{empty}}]$ represents the concentration of unoccupied Lewis acidic site specific for methanol adsorption.

Based on the Langmuir's model, the concentration of unoccupied Lewis acidic site can be formulated as Eq. 2-3.

$$[\text{LAS}_{\text{empty}}] = (1 + K_1 [\text{MeOH}])^{-1}$$

Eq. 2-3

Therefore, the rate of methanol adsorption will become r_1 in Eq. 2-4.

$$r_1 = k_1 [\text{MeOH}] (1 + K_1 [\text{MeOH}])^{-1}$$

Eq. 2-4

Based on the investigation of *in-situ* IR measurements, the methanol coverage is high ($K_1 [\text{MeOH}] \gg 1$, Figure 2-9). Therefore, r_1 reduces to a constant $k_1 K_1^{-1}$, independent by the concentration of methanol and CO_2 in the mixture. Under the circumstances, this would imply an observed reaction order of 0 for both reactants (methanol and CO_2), being in contradiction with current experimental results (Table 2-3). Therefore, step 1 methanol adsorption is not RDS.

The rate of step 2 can be formulated as shown in Eq. 2-5.

$$r_2 = k_2 [\text{CO}_2] [\text{LBS}_{\text{empty}}]$$

Eq. 2-5

Here [LBS] represents the concentration of unoccupied Lewis basic site specific for CO_2 adsorption.

Based on the Langmuir's model, the concentration of unoccupied Lewis basic site can be calculated as Eq. 2-6.

$$[\text{LBS}_{\text{empty}}] = (1 + K_2 [\text{CO}_2])^{-1}$$

Eq. 2-6

Therefore, the rate of CO₂ adsorption will become r_2 in Eq. 2-7.

$$r_2 = k_2 [\text{CO}_2] (1 + K_2 [\text{CO}_2])^{-1}$$

Eq. 2-7

Based on the investigation of *in-situ* IR measurements that CO₂ is low ($K_2 [\text{CO}_2] \ll 1$, Figure 2-10). Therefore, r_2 reduces to $k_2 [\text{CO}_2]$. In this case, it can be assumed a zero order for methanol and a first order for CO₂. This form is in agreement with the experimentally determined rate expression, so that step 2 is considered as a possible RDS, limiting the overall DMC formation.

The rate of step 3 is shown in Eq. 2-8.

$$r_3 = k_3 [\text{LAS} - \text{MeOH}] [\text{LBS} - \text{CO}_2]$$

Eq. 2-8

Here LAS-MeOH and LBS-CO₂ represent the active sites where methanol and CO₂ were adsorbed, respectively.

Based on the Langmuir's model, the concentration of Lewis acidic site occupied by methanol and the concentration of Lewis basic site occupied by CO₂ can be calculated

as Eq. 2-9.

$$\begin{aligned} [\text{LAS} - \text{MeOH}] &= K_1 [\text{MeOH}] (1 + K_1 [\text{MeOH}])^{-1} \\ [\text{LBS} - \text{CO}_2] &= K_2 [\text{CO}_2] (1 + K_2 [\text{CO}_2])^{-1} \end{aligned}$$

Eq. 2-9

Under the above assumptions of high surface coverage on LAS ($K_1 [\text{MeOH}] \gg 1$, Figure 2-9), $[\text{LAS}-\text{MeOH}]$ will become equal to 1. In contrast, low coverage on LBS ($K_2 [\text{CO}_2] \ll 1$, Figure 2-10) leads to that $[\text{LBS}-\text{CO}_2]$ will reduce to $K_2 [\text{CO}_2]$. Under this condition, the rate of step 3 reduces to $k_3 K_2 [\text{CO}_2]$, implying a zero order for methanol and a first order for CO_2 , in good agreement with experimentally determined reaction orders. Thus, step 3 is similarly considered as a possible RDS, limiting overall DMC formation.

The rate of step 4 can be presented as Eq. 2-10.

$$r_4 = k_4 [\text{LAS} - \text{MMC}] [\text{MeOH}]$$

Eq. 2-10

Here LAS-MMC represents Lewis acidic sites where MMC is formed.

The concentration of LAS occupied by MMC is proportional to the concentration of LAS-MeOH and LBS- CO_2 . Therefore, the rate expression will become r_4 in Eq. 2-11.

$$r_4 = k_4 K_3 [\text{LAS} - \text{MeOH}] [\text{LBS} - \text{CO}_2] [\text{MeOH}]$$

Eq. 2-11

Under the conditions of high coverage of methanol on LAS and low coverage of CO_2

on LBS (Figure 2-9 and 2-10), [LAS-MeOH] reduces to 1 while and [LBS-CO₂] reduces to K_2 [CO₂], so that Eq. 2-11 further reduces to r_4 in Eq. 2-12.

$$r_4 = k_4 K_2 K_3 [\text{MeOH}] [\text{CO}_2]$$

Eq. 2-12

As shown in Eq. 2-12, the rate expression of step 4 would imply a first order for both reactants. This is in contradiction with experimentally determined reaction orders. Therefore, step 4 is not considered as the RDS.

The rate of the last step (step 5) is r_5 in Eq. 2-13.

$$r_5 = k_5 [\text{LAS} - \text{DMC}]$$

Eq. 2-13

Here LAS-DMC represents DMC adsorbed on Lewis acidic sites.

The concentration of DMC adsorbed on Lewis acidic sites is proportional to the concentration of MMC adsorbed on Lewis acidic sites and of methanol (derived from step 4).

$$\begin{aligned} [\text{LAS} - \text{MeOH}] &= K_3 K_4 [\text{LAS} - \text{MeOH}] [\text{LBS} - \text{CO}_2] [\text{MeOH}] \\ &= K_2 K_3 K_4 [\text{MeOH}] [\text{CO}_2] \end{aligned}$$

Eq. 2-14

The rate expression for step 5 becomes Eq. 2-15.

$$r_5 = k_5 K_2 K_3 K_4 [\text{MeOH}] [\text{CO}_2]$$

Eq. 2-15

In this formulation, both reactants have a first order correlation to the rate of step 5, in contradiction with experimentally determined rate expression. Therefore, step 5 is not considered as the RDS.

A general overview of the estimated reaction orders are shown in Table 2-4.

Table 2-4 Estimated reaction orders in different elementary steps

Elementary step	Methanol order	CO ₂ order
Methanol adsorption	0	0
CO ₂ adsorption	0	1
MMC formation	0	1
DMC formation	1	1
DMC desorption	1	1

Compared to experimental results, the rate determining step is concluded to involve CO₂ adsorption and / or surface reaction (MMC formation). From kinetic parameters, among steps of CO₂ adsorption and surface reaction, it is difficult to distinguish which of these two reactions presents a higher limitation to the DMC formation.

In previous contributions, it was proposed that the CO₂ insertion into the surface methoxide species leads to MMC formation and is one single rate determining step,^[5] or it is considered that CO₂ competitively adsorbed with methanol and the consecutive surface reaction is the rate determining step.^[6, 7]

Concerning the CO₂ adsorption (step 2 in the proposed model, Eq. 2-5), as CO₂ is rather an acidic molecule and a more basic MgO-ZrO₂ would have a higher affinity to

CO₂, an acceleration of the reaction (higher k_2) is expected as compared to a ZrO₂ catalyzed reaction. Since CO₂ coverage is rather low, the concentration of empty LBS nearly equals to the concentration of total LBS. In the case of MgO modified material, an increase of the sites are observed (Figure 2-7). These two factors have an impact on the overall reaction rate under the assumption that CO₂ adsorption is the rate determining step. In addition, the slight depression of CO₂ reaction order with increasing MgO modification degrees can be explained by larger CO₂ coverage caused by stronger basic sites.

Concerning the step of MMC formation (step 3), as shown in Eq. 2-8, the concentration of methanol occupied LAS is the same for ZrO₂ as well as for MgO-ZrO₂ catalysts. Concerning the CO₂ adsorption, compared to ZrO₂ catalyst, MgO-ZrO₂ has larger fraction and stronger basic sites, so that [LBS-CO₂] becomes larger for MgO-ZrO₂. The surface reaction is driven by the nucleophilic attack from an oxygen atom of methoxide species on a carbon atom of adsorbed CO₂. As evidenced by NH₃-TPD measurements, Lewis acidity of ZrO₂-based catalysts is weakened by MgO doping, so that the coordinatively unsaturated electropositive metal has less affinity for the electrons of a nucleophilic oxygen atom in methoxide species and the surface reorganization becomes favored. This effect indicates that the rate constant k_3 becomes larger. Therefore, the overall reaction rate is similarly enhanced.

Summarizing the observations made related to the two CO₂ involved reaction steps, it is argued that CO₂ adsorption and subsequent surface reactions have similar impacts on the overall reaction kinetics. Furthermore, MgO doping results in the generation of new and stronger Lewis basic sites on ZrO₂ catalyst surface, and has a positive effect on both steps. In the present study, the CO₂ coverage on MgO-ZrO₂ catalyst is predominantly higher, thus, cannot be neglected, since a slight depression of CO₂ reaction order has been observed by increasing the MgO content in the catalyst. This

observation further supports the LH mechanism in CO₂ involved surface reaction.

2.7.13 Calorimetric study on rate determining steps

Prior to the surface reaction, the catalyst surface is saturated by dimethyl ether (DME), in order to generate surface methoxide species and to avoid water formation. After removal of physisorbed species, CO₂ is contacted with DME-saturated catalyst. During this procedure, the CO₂ adsorption and formation of bicarbonate / carboxylate along with MMC occur simultaneously on the surface. The gained calorimetric results are the combined effects of these two elementary steps.

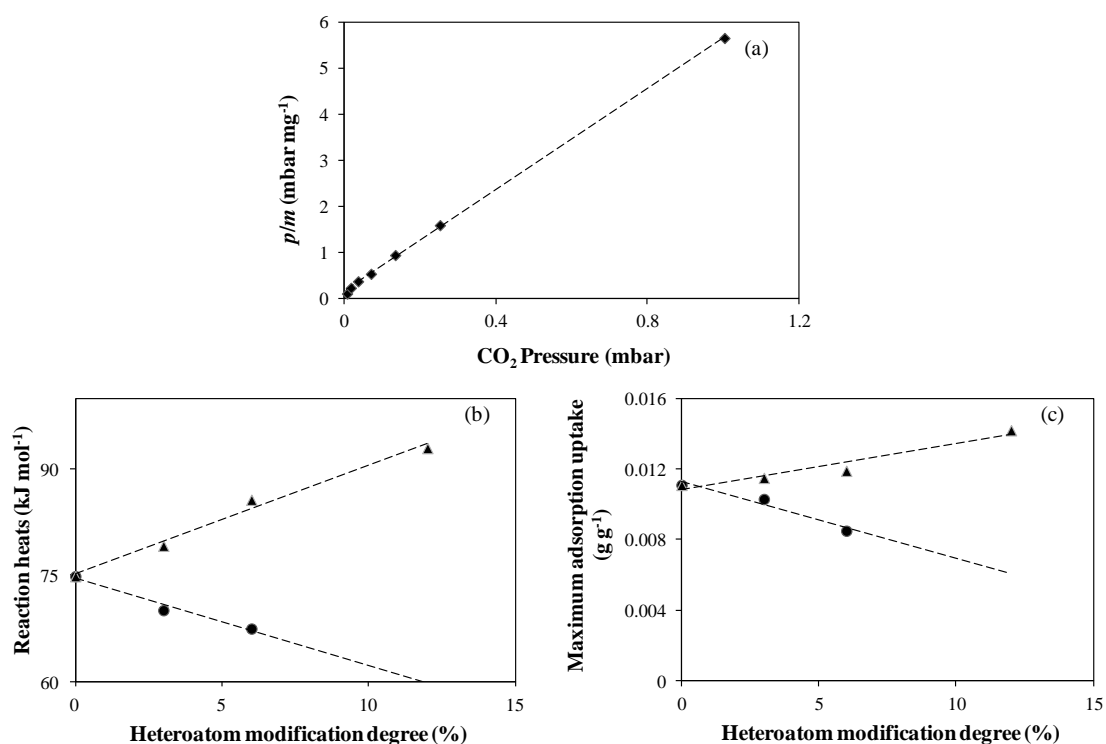


Figure 2-30 Example of fitted Langmuir isotherm (a), average reaction heats (b) and uptake of interaction (c) between CO₂ and DME-saturated surfaces on different ZrO₂-based catalysts (▲: MgO-ZrO₂, ●: Al₂O₃-ZrO₂)

The surface interactions follow Langmuir's model on all measured catalysts. One example of fitted results by Langmuir's isotherm is shown in Figure 2-30 (a). The

comparison of average reaction heat for this surface interaction as well as the CO₂ uptake capacity on DMC saturated surface over different catalysts are shown in Figure 2-30 (b) and (c). The experimental observations clearly demonstrates that the reaction heat increases with MgO doping while decreases with Al₂O₃ doping. In addition, the DME saturated surface of MgO-ZrO₂ has larger CO₂ capacity than ZrO₂ catalyst. These phenomena suggest that the rate determining steps are more favored on MgO-ZrO₂, which is in agreement with kinetic and spectroscopic investigations.

2.7.14 References in Section 2.7

- [1] C. M. Phillippi, K. S. Mazdidasni, *J. Am. Ceram. Soc.* **1971**, *54*, 254
- [2] R. Srinivasan, M. B. Harris, R. J. De Angelis, B. H. Davis, *J. Mater. Res.* **1988**, *3*, 787
- [3] W. Li, H. Huang, H. Li, W. Zhang, H. Liu, *Langmuir* **2008**, *24*, 8358
- [4] K. T. Jung, A. T. Bell, *J. Mol. Catal. A: Chem.* **2000**, *163*, 27
- [5] V. Eta, P. Mäki-Arvela, J. Wärnå, T. Salmi, J. Mikkola, D. Yu. Murzin, *Appl. Catal. A: Gen.* **2011**, *404*, 39
- [6] B.A.V. Santos, C.S.M. Pereira, V.M.T.M. Silva, J.M. Loureiro, A.E. Rodrigues, *Appl. Catal. A: Gen.* **2013**, *455*, 219
- [7] B.A.V. Santos, C.S.M. Pereira, V.M.T.M. Silva, J.M. Loureiro, A.E. Rodrigues, *Appl. Catal. A: Gen.* **2014**, *471*, 106

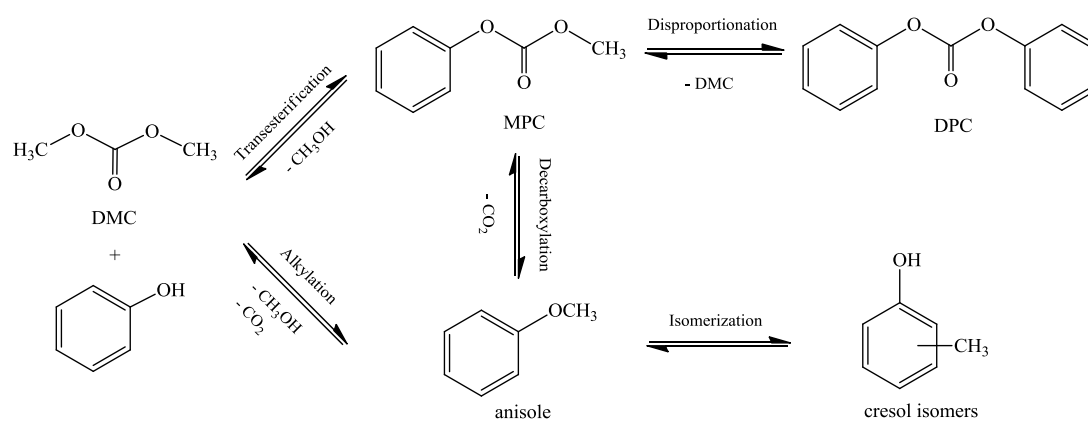
Chapter 3

Mechanism of MoO₃ catalyzed transesterification of DMC with phenol: evidence for highly active nanocrystalline phase for selective DPC formation

Nanocrystalline MoO₃ clusters on porous SiO₂ exhibit the highest catalytic activity and the best chemoselectivity for transesterification of DMC with phenol. For transesterification, the catalyst yields a TOF of 51 h⁻¹ and a chemoselectivity to methyl phenyl carbonate of > 99 %. The superior catalytic performance is attributed to a cooperative effect between the highly dispersed nanocrystalline MoO₃ clusters for DMC activation and unique surface properties of MoO₃-SiO₂ with a high concentration of Mo-O-Mo sites on the catalyst surface. The high chemoselectivity is mainly governed by the high dispersion of the mild Lewis acidic and basic sites of nanocrystalline MoO₃ on the support responsible for the preferential adsorption and activation of DMC via carbonyl group. Reactivity data confirm the competitive adsorption of DMC and phenol, leading to the formation of an asymmetrical carbonate species as key intermediate in the transesterification reaction.

3.1 Introduction

With the increasing concern about the energy and environmental issues originating from current chemical processes, the development of sustainable and green chemical processes for the synthesis of polycarbonates is highly required. Polycarbonates (PCs) are, due to their unique physicochemical properties, widely employed as an engineering plastic in various applications, such as electronic appliances, optical lens and medical equipment. PCs can be produced via transesterification of bisphenol-A with diphenyl carbonate (DPC), without the use of toxic and corrosive reagent phosgene. In order to go beyond “traditional” chemical engineering, scientists are continuously working on novel concepts and techniques that potentially could transform the DPC synthesis into an environment-friendly sustainable phosgene-free process. ^[1 - 4] In this respect, DPC was synthesized via a two-step reaction starting from phenol and dimethyl carbonate (DMC). Transesterification of DMC with phenol primarily leads to the formation of methyl phenyl carbonate (MPC), a key intermediate in the DPC process. The further activation of MPC on Lewis acidic sites (LAS) facilitates the following disproportionation reaction and leads to the selective formation of DPC. Brønsted acidic sites (BAS) and strong LAS catalyze alkylation, while surface basic sites favor decarboxylation reactions, overall enabling the formation of anisole and cresol isomers. ^[5] The proposed reaction network that could count for all the assumed products and by-products is depicted in Scheme 3-1.



Scheme 3-1 Schematic representation of the reaction network that count for DPC and anisole formation on competitive pathways

The main pathway of DPC synthesis (the 1st step transesterification to MPC followed by the 2nd step disproportionation to DPC in Scheme 3-1) is an equilibrium constrained reaction (equilibrium constant $K < 10^{-5}$ at a temperature range of 160 ~ 180 °C). From thermodynamic point of view, the presence of methanol, as the co-product in the reaction mixture (Scheme 3-1), limits the overall yield of MPC and DPC. In order to overcome this limitation, the methanol content in the reaction mixture needs to be continuously reduced. Compared to the disproportionation of MPC, the reaction between phenol and DMC is more critical, owing to its lower equilibrium constant ($K < 10^{-3}$ for the 1st step transesterification while $K \sim 0.1$ for disproportionation of MPC).^[6] From kinetic point of view, both reaction steps are enabled on surface LAS, although the operational conditions which favor the two reactions might differ from each other due to thermodynamic concerns.^[5, 7] Therefore, studies on the critical parameters influencing the first transesterification step are mandatory for understanding the catalysis.

The transesterification of DMC with phenol can be enabled by either homogeneous or heterogeneous Lewis acid catalysts. In this respect, several remarkable homogeneous Lewis acid catalysts were reported for their high activity and selectivity.^[8-11] Among all homogeneous catalysts, (C₄H₉)₂SnO is the most representative one, due to its excellent catalytic performance and stability.^[12, 13] In parallel with the development of

homogeneous catalysts, various heterogeneous catalytic materials like $\text{MoO}_3/\text{SiO}_2$,^[7] $\text{TiO}_2/\text{SiO}_2$,^[5, 14] $\text{V}_2\text{O}_5/\text{SiO}_2$,^[15] PbO/MgO ^[16] and CeO_2 -based mixed oxides^[17] were also reported for the transesterification of DMC with phenol. Based on the outcome of scientific research, it is known that transition metal oxides with mild surface acidic / basic sites are suitable candidates of heterogeneous catalysts for the transesterification of DMC with phenol. Strong BAS or LAS favorably catalyze the alkylation reaction between phenol and DMC, while strong basic sites accelerate the decarboxylation of MPC (Scheme 3-1). Both alkylation and decarboxylation pathways lead to the formation of the main by-product anisole and its isomers on a thermodynamically favored pathway. However, in-depth kinetic and mechanistic studies of heterogeneous catalysts for this reaction are not available yet. Due to the mild acidic and basic properties of the active sites of MoO_3 , MoO_3 supported on SiO_2 was reported as suitable transesterification catalyst presenting high activity and selectivity.^[7] Therefore, it is important to investigate the catalytic transesterification at molecular level, in order to understand fundamental activation processes and to design a new energy-efficient catalytic process.

In this chapter, MoO_3 was prepared by using various supports with different surface acidic / basic properties and tested for the transesterification reaction of DMC with phenol. By correlating the structural analysis data and the catalytic performance, it was shown that the high concentration and high dispersion of Mo-O-Mo sites in nanocrystalline $\alpha\text{-MoO}_3$ clusters are stabilized on the SiO_2 support, contributing to the favored adsorption and activation of DMC via carbonyl group. Based on detailed kinetic results and *in-situ* spectroscopic measurements, it was possible to identify main reaction steps that would count for the DPC formation. The reaction involves the competitive adsorption of both reactants (phenol and DMC) on Lewis acidic sites, resulting in the formation of an asymmetrical carbonate species, the key intermediate in DPC formation.

3.2 Experimental

3.2.1 Catalysts preparation

3.2.1.1 Preparation of MoO_3 -based catalysts on different supports

MoO_3 catalysts deposited on oxide supports with various structural and chemical properties, *i.e.*, Al_2O_3 , CaO , ZrO_2 and SiO_2 , were prepared by wet impregnation method. For synthesizing supported MoO_3 materials (20 wt. %), 1.23 g of $(\text{NH}_4)_6\text{Mo}_7\text{O}_{24} \cdot 7 \text{H}_2\text{O}$ were dissolved in 50 mL water (pH = 7.5 at 25 °C). Afterwards, 4 g of support were added to the aqueous solution under continuous stirring. The resulted blue suspension was then stirred for 4 hours at 80 °C till a homogeneous gel was formed. Finally, the obtained gel was dried at 120 °C overnight and calcined for 6 hours at 500 °C in air. For comparison, non-supported MoO_3 catalyst was also prepared by pyrolysis of $(\text{NH}_4)_6\text{Mo}_7\text{O}_{24} \cdot 7 \text{H}_2\text{O}$ for 6 hours at 500 °C.

3.2.1.2 Preparation of $\text{MoO}_3/\text{SiO}_2$ catalysts with different MoO_3 loadings

Following the synthetic approach described in Section 3.2.1.1, a series of MoO_3 - SiO_2 catalysts with loadings of 1 ~ 20 wt. % were prepared by using various amounts of $(\text{NH}_4)_6\text{Mo}_7\text{O}_{24} \cdot 7 \text{H}_2\text{O}$ and SiO_2 .

3.2.1.3 Preparation of 20 wt. % $\text{MoO}_3/\text{SiO}_2$ catalysts at different calcination temperatures

Following the synthetic approach described in Section 3.2.1.1 and 3.2.1.2, 5 portions

of homogeneous (in sum *ca.* 50 g) gel mixture of $(\text{NH}_4)_6\text{Mo}_7\text{O}_{24} \cdot 7 \text{H}_2\text{O}$ and SiO_2 were prepared. After drying the gel mixture, the 5 aliquots were calcined in air for 6 hours at 300, 400, 450, 500 and 600 °C, respectively.

3.2.2 Catalytic reaction

The transesterification reaction of DMC with phenol was carried out in a stainless steel autoclave (Parr instrument) with an inner volume of 300 mL. In a standard catalytic reaction, 0.1 g MoO_3 -based catalyst (synthesized with different supports, different loadings and at different calcination temperatures), 11.4 g phenol and 109 g DMC (substrate / catalyst = 1200 in weight) were suspended in the autoclave at ambient temperature. The autoclave was then sealed and purged with N_2 for several times before heating. After the reaction temperature was reached (160 °C, monitored by the reactor controller Parr 4848), rigorous stirring (700 rpm) was started. For product analysis, aliquots of filtered samples were taken at short time intervals (5 ~ 20 min). The composition of the reaction mixture was determined by GC (Shimadzu GC 2010 plus) equipped with a capillary column (Optima 35 MS). For analysis, the column temperature was set to 90 °C and the samples were measured by using a temperature ramp of 15 °C min^{-1} .

For a better understanding on the complex reaction network, the MoO_3 -catalyzed transesterification was similarly performed by using different fractions of phenol and DMC at identical substrate to catalyst ratio.

3.2.3 Catalyst characterization

In order to determine the BET specific surface area of synthesized MoO_3 -based catalysts, N_2 adsorption-desorption measurements were performed with a Sorptomatic

1990 Series instrument. In all the cases, the samples were activated in vacuum at 300 °C for 2 hours before measurements. The adsorption-desorption processes were conducted at -196 °C.

The crystal structure of synthesized materials was analyzed by X-ray diffraction measurements. Philips X'Pert Pro diffractometer equipped with an X'celerator module using Cu-K α radiation operating at 40 kV / 45 mA was applied. The samples were measured with a scan rate of 3 ° min⁻¹ from 5 ° to 70 ° (2 θ).

Raman analysis was performed with a Renishaw spectrometer (Series 1000). After calibration of the spectrometer using a Si (111) single crystal, all the Raman spectra were recorded by using the green line of an argon-ion laser (514.53 nm, 2.41 eV). For *ex-situ* measurement, the activated samples were prepared over glass slits. 1 ~ 10 accumulations of Raman shift between 100 and 4000 cm⁻¹ were recorded for obtaining high signal-to-noise ratio. *In-situ* Raman spectra were recorded from materials placed between quartz wool in a quartz reactor with an inner-diameter of 1.62 mm by using the same parameters as described above. In order to remove the pre-adsorbed small molecules from the sample, the materials were activated under inert conditions (N₂ atmosphere) for 1 hour at 150 °C. During the *in-situ* measurement, vapors of the liquid adsorbates (*e.g.*, DMC) were introduced into the reactor by using N₂ as a carrier gas.

IR spectroscopy of adsorbed pyridine was used to determine the concentration of Brønsted and Lewis acidic sites (BAS and LAS). The samples were pressed into a thin self-supporting wafer and activated for 1 hour at 450 °C in vacuum. Prior to pyridine adsorption, the background spectrum was recorded by an IR spectrometer (Perkin-Elmer 2000) with resolution of 2 cm⁻¹. Subsequently, the activated samples were exposed to pyridine vapors at pressure of 0.1 mbar for *ca.* 1 hour at 150 °C.

After evacuation for 0.5 hour to remove physisorbed pyridine, another spectrum was recorded. The bands at *ca.* 1540 cm⁻¹ and 1450 cm⁻¹ were used for characterization of BAS and LAS, respectively. After that, the adsorbed pyridine was desorbed by evacuation at elevated temperature (450 °C), in order to evaluate the strength of surface acidic sites.

In order to study the surface chemistry and to identify intermediates involved in the various elemental steps, *in-situ* vacuum IR spectroscopic measurements (Bruker ISF88) were performed. Prior to measure, all the samples were pressed into thin self-supporting wafers and activated under vacuum ($p = 10^{-6}$ mbar) for 1 hour at 450 °C. DMC and MPC were used as adsorbates for the identification of *in-situ* formed intermediates on the catalyst surface. The temperature-dependent IR measurements, in this study, were performed under *quasi-steady* state conditions. Based on experimental data, a temperature ramp of 1 °C min⁻¹ was determined as suitable for the present catalytic system. In a typical temperature-dependent IR measurement, the catalyst was first treated with the respective adsorbate(s). The system evacuation was initiated as soon as the expected intermediate was formed. IR spectra of treated catalyst were continuously recorded at short time intervals (5 min) till the steady state conditions were reached. The heating program was then started with a ramp of 1 °C min⁻¹ under evacuation ($p < 10^{-5}$ mbar).

3.3 Results

3.3.1 Physico-chemical properties of MoO₃ catalysts

In an initial effort to establish the correlation between catalytic performance and active catalyst surface, all the synthesized MoO₃/SiO₂ materials were analyzed by

using spectroscopic characterization techniques including N₂ physisorption (BET), powder X-ray diffraction (XRD), Raman and infrared (IR) spectroscopy.

For MoO₃ catalysts supported on Al₂O₃, CaO, ZrO₂ and SiO₂, the BET surface area was in the range of 100 ~ 200 m² g⁻¹, much larger than that of unsupported MoO₃ catalyst (*ca.* 5 m² g⁻¹), indicating that the support with high surface area provides a porous structure for accommodation of MoO₃ particles. It was revealed that 1 ~ 5 wt. % loading of MoO₃ on the SiO₂ support results in an obvious depression of surface area, while the specific surface area of MoO₃/SiO₂ catalysts with higher loadings (5 ~ 20 wt. %) was almost constant (~ 180 m² g⁻¹). Another significant depression of the BET surface area was observed at loading higher than 20 wt. % (Section 3.7, Figure 3-11 (a)). The total volume of macro- and mesopores almost kept constant in the range of 1 ~ 20 wt. % MoO₃ loadings (Section 3.7, Figure 3-11 (b)), while a depression of the micropores volume happened at loadings of 1 ~ 5 wt. %.

In order to analyze the stabilization of MoO₃ particles supported on SiO₂ in detail, information on crystallinity is required. In this respect, XRD measurements were performed on all prepared MoO₃/SiO₂ materials and typical XRD patterns are shown in Figure 3-1.

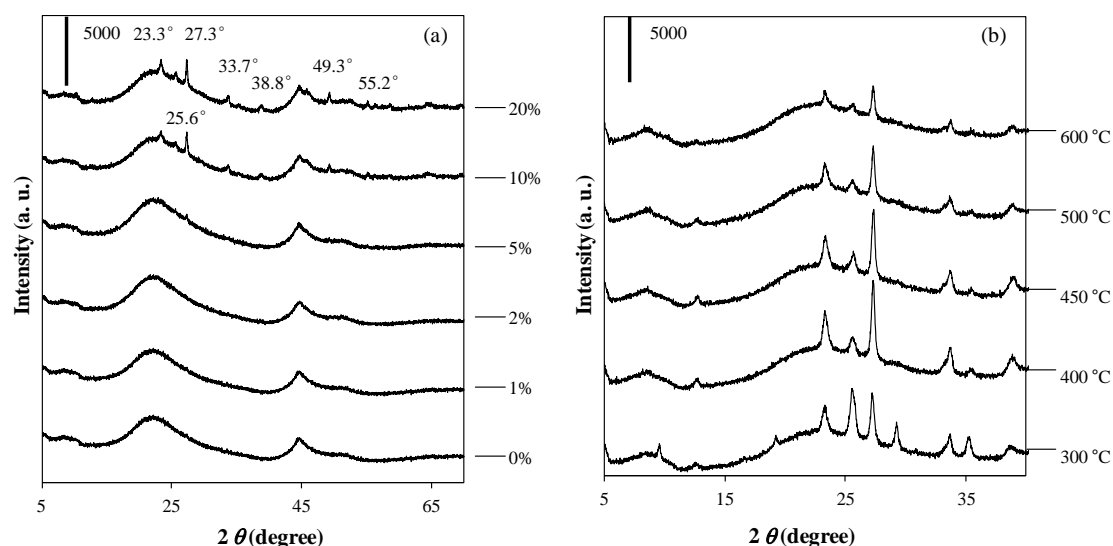


Figure 3-1 XRD patterns of 1 ~ 20 wt. % MoO₃/SiO₂ calcined at 500 °C (a) and 20 wt. % MoO₃/SiO₂ obtained at different calcination temperatures (b)

For comparison, the XRD pattern of pure SiO₂ is included. The patterns show the amorphous nature of the material at low MoO₃ loadings. At low loadings (< 5 wt. %), no characteristic diffraction peaks of crystalline MoO₃ were detected in the XRD spectra of MoO₃/SiO₂ (Figure 3-1 (a)). At higher loadings (> 5 wt. %), characteristic diffraction peaks of crystalline MoO₃ were observed at 23.3, 25.6, 27.3, 33.7, 38.8, 49.3 and 55.2 degree (2θ). It is well known that crystalline MoO₃ exhibits an orthorhombic (α -MoO₃) and a metastable monoclinic (β -MoO₃) crystal phase. ^[18, 19] At high MoO₃ loading degree (10 ~ 20 wt. %), the presence of α -MoO₃ with a characteristic diffraction peak at 12 degree (2θ) corresponding to the (020) crystalline phase was identified. The most probable impurity, MoO₂, was not observed for any of the materials. ^[20] Post-synthetic thermal treatments on 20 wt. % MoO₃/SiO₂ favored the formation of α -MoO₃ following the dehydration of β -MoO₃. ^[21] As shown in Figure 3-1 (b), the crystallinity of MoO₃/SiO₂ calcined at temperature range of 400 ~ 500 °C is considerably higher than that of the materials calcined at lower temperature (300 °C), as indicated by the diffraction intensity of the peak located at 12 degree (2θ). At higher calcination temperature (600 °C), the α -MoO₃ had a lower crystallinity, due to the temperature enabled surface reorganization as a consequence of oxygen release from the crystal lattice to the gas phase during calcination, leading to more oxygen

vacancy and a reduced crystallinity. [22] It is important to note that the SiO₂ support still retains its amorphous nature even at high MoO₃ loadings, leading to the high surface area of the materials.

The Raman spectra of MoO₃/SiO₂ catalysts with different loadings are shown in Figure 3-2.

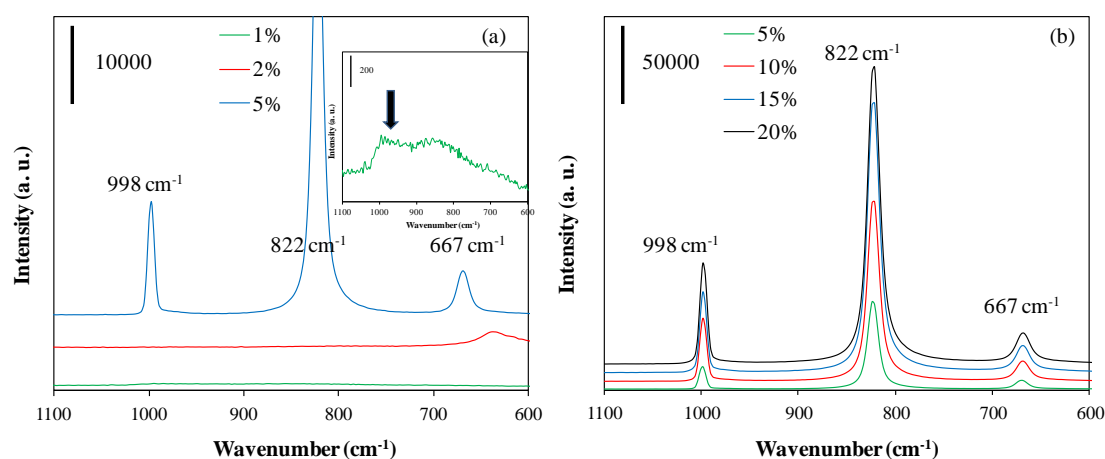


Figure 3-2 Raman spectra of 1 ~ 5 wt. % MoO₃/SiO₂ (a) and 5 ~ 20 wt. % MoO₃/SiO₂ (b) calcined at 500 °C

The Raman spectra of the materials with low MoO₃ content (< 5 wt. %) do not show the typical bands for crystalline MoO₃. Importantly, the very weak and broad Raman band at 900 ~ 1000 cm⁻¹ observed in the spectra of materials with low MoO₃ loadings (Figure 3-2 (a) inset) is attributed to both Mo=O and Si-O stretching modes from amorphous surface silicomolybdc species. [23] It is speculated that the initial formation of surface silicomolybdc species similarly counts for the reduction of the specific surface area of the materials with 1 ~ 5 wt. % MoO₃ on SiO₂ (Section 3.7, Figure 3-11 (a)) and for the lack of typical XRD patterns in the XRD spectra recorded. In contrast, Raman spectra recorded for the materials with high MoO₃ content (5 ~ 20 wt. %) deposited on SiO₂ show three main bands characteristic for terminal Mo=O (998 cm⁻¹), Mo-O-Mo unit in one-dimension of α -MoO₃ structure (822 cm⁻¹) as well

as for the multi-linkage of Mo-O unit in crystalline MoO₃ (667 cm⁻¹). Typical Raman bands for β -MoO₃ with monoclinic structure, located between 830 and 850 cm⁻¹, were not observed, further strengthening the hypothesis deduced from XRD analysis that only α -MoO₃ phase is present in the crystalline MoO₃.^[23, 24]

The presence of Lewis acidic sites on surface coordinatively unsaturated MoO₃/SiO₂ was ascertained by measuring the IR spectra of adsorbed pyridine (Figure 3-3).

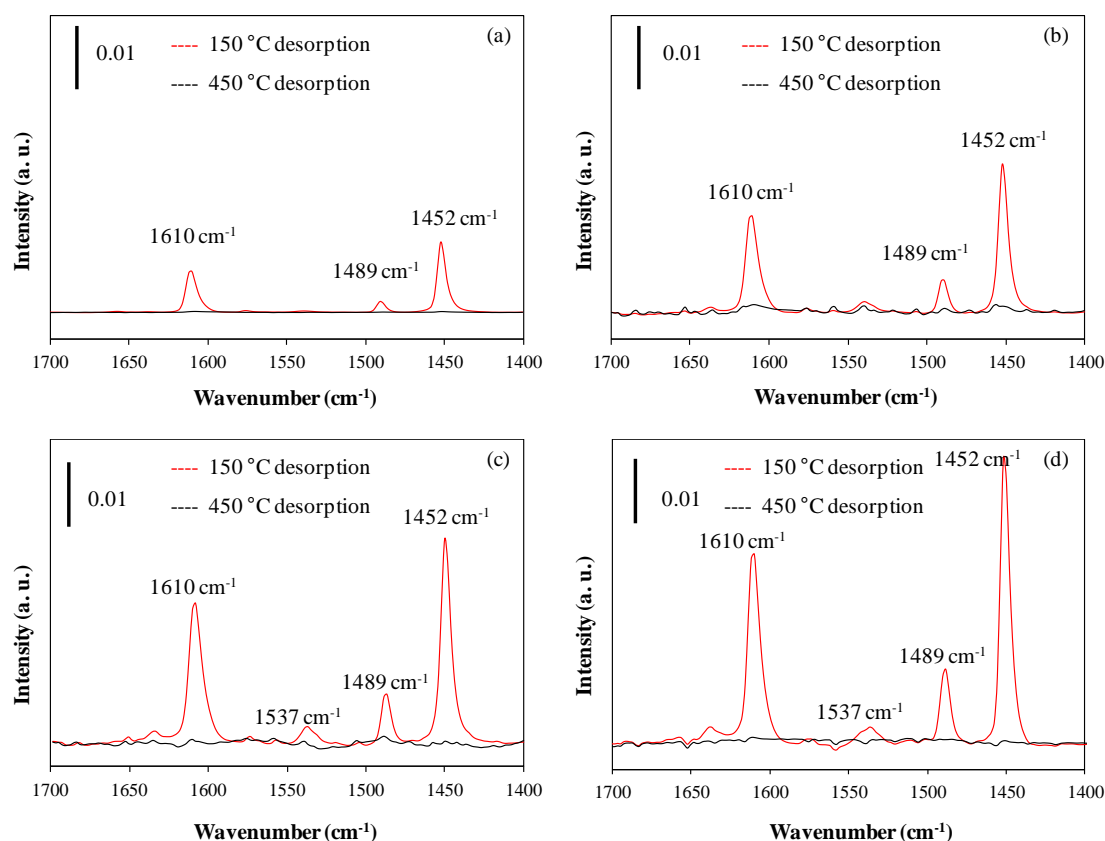


Figure 3-3 IR spectra of adsorbed pyridine on MoO₃/SiO₂ catalysts with MoO₃ loading of 5 wt. % (a), 10 wt. % (b), 15 wt. % (c) and 20 wt. % (d)

The band at 1452 cm⁻¹, which is attributed to pyridine coordinated to surface LAS, was observed for all the studied MoO₃/SiO₂ catalysts. In addition, the band at 1537 cm⁻¹, assignable to pyridinium ion in the spectrum of MoO₃/SiO₂, indicates the presence of very low concentration of surface BAS (Figure 3-3 (c) and (d)). The other

two bands (1489 and 1610 cm^{-1}) can be attributed in both LAS and BAS. [25] Moreover, after desorption at $450\text{ }^{\circ}\text{C}$, all the IR bands diminished, indicating that all the surface acidic sites are weak acidic sites.

3.3.2 MoO_3 -catalyzed transesterification of DMC with phenol

The complex reaction network involves the primer formation of MPC and anisole on transesterification and alkylation reaction pathways, respectively. As products of the consecutive reaction, DPC and cresol isomers are formed. As the first attempt to unravel the correlation between physicochemical properties of the MoO_3 -based catalysts and catalytic activity, the influence of the support on the transesterification of DMC with phenol was studied by using 20 wt. % MoO_3 deposited on various supports having additional acidic (Al_2O_3), basic (CaO) and both acidic and basic (ZrO_2) sites, and compared with the MoO_3 deposited on neutral SiO_2 support. As reference, the unsupported MoO_3 synthesized by pyrolysis of $(\text{NH}_4)_6\text{Mo}_7\text{O}_{24} \cdot 7\text{ H}_2\text{O}$ was considered. The final composition of the reaction mixture was analyzed after time on stream of 3 hours (Figure 3-4).

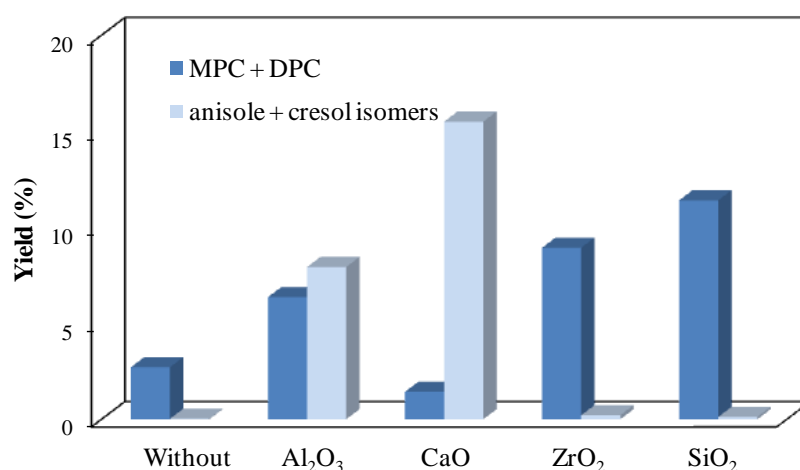


Figure 3-4 Comparison on the catalytic performance of MoO_3 deposited on different supports (Reaction conditions: 11.4 g phenol, 109 g DMC, 0.5 g supported MoO_3 catalysts or 0.1 g unsupported MoO_3 catalyst, MoO_3 loading of each catalyst 20 wt. %, reaction time 3 hours, reaction temperature $160\text{ }^{\circ}\text{C}$.)

Results of the comparative study shown in Figure 3-4 revealed that the Lewis acidic and basic sites of the support have a direct implication in the catalytic activation processes and strongly influence the overall chemoselectivity of MoO₃. Unsupported MoO₃ with crystalline α -phase is highly selective for transesterification. However, unsupported crystalline α -MoO₃ showed very low activity due to its extremely low surface area (5 m² g⁻¹). The use of MoO₃ deposited on Al₂O₃ bearing strong LAS, the selectivity of MPC and DPC is rather was (44.5 %), while high concentrations of alkylation products (55.4 %) were monitored in the composition of the final reaction mixture. The highest overall selectivity to by-products was observed in the case of CaO supported MoO₃. Strong Lewis basic sites of CaO favor the decarboxylation of MPC and formation of undesired by-products. SiO₂ and ZrO₂ supported MoO₃ materials had similar high chemoselectivities (99.0 % and 97.7 %, respectively). Importantly, the SiO₂ supported MoO₃ catalyst shows the highest activity (transesterification yield of 11.4 % compared to 8.9 % for ZrO₂ supported MoO₃, Figure 3-4).

Following the structural analysis of the sites located on the active MoO₃/SiO₂ catalysts, *i.e.*, terminal Mo=O, accessible bridged Mo-O-Mo and Mo-(O)_n-Mo ($n > 1$), have been considered as being important for the selective transesterification (Figure 3-2). To distinguish in-between the contribution of different active sites on the sequential and parallel reaction network and to identify key parameters influencing the overall selectivity of the MoO₃ catalysts, detailed kinetic analysis was performed at phenol conversion lower than 2 %. Thus, the reaction network can be simplified as that MPC and anisole are the only products formed at this low conversion. Initial rates of MPC formation determined in the presence of MoO₃/SiO₂ catalysts with different MoO₃ loading and 20 wt. % MoO₃/SiO₂ prepared at different temperatures are shown in Figure 3-5 (a) and (b).

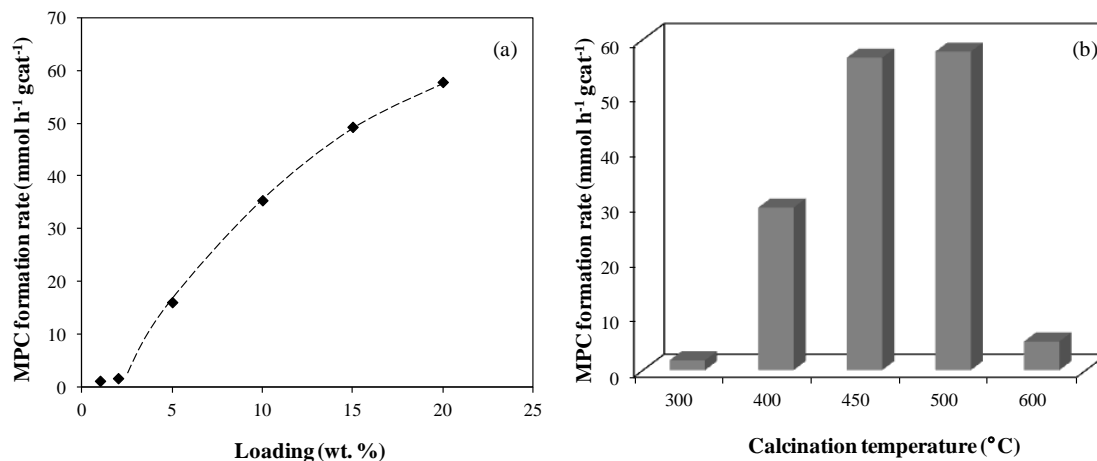


Figure 3-5 Transesterification of DMC with phenol in the presence of MoO₃/SiO₂ with different MoO₃ loadings (a) and in the presence of 20 wt. % MoO₃/SiO₂ calcined at different temperatures (b) (Reaction conditions: 11.4 g phenol, 109 g DMC, 0.1 g MoO₃/SiO₂ catalyst (calcined at 500 °C for (a)), reaction temperature 160 °C.)

At low MoO₃ loadings (< 5 wt. %) on SiO₂, when amorphous surface silicomolybdic species are preferentially formed (Figure 3-2), the materials showed a rather low catalytic activity for MPC formation (Figure 3-5 (a)). In contrast, starting from 5 wt. % of MoO₃ loading, the reaction rate continuously increased with increasing MoO₃ loading. Combining activity results (Figure 3-5 (a) and (b)) with the results from XRD analysis (Figure 3-1), it can be revealed that nanocrystalline α -MoO₃ is the most important active phase of the catalysts. Notably, the high surface area of the MoO₃/SiO₂ has an important role in the accommodation of larger amounts of nanocrystalline α -MoO₃ with increasing MoO₃ loading and further positively influence the transesterification reaction course. Therefore, the unique surface properties of SiO₂ able to accommodate highly active nanocrystalline α -MoO₃ clusters are of critical importance for the transesterification of DMC with phenol.

As shown in Figure 3-5 (b), with the same MoO₃ loading, the catalysts calcined at the temperature range of 400 ~ 500 °C showed significantly higher activity for MPC formation. From the results of XRD measurements (Figure 3-1), it is known that such samples have a high content on α -MoO₃ phase. In contrast, the other two samples

(calcined at 300 and 600 °C having a low content on crystalline α -MoO₃) showed limited catalytic activity for MPC formation.

In order to identify the main interaction processes enabled on various site of MoO₃/SiO₂, the DMC adsorption on 20 wt. % MoO₃/SiO₂ catalyst was studied at (160 °C). The catalyst surface transformation and transient formation of reactive intermediates were analyzed by *in-situ* Raman and IR spectroscopy, respectively (Figure 3-6).

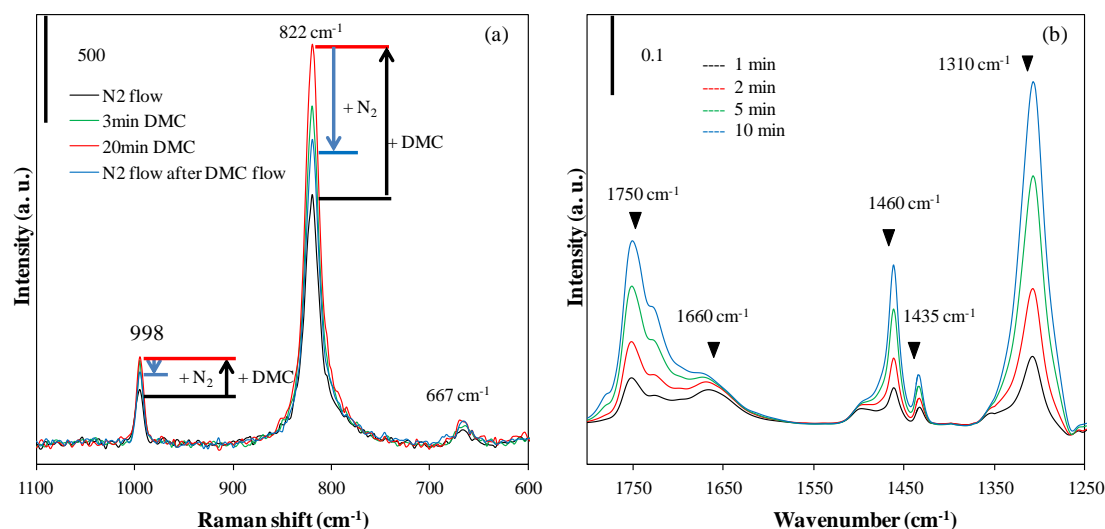


Figure 3-6 *In-situ* Raman spectra of 20 wt. % MoO₃/SiO₂ catalyst contacted with DMC vapor at 160 °C (a) and *in-situ* IR spectra of adsorbed DMC ($p = 5$ mbar) on 20 wt. % MoO₃/SiO₂ at 160 °C (b)

Recorded Raman spectra of 20 wt. % MoO₃/SiO₂ under inert conditions (N₂ flow at 160 °C, Figure 3-6 (a)) showed three characteristic bands at 998, 822 and 667 cm⁻¹, corresponding to terminal Mo=O bond, Mo-O-Mo and Mo-(O)_n-Mo ($n > 1$). By addition of DMC, the unique behavior of each coordinatively unsaturated site located on the surface of MoO₃/SiO₂ catalyst was monitored. The results of *in-situ* Raman spectroscopic analysis evidenced that DMC addition leads to an increase in Raman band intensities at terminal Mo=O and one dimensional Mo-O-Mo sites on the

catalyst surface. In contrast, the change on Mo-(O)_n-Mo ($n > 1$) was negligibly small (Figure 3-6 (a)). It was interesting to observe that the DMC chemisorption enabled on the surface Mo-O-Mo sites is reversible under inert conditions, while the interaction at terminal Mo=O sites is totally irreversible. These experiments emphasize the importance of Mo-O-Mo site for reversible DMC adsorption. For the further characterization of transiently formed surface intermediates, *in-situ* IR studies on the DMC adsorption were performed. Figure 3-6 (b) shows the IR spectra of adsorbed DMC at reaction temperature (160 °C). It was evidenced that 10 min exposure time was sufficient for reaching the adsorption equilibrium between surface bidentate carbonate groups and molecular DMC at 160 °C. The band at 1750 cm⁻¹ and two shoulder bands are attributed to C=O stretching vibration of molecular DMC with different adsorption states,^[27] while the band at 1660 cm⁻¹ is attributed to the presence of bidentate carbonate groups.^[28] In addition, the bands at 1460, 1435 (C-H bending vibration of the methyl groups) and 1310 cm⁻¹ (asymmetric O-C-O stretching vibration) can be assigned to both molecular DMC and surface bidentate carbonate groups.

To further investigate the stability of formed surface species, after the adsorption of DMC molecule, desorption from MoO₃/SiO₂ catalyst was performed in vacuum ($p < 10^{-5}$ mbar) under isothermal conditions (160 °C). The corresponding IR spectra recorded during desorption are shown in Figure 3-7.

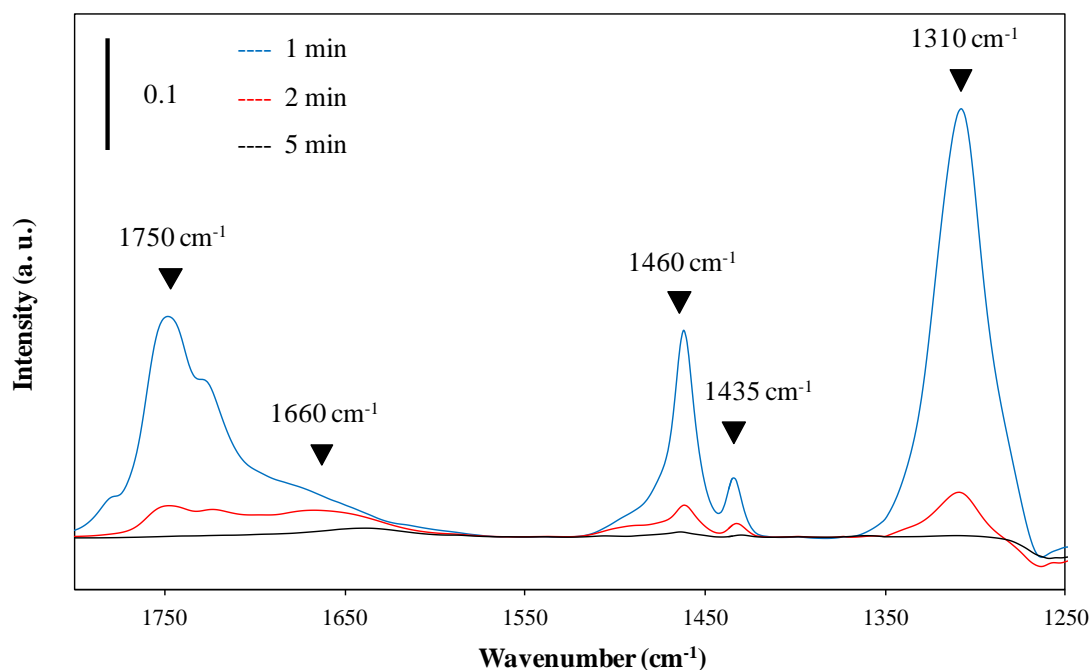


Figure 3-7 IR spectra of adsorbed DMC on 20 wt. % MoO₃/SiO₂ catalyst during desorption at 160 °C (The catalyst was exposed to DMC vapor ($p = 5.0$ mbar) at 160 °C for 30 min prior to desorption.)

Prior to desorption, it was clearly shown that all bands referring to both molecular DMC and surface bidentate carbonate groups are concomitantly present on the surface. During desorption, the intensity of all characteristic bands depressed rapidly, indicating that the stability of transiently formed surface species is rather low, so that a weak and reversible interaction between DMC and MoO₃/SiO₂ catalyst is assumed under the selected experimental conditions.

Aiming the identification of DMC activation process in the presence of phenol-based intermediates, MPC was used as a second adsorbate for *in-situ* IR measurement. Since MPC contains both aliphatic and aromatic moieties, it can serve indirectly to the elucidation of the main pathways of DMC / phenol activation. Typical IR spectra recorded during MPC interactions are shown in Figure 3-8.

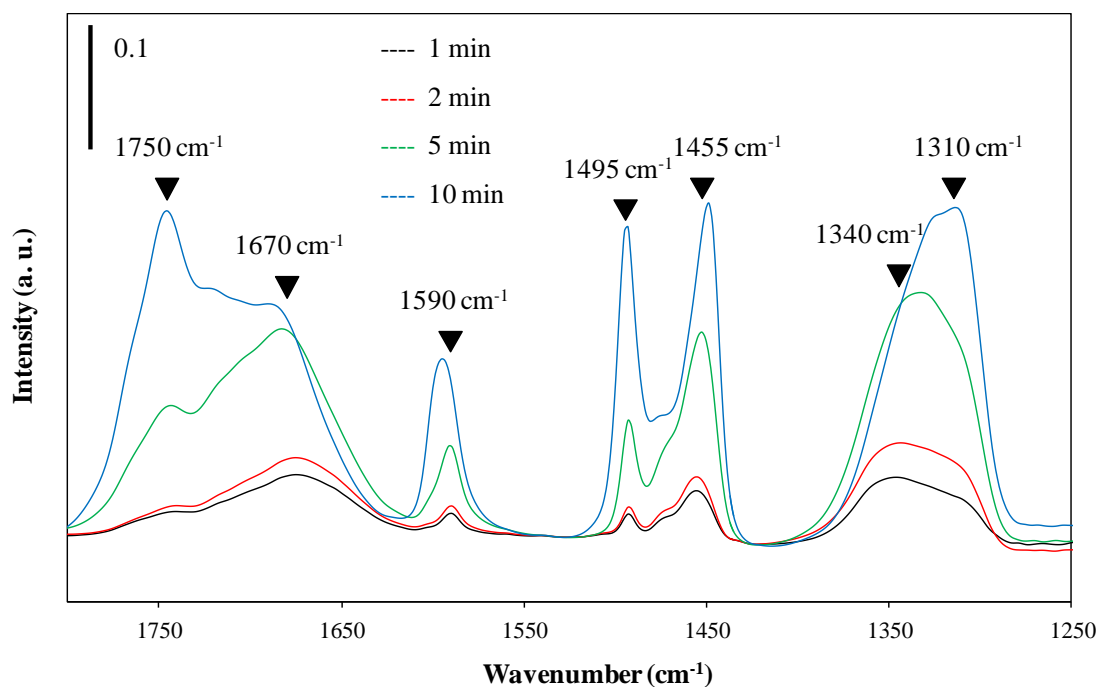


Figure 3-8 IR spectra of adsorbed MPC ($p = 5$ mbar) on 20 wt. % $\text{MoO}_3/\text{SiO}_2$ at 160 °C

The interaction of MPC with the active sites located on the surface of 20 wt. % $\text{MoO}_3/\text{SiO}_2$ catalyst was investigated by the exposing the catalyst to DMC vapor at 160 °C. The IR spectra recorded after the adsorption of MPC give the evidence of the characteristic bands of the aromatic ring and of carbonyl species, indicating the co-existence of aromatic and carbonyl species on the surface at 160 °C. The band at 1750 cm^{-1} is attributed to C=O stretching vibration of molecular MPC. The bands at 1670 , 1455 , 1340 , 1310 cm^{-1} indicate the presence of bidentate carbonate groups, similar as in the case of DMC adsorption. In addition, the bands at 1590 cm^{-1} and 1495 cm^{-1} are assigned to different modes of C-C stretching vibration in the aromatic ring.^[29, 30] Compared to the IR spectra of adsorbed DMC (Figure 3-6 (b)), the band at 1660 cm^{-1} attributed to C=O stretching vibrations of the surface carbonate species is shifted to 1670 cm^{-1} , due to the effect of the neighboring aromatic moiety. Moreover, there was only one sharp band at 1310 cm^{-1} attributed to O-C-O stretching vibrations in the case of DMC adsorption, while a new broad band at 1340 cm^{-1} and a shoulder

band at 1325 cm^{-1} were observed if MPC was used as adsorbate.

The stabilities of different surface species after MPC adsorption were studied by isothermal desorption (similar as in the case of DMC), followed by desorption conducted at elevated temperatures. The experimental results are shown in Figure 3-9.

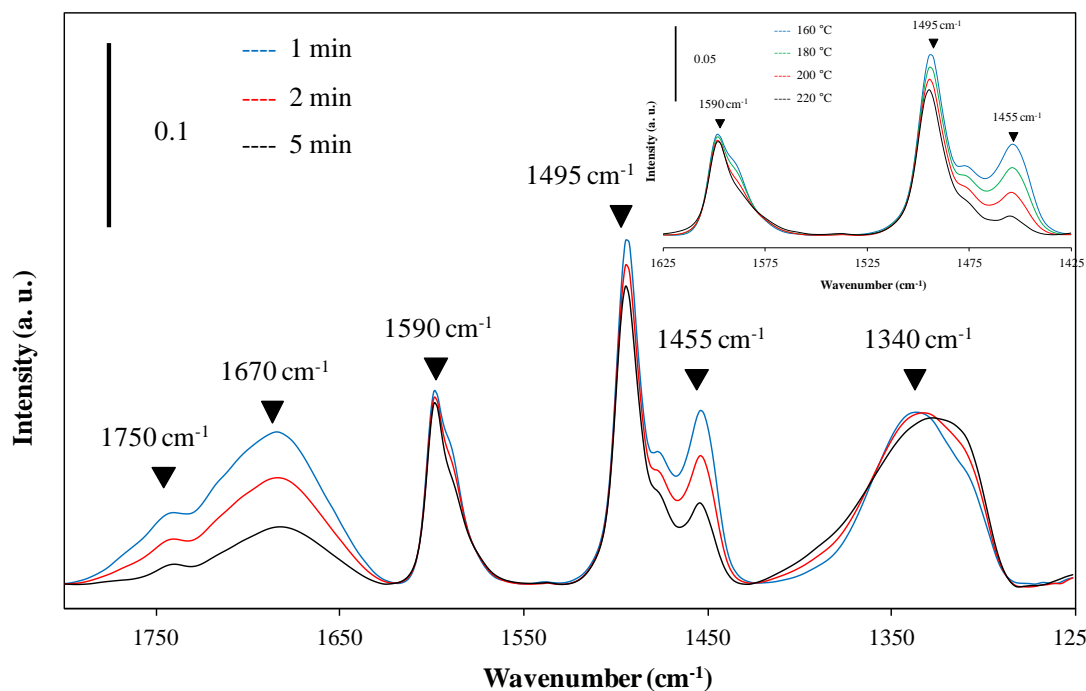


Figure 3-9 IR spectra of adsorbed MPC on 20 wt. % $\text{MoO}_3/\text{SiO}_2$ recorded during desorption (Main figure shows the spectra recorded during isothermal desorption at $160\text{ }^\circ\text{C}$. The inset figure shows the spectra recorded during temperature programmed desorption from 160 to $220\text{ }^\circ\text{C}$. The catalyst was exposed to MPC vapor ($p = 5.0\text{ mbar}$) at $160\text{ }^\circ\text{C}$ for 30 min prior to desorption.)

Based on the results of the stability tests (Figure 3-9), the blue shift of C=O stretching vibration band (from 1660 to 1670 cm^{-1}) as well as the splitting of O-C-O stretching vibration band (from one single band at 1310 cm^{-1} to two neighboring bands at 1310 and 1325 cm^{-1}) indicate a stronger chemical bonding in -O-(CO)-O- unit on the catalyst with neighboring aromatic species than that without the presence of aromatic species. Even at $220\text{ }^\circ\text{C}$ in vacuum ($60\text{ }^\circ\text{C}$ higher than the adsorption temperature), the characteristic bands of aromatic ring (1590 and 1495 cm^{-1}) are still present in the

IR spectra without depression of intensity, while the intensity of a neighboring band attributed to aliphatic carbonate species (1455 cm^{-1}) considerably decreased. It is, therefore, consequently deduced that the interaction between the carbonyl group and catalyst surface is weakened by the co-present aromatic group. This investigation further implies a competitive adsorption of DMC and phenol on the catalyst surface during the activation processes.

As one of the most important kinetic features relevant for understanding the nature of interactions between the reactant molecules and catalysts, the reaction orders of both reactants, *i.e.*, phenol and DMC, were determined by using the double logarithmic plots of the initial rates of MPC formation *vs.* starting concentration of the corresponding reactant on the most active catalyst, *i.e.*, 20 wt. % $\text{MoO}_3/\text{SiO}_2$, as shown in Figure 3-10.

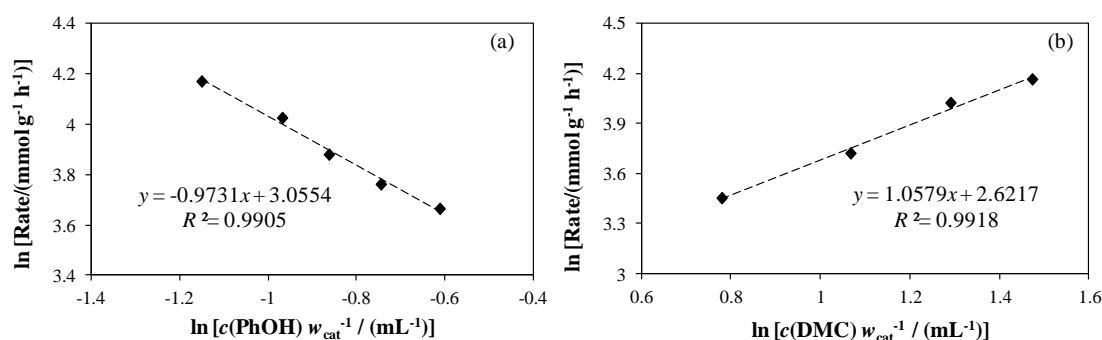


Figure 3-10 Determination of reactants reaction order on MPC formation over 20 wt. % $\text{MoO}_3/\text{SiO}_2$ catalyst (Reactions were performed in the 300 mL autoclave and the total volume of all reagents were between 100 and 150 mL, reaction temperature $160\text{ }^\circ\text{C}$.)

From the conducted kinetic measurements, it can be concluded that the reaction orders of phenol and DMC are -1 and 1, respectively. This observation is in agreement with the facts that the reaction follows Langmuir-Hinshelwood model, *i.e.*, both reactants are adsorbed before the surface reaction starts, and, more important, a competitive adsorption of the two reactants takes place on the same active sites during the catalytic reaction (a detailed kinetic model is available in Section 3.7.2).^[31]

3.4 Discussion

The basic structural unit of crystalline MoO_3 is MoO_6 octahedron. In α - MoO_3 phase, the distorted octahedral share edges and form chains which are cross-linked by oxygen atoms to further form layers. In contrast, in β - MoO_3 phase, the chains composed by edge-sharing octahedral are disturbed by crystalline water.^[21] The presence of crystal water hinders the chain and layer formation, so that the formation of β - MoO_3 phase is favored at low temperatures (< 400 °C). At elevated temperatures ($400 \sim 500$ °C), the formation of α - MoO_3 is achieved following the total dehydration of β - MoO_3 phase. When the calcination temperature is even higher (> 500 °C), however, the mobilization of lattice oxygen atoms becomes significant, producing large amount of oxygen vacancies in the crystal lattice so that crystallinity and the concentration of Mo-O-Mo unit are reduced.

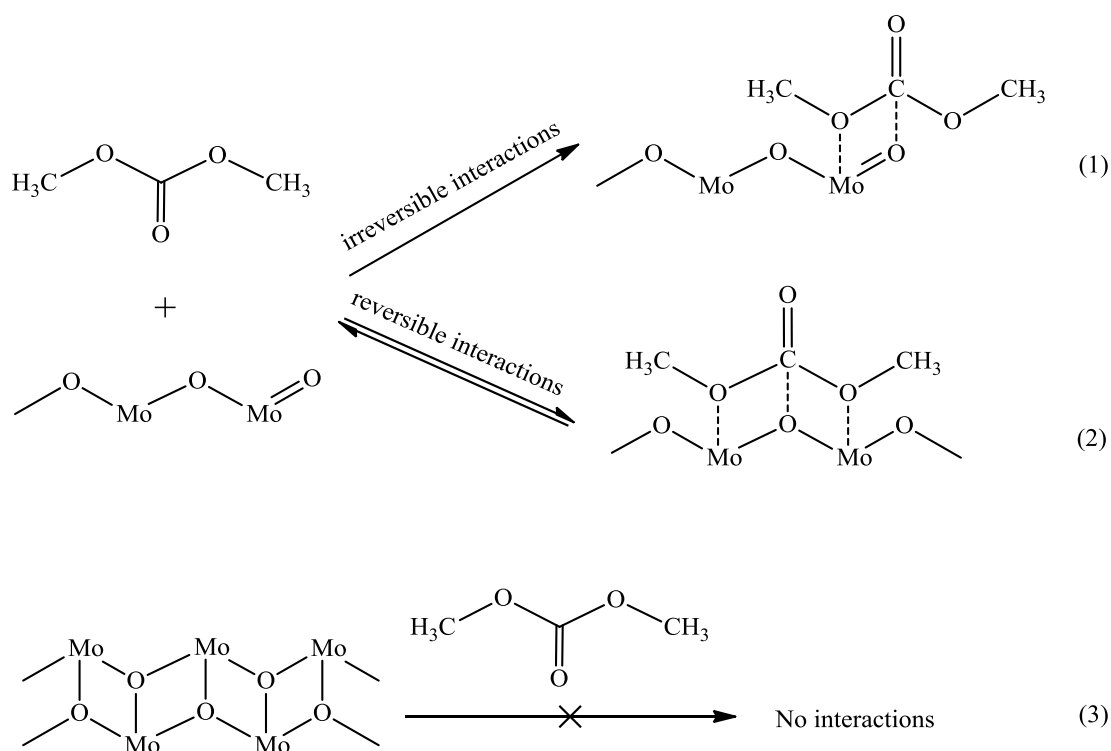
Different surface units, *i.e.*, terminal Mo=O, one dimensional Mo-O-Mo and Mo-(O)_n-Mo ($n > 1$), are present on the surface of MoO_3 catalysts. Mo=O site is mainly located on the edges and vacancies. Therefore, the materials with large content of β - MoO_3 where the edge-sharing octahedral are disturbed by crystal water and the materials prepared at high temperature with large oxygen vacancies have high concentration of terminal Mo=O sites. In contrast, the formation of Mo-O-Mo unit requires a well-ordered and cross-linked chain structure, which is only enabled in crystalline α - MoO_3 .

MoO_3 itself has rather low surface area (*ca.* $5 \text{ m}^2 \text{ g}^{-1}$). Therefore, a porous support with large surface area is required for the accommodation of highly active MoO_3 particles and for the enhancement of the catalytic activity. At the same time, the support needs to possess high thermal and chemical stability. In the case of

MoO₃/SiO₂, the particle size of MoO₃ was in the range of 10 nm (determined from XRD patterns shown in Figure 3-1 (b) by using Scherrer equation), which is much smaller than that of unsupported MoO₃ particles (> 100 nm) synthesized by using similar thermal treatment.^[26] Therefore, a much higher dispersion of MoO₃ is achieved by using SiO₂ as a support. Moreover, the dispersed nanocrystalline MoO₃ particles did not block or collapse the porous structure of SiO₂ (Section 3.7, Figure 3-11). In order to disperse the highest concentration of active MoO₃ phase, the loading of MoO₃ should also be carefully considered. Crystalline α -MoO₃ can only be formed at loadings higher than 5 wt. %, while MoO₃ loading higher than 20 wt. % leads to significant depression of the pore volume. Therefore, for a good dispersion of active MoO₃ particle, the loading should be controlled at 20 wt. %.

In the catalytic transesterification of DMC with phenol, surface coordinatively unsaturated sites were proposed as the active center responsible for selective transesterification and a catalytic cycle was accordingly proposed in previous publication.^[7] However, there is no existing information concerning the interaction ability of various Lewis acidic / basic sites identified in the composition of the active α -MoO₃.

The *in-situ* IR and Raman studies on the DMC interaction with MoO₃ surface evidenced that the associative adsorption of DMC preferentially takes place on the Lewis acidic / basic pairs of Mo-O-Mo unit similar as previously proposed on other Lewis acidic / basic sites.^[27, 28] As a result, a surface symmetrical carbonate species is formed as a consequence of the electrostatic interactions of the organic molecule with the active Lewis acidic / basic Mo-O-Mo sites, as shown in Scheme 3-2.

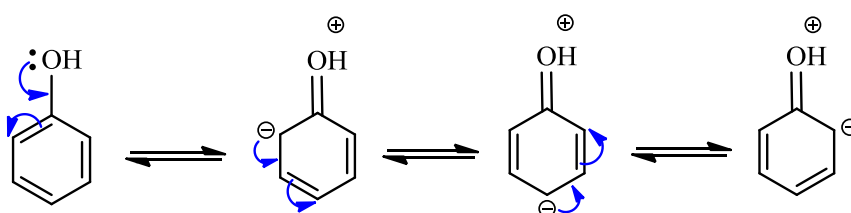


Scheme 3-2 Proposed interactions between DMC molecule and different surface sites on MoO_3

The nucleophilicity of oxygen atom is different at terminal $\text{Mo}=\text{O}$ as in $\text{Mo}-\text{O}-\text{Mo}$ and $\text{Mo}-(\text{O})_n-\text{Mo}$ ($n > 1$) units. The Hückel charge of oxygen atom in $\text{Mo}=\text{O}$, $\text{Mo}-\text{O}-\text{Mo}$ and $\text{Mo}-(\text{O})_n-\text{Mo}$ ($n > 1$) units is -1.3, -1.1 and -0.8, respectively (calculated by using Chem 3D Pro, Version 12.0.2.1076). High oxygen nucleophilicity in terminal $\text{Mo}=\text{O}$ sites (Hückel charge -1.3), due to its high coordinative unsaturation level, leads to a strong adsorption of DMC molecule, further blocking the sites (Scheme 3-2 (1)). This strong interaction might further lead to the dissociation of chemisorbed DMC molecule.^[26, 36] In contrast, low oxygen nucleophilicity in $\text{Mo}-(\text{O})_n-\text{Mo}$ ($n > 1$) (Hückel charge -0.8) and the coordinative saturation of the sites hinder the DMC adsorption. Only accessible $\text{Mo}-\text{O}-\text{Mo}$ sites with mild nucleophilicity of oxygen (Hückel charge -1.1) enables the reversible DMC adsorption (Figure 3-6 and 3-7). As evidenced by *in-situ* IR studies, it is worth mentioning that the interaction between DMC and surface $\text{Mo}-\text{O}-\text{Mo}$ unit is strong

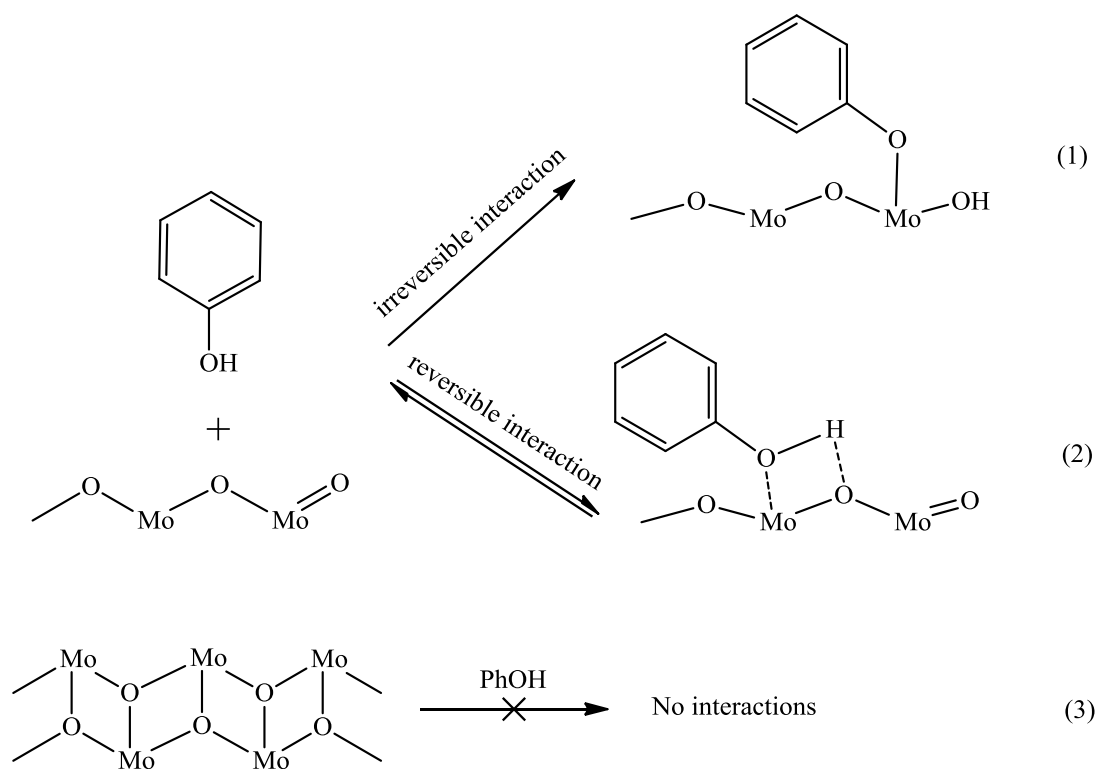
enough to activate C-O bond via carbonyl group but not to irreversibly block the active sites hindering further catalytic transformations.

In a reaction mixture of phenol and DMC, the surface interaction of phenol was considered in parallel. From the resonance structure of phenol, it is well known that the aromatic ring has nucleophilicity comparable with free amines, owing to the nucleophilicity of the carbon located at *ortho*- and *para*-positions (Scheme 3-3).



Scheme 3-3 Resonance structure of phenol molecule

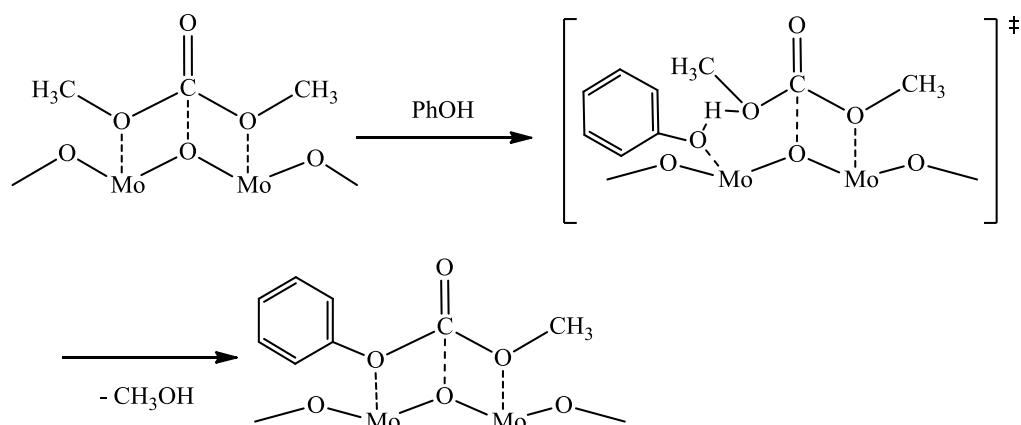
Therefore, the O-H bond of the phenolic hydroxyl group is able to be activated on Lewis acidic / basic pairs. It is important to note that the sites favoring DMC adsorption are also the sites where phenol adsorption is supposed to take place. On different surface units on MoO₃ catalyst, the surface adsorption form of phenol is also different (Scheme 3-4).



Scheme 3-4 Surface adsorption of phenol

As discussed above, the nucleophilicity of oxygen in terminal Mo=O sites (Hückel charge -1.3) is too strong, leading to the dissociative adsorption of phenol molecule and the formation of the surface stable phenoxide species. In addition, the nucleophilicity of oxygen in Mo-(O)_n-Mo (*n* > 1) units is too weak, so that no effective interaction takes place. Therefore, it is rationalized that phenol adsorption occurs on the Mo-O-Mo units of α -MoO₃ with mild oxygen nucleophilicity, resulting in a better accommodation of phenol molecule, as depicted in Scheme 3-4 (2).

In the co-presence of DMC, the proton from phenol molecule is preferentially interacting with the oxygen atom of the carbonyl moiety, forming an energetically favored 6-membered transition state (Scheme 3-5).



Scheme 3-5 Competitive adsorption of phenol and DMC on the surface and formation of MPC

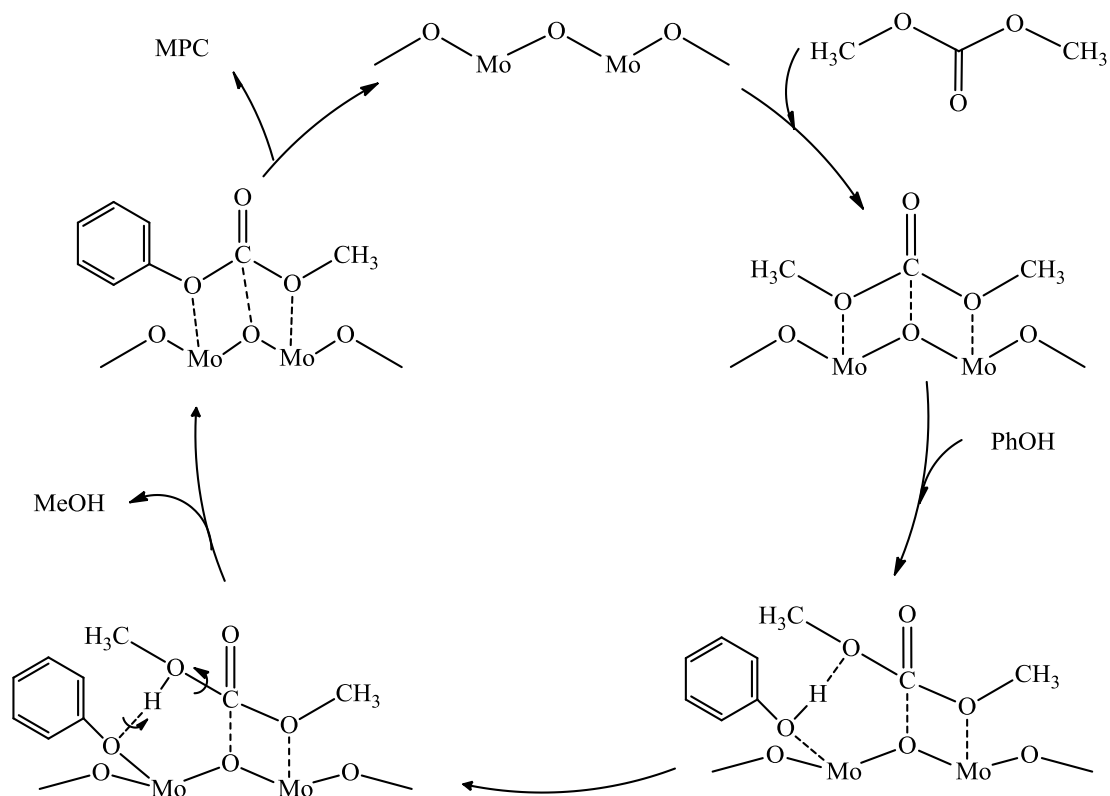
The electron density of oxygen atom in carbonyl group of DMC molecule (Hückel charge -1.3 calculated by using Chem 3D Pro, Version 12.0.2.1076) is comparable to that of oxygen atom in Mo-O-Mo unit. Comparing the chemical environment of two different oxygen atoms, *i.e.*, the one in Mo-O-Mo site and the one in carbonyl group of DMC molecule, the lone pair electron of oxygen atom in Mo-O-Mo sites is shared by the d orbital of Mo atom, while the lone pair electron of oxygen atom in carbonyl group cannot be donated since the neighboring carbon atom does not have d orbital. Consequently, the oxygen atom of DMC molecule, with its high affinity to the proton of phenol molecule, promotes the adsorption of phenol molecule on the surface LAS via the formation of a 6-membered transition state and a hydrogen bond in the transition state ring. Moreover, from the experimental results of *in-situ* IR measurements, a blue shift of characteristic IR bands for C=O and O-C-O stretching vibration (contributed from aliphatic carbonate species) is observed, when phenol-based intermediates are coexisting on the surface (Figure 3-6 and 3-8). Therefore, it is evidenced that the simultaneous presence of phenolic group on the surface Mo-O-Mo sites weakens the adsorption of DMC molecule. Furthermore, evidenced by the splitting of the characteristic IR band for O-C-O stretching vibration, the symmetrical carbonate species becomes an asymmetrical carbonate species with

the presence of phenolic species. These investigations strengthen the proposed surface transformation shown in Scheme 3-5.

After the formation of the 6-membered transition state, a methanol molecule is formed and released. The phenolic fragment has been subsequently accommodated by the surface Lewis acidic site, subsequently leading to the formation of a new C-O bond, overall resulting in the formation of product molecule MPC (Scheme 3-5).

The transesterification between carbonates and hydroxylic compounds involves the substitution of a less nucleophilic component with the more nucleophilic hydroxyl or by the substitution of the less volatile compound by the more volatile one.^[32] The transesterification of DMC with phenol to afford DPC occurs contrary to that and in consequence, a suitable catalyst is required to enable the chemical reaction at a higher rate.^[33] Based on the consideration that the resonance structure provides the nucleophilicity of the aromatic ring of phenol, the activation and deprotonation of phenol on Mo-O-Mo sites is not difficult, and therefore, not rate determining. In contrast, the C-O bond cleavage is crucial for the selective transesterification, which requires a mild interaction with Lewis acidic / basic pair. Therefore, the main role of MoO₃/SiO₂ catalyst is located on the C-O bond activation.

Combining the experimental data of catalyst characterization and IR spectroscopic measurements, following elementary steps enabled on the catalyst surface, are proposed for catalytic cycle for the most critical step in the DPC formation (Scheme 3-6).



Scheme 3-6 Proposed catalytic cycle for the MoO_3 catalyzed transesterification

The adsorption of DMC on the coordinatively unsaturated Mo-O-Mo unit at nanocrystalline $\alpha\text{-MoO}_3$ results in the transient formation of symmetric carbonate species on the surface, leading to the activation of the C-O bond. Phenol is firstly interacted with adsorbed DMC species in order to activate the O-H bond. In the presence of phenol, the concomitant formation of asymmetric carbonate takes place and the adsorption of DMC is weakened. Following the surface reconstruction and the release of a methanol molecule, phenolic species is accommodated on Lewis acidic site leading to the surface adsorbed MPC formation. This mechanism is consistent with the measured reaction orders for DMC and phenol (1 and -1, respectively, Figure 3-10). It pictures the MPC (formed following co-adsorption of DMC and phenol) as a true intermediate that can be detected and characterized by spectroscopy.

3.5 Conclusion

Active nanocrystalline α -MoO₃ supported on SiO₂ was synthesized and successfully tested for transesterification of DMC with phenol. Among terminal Mo=O sites, Mo-O-Mo and Mo-(O)_n-Mo ($n > 1$) units, the surface coordinatively unsaturated Mo-O-Mo sites, stabilized on an orthorhombic crystal lattice, are identified as responsible for the catalytic transesterification of DMC with phenol. Based on the observed negative reaction order of phenol, competitive adsorption on Lewis acidic / basic pairs of two reactants is proposed. Results from detailed *in-situ* spectroscopic measurements further support these mechanistic assumptions and enable to propose a reaction sequence that would account for MPC formation, a crucial intermediate in the process of DPC synthesis.

3.6 References

- [1] U. Curtius, L. Bottoenbruch, H. Schnell, *US Patent*, **1969**, 3442854
- [2] H. Yamana, T. Kuni, T. Furusawa, H. Nakai, Y. Hiro, *US Patent*, **1975**, 3888826
- [3] D. Brunelle, *US Patent*, **1982**, 4321356
- [4] J. B. Starr, A. Ko, *US Patent*, **1983**, 4383092
- [5] W. B. Kim, J. S. Lee, *Catal. Lett.* **1999**, 59, 83
- [6] J. Haubrock, M. Raspe, G. F. Versteeg, H. A. Kooijman, R. Taylor, J. A. Hogendoorn, *Ind. Eng. Chem. Res.* **2008**, 47, 9862
- [7] Z. Fu, Y. Ono, *J. Mol. Catal. A: Chem.* **1997**, 118, 293
- [8] H. Yasuda, K. Watarai, J. C. Choi, T. Sakakura, *J. Mol. Catal. A: Chem.* **2005**, 236, 149
- [9] F. Mei, G. Li, N. Jin, H. Xu, *J. Mol. Catal. A: Chem.* **2002**, 184, 465

-
- [10] H. Niu, J. Yao, Y. Wang, G. Wang, *Catal. Commun.* **2007**, 8, 355
- [11] Z. Du, W. Kang, T. Cheng, J. Yao, G. Wang, *J. Mol. Catal. A: Chem.* **2006**, 246, 200
- [12] K. Kawahashi, K. Murata, M. Watabiki, *US Patent*, **1995**, 5380908A
- [13] Z. Du, Y. Xiao, T. Chen, G. Wang, *Catal. Commun.* **2008**, 9, 239
- [14] W. B. Kim, J. S. Lee, *J. Catal.* **1999**, 185, 307
- [15] D. Tong, J. Yao, Y. Wang, H. Niu, G. Wang, *J. Mol. Catal. A: Chem.* **2007**, 268, 120
- [16] M. Cao, Y. Meng, Y. Lu, *Catal. Commun.* **2005**, 6, 802
- [17] A. Dibenedetto, A. Angelini, L. Bitonto, E. De Giglio, S. Cometa, M. Aresta, *ChemSusChem* **2014**, 7, 1155
- [18] J. R. Günter, *J. Solid State Chem.* **1972**, 5, 354
- [19] A. Stoyanova, R. Iordanova, M. Mancheva, Y. Dimitriev, *J. Optoelectron. Adv. Mater.* **2009**, 11, 1127
- [20] O. Marin-Flores, L. Scudiero, S. Ha, *Surf. Sci.* **2009**, 603, 2327
- [21] A. Kuzmin, J. Purans, *J. Phys.: Condens. Matter* **2000**, 12, 1959
- [22] T. Ressler, J. Wienold, R. E. Jentoft, T. Neisius, *J. Catal.* **2002**, 210, 67
- [23] M. R. Smith, L. Zhang, S. A. Driscoll, U. S. Ozkan, *Catal. Lett.* **1993**, 19, 1
- [24] L. Seguin, M. Figlarz, R. Cavagnat, J. C. Lassègues, *Spectrochim. Acta Part A* **1995**, 51, 1323
- [25] E. P. Parry, *J. Catal.* **1963**, 2, 371
- [26] L. Wang, B. Peng, L. Peng, X. Guo, Z. Xie, W. Ding, *Sci. Rep.* **2013**, 3, 2881
- [27] T. Beutel, *J. Chem. Soc. Faraday Tran.* **1998**, 94, 985
- [28] L. Bertsch, H. W. Habgood, *J. Phys. Chem.* **1963**, 67, 1621
- [29] E. B. Wilson, *Phys. Rev.* **1934**, 45, 706
- [30] J. H. S. Green, *J. Chem. Soc.* **1961**, 2236

- [31] F. Kapteijn, J. A. Moulijn, R. A. van Santen, R. Wever, *Chemical kinetics of catalyzed reaction* in *Catalysis: an Integrated Approach*, Elsevier, Amsterdam, **2000**
- [32] H.-J. Buysch, *Carbonic acid esters* in *Ullmann's Encyclopedia of Industrial Chemistry*, VCH, Weinheim, **1986**
- [33] R. Sridharan, I. M. Mathai, *J. Sci. Ind. Res.* **1974**, 33, 178
- [34] M. Bensitel, V. Moravek, J. Lamotte, O. Saur, J. C. Lavalley, *Spectrochim. Acta Part A*, **1987**, 43, 1487

3.7 Appendix

3.7.1 N_2 physisorption

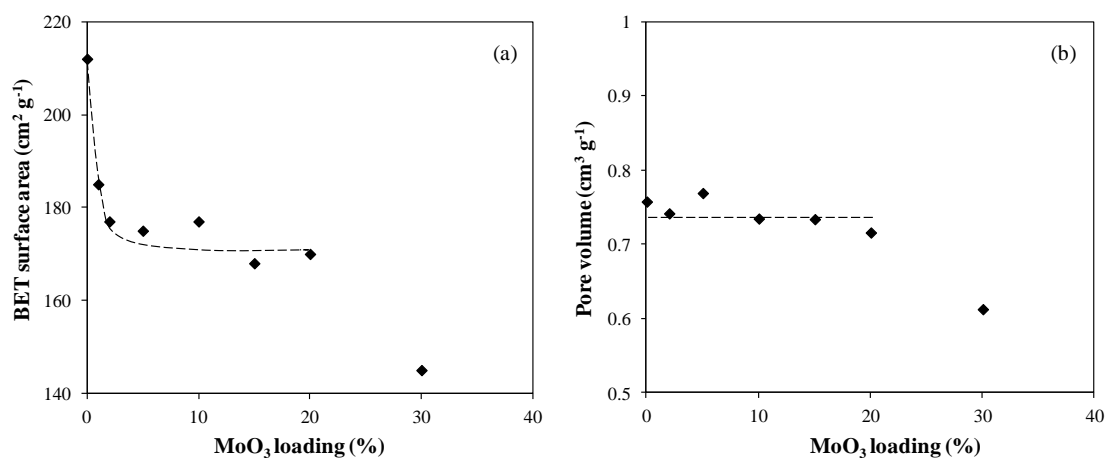


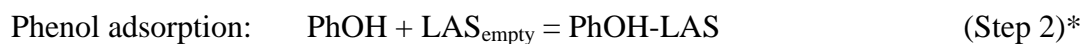
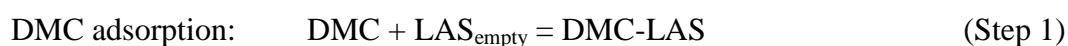
Figure 3-11 BET surface areas (a) and pore volumes (b) of MoO₃/SiO₂ catalysts with different loadings (Pore volume was determined for the pores with a size larger than 20 Å.)

3.7.2 Kinetic analysis

The measurements of kinetics revealed the reaction orders for phenol and DMC are -1 and 1, respectively. Based on the experimental observations from kinetic

measurements, a rational model of reaction sequences is proposed. A competitive adsorption on the same active site between phenol and DMC is featured in this model. From steady-state kinetic assumptions, the overall reaction rate equals to the rate of the rate determining step and all the other elementary steps are fast enough to reach equilibrium.

In the overall catalytic transformation, following 4 elemental steps were considered.



* Step 2 is actually achieved via the involvement of DMC-LAS, as $\text{PhOH} + \text{DMC-LAS} + \text{LAS}_{\text{empty}} = \text{PhOH-LAS} + \text{DMC-LAS}$. Within this elementary step (Step 2), it is assumed that the coverage of DMC is not changed, although the strength of adsorbed species has been weakened.

For simplification of the model, based on the fact that the concentration of MPC in the reaction mixture is very low thus the surface coverage of MPC is negligible, MPC desorption (Step 4) has little influence on the overall reaction rate. Therefore, only steps 1, 2 and 3 are discussed.

The rate of step 1 can be formulated as Eq. 3-1.

$$r_1 = k_1 [\text{DMC}] [\text{LAS}_{\text{empty}}]$$

Eq. 3-1

Based on the Langmuir's model, since both reactants (DMC and phenol) are competitively adsorbed on the same active sites, the concentration of unoccupied Lewis acidic sites can be formulated as Eq. 3-2.

$$[\text{LAS}_{\text{empty}}] = (1 + K_1 [\text{DMC}] + K_2 [\text{PhOH}])^{-1}$$

Eq. 3-2

Therefore, the rate of DMC adsorption will become r_1 in Eq. 3-3.

$$r_1 = k_1 [\text{DMC}] (1 + K_1 [\text{DMC}] + K_2 [\text{PhOH}])^{-1}$$

Eq. 3-3

Based on the investigation of *in-situ* IR measurements, the phenol coverage is high while the DMC coverage is low ($K_1 [\text{DMC}] \ll 1$, $K_2 [\text{PhOH}] \gg 1$, Figure 3-9). Therefore, $1 + K_1 [\text{DMC}] + K_2 [\text{PhOH}]$ reduces to $K_2 [\text{PhOH}]$, so that r_1 reduces to $k_1 K_2^{-1} [\text{DMC}] [\text{PhOH}]^{-1}$, in the same form as that the reaction orders of DMC and phenol are 1 and -1, respectively. Therefore, step 1 is considered as a possible RDS, limiting the overall transesterification.

The rate of step 2 can be expressed as Eq. 3-4.

$$r_2 = k_2 [\text{PhOH}] [\text{LAS}_{\text{empty}}]$$

Eq. 3-4

Here $[\text{LAS}_{\text{empty}}]$ represents the concentration of unoccupied surface Lewis acidic sites.

Based on the site balance shown in Eq. 3-2, the rate of phenol adsorption will become r_1 in Eq. 3-5.

$$r_2 = k_2 [\text{PhOH}] (1 + K_1 [\text{DMC}] + K_2 [\text{PhOH}])^{-1}$$

Eq. 3-5

As discussed above, $1 + K_1 [\text{DMC}] + K_2 [\text{PhOH}]$ reduces to $K_2 [\text{PhOH}]$, thus r_2 reduces to a constant $k_2 K_2^{-1}$, independent by the concentration of phenol. This would imply an observed reaction order of 0 for phenol, being in contradiction with experimental results (Figure 3-10). Thus, step 2 (phenol adsorption) is not RDS.

The rate of step 3 is shown in Eq. 3-6.

$$r_3 = k_3 [\text{LAS} - \text{DMC}] [\text{LAS} - \text{PhOH}]$$

Eq. 3-6

Here LAS-PhOH and LAS-DMC represent the active sites where phenol and DMC were adsorbed, respectively.

Based on the Langmuir's model, the concentration of active sites occupied by phenol and DMC can be calculated as Eq. 3-7.

$$\begin{aligned} [\text{DMC} - \text{LAS}] &= K_1 [\text{DMC}] (1 + K_1 [\text{DMC}] + K_2 [\text{PhOH}])^{-1} \\ [\text{PhOH} - \text{LAS}] &= K_2 [\text{PhOH}] (1 + K_1 [\text{DMC}] + K_2 [\text{PhOH}])^{-1} \end{aligned}$$

Eq. 3-7

Therefore, the rate of step 3 (Eq. 3-6) will become r_3 in Eq. 3-8.

$$r_3 = k_3 K_1 K_2 [\text{DMC}] [\text{PhOH}] (1 + K_1 [\text{DMC}] + K_2 [\text{PhOH}])^{-2}$$

Eq. 3-8

Under the above assumptions that $1 + K_1 [\text{DMC}] + K_2 [\text{PhOH}]$ reduces to $K_2 [\text{PhOH}]$, the rate of step 3 (Eq. 3-8) will become $k_3 K_1 K_2^{-1} [\text{DMC}] [\text{PhOH}]^{-1}$, in the same form as that the reaction orders of DMC and phenol are 1 and -1, respectively. Therefore, surface reaction (step 3) is similarly considered as a rate limiting step.

As a conclusion, the kinetic model with assumption of surface competitive adsorption fits well with the experimental observation. Moreover, the DMC-involved elementary steps are identified as possible RDS(s).

Chapter 4

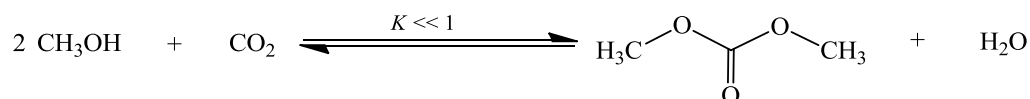
Optimization of a two-step process for the phosgene-free DPC production

In the phosgene-free pathway of the DPC synthesis presented in the current thesis, both the DMC formation from methanol and CO₂ and the transesterification of DMC with phenol are strongly equilibrium constrained reactions. In order to enhance product yield, several microcrystalline zeolitic materials were selected and further analyzed for the highly selective separation of co-produced water or methanol from the reaction mixture. The determination of adsorption and diffusion parameters for water and methanol inside the microcrystalline zeolitic pores has been made by using a demanding analysis technique based on direct measurements of mass transportation (DMMT) in liquid phase. It was possible to demonstrate that the chemical engineered sorbents, due to their high separation factors, have many inherent advantages, such as higher throughput and product purity as well as considerably high recyclability. The yield of products in both reactions was significantly enhanced when the selected materials and process conditions was applied.

4.1 Optimization of DMC synthesis from methanol and CO₂ using a selective water removal agent

4.1.1 Introduction

The current widely applied industrial processes for dimethyl carbonate (DMC) synthesis are the methanolysis of phosgene ^[1] and the oxidative carbonylation of methanol. ^[2] Both of them involve the use of toxic and / or flammable reagents, *e.g.*, phosgene and CO, making the direct synthesis of DMC from methanol and CO₂ especially attractive.



Scheme 4-1 Chemical equation of DMC formation from methanol and CO₂

As shown in Scheme 4-1, the direct synthesis of DMC from methanol and CO₂, however, is a thermodynamically un-favored reaction (equilibrium constant $K < 10^{-5}$ determined at a temperature range of 160 ~ 180 °C and corresponding to $\Delta_r G_m^\circ > 40$ kJ mol⁻¹), indicating that the maximum DMC yield is lower than 1 %. ^[3, 4] The reaction equilibrium, however, can be significantly shifted by using a suitable water scavenger to minimize the water content in the reaction mixture and to maximize the DMC product formation. It has been previously reported that 2,2-dimethoxypropane (DMP) and *N,N'*-dicyclohexylcarbodiimide (DCC) can be used as a selective chemical water scavenger in this reaction. ^[5] However, the main disadvantage of the chemical water scavenger is the high energy consumption in regeneration of the spent scavenging agent which reacts stoichiometrically with water. In addition, the high expense of large amounts of chemical water scavengers required in an operational unit also limits their industrial application. Therefore, an easy-to-handle water scavenger

with high selectivity, low cost and high reusability is desired for this application. With the above mentioned concerns and in order to overcome the disadvantages of chemical water scavengers, well-ordered crystalline materials have been considered for the selective water removal in a DMC synthesis process.

For that, zeolites, a class of solid state crystalline materials with well-defined pore structure, intra-crystalline channels and cages, were analyzed as potential candidates.^[6-8] In the present specific case, *i.e.*, concerning the selective separation of two small molecules having comparable kinetic diameter (water 2.6 Å and methanol 3.6 Å), zeolites with narrow pores are of special importance. Linde Type A zeolite (LTA or A zeolite) is a typical small-pore zeolite with a well-ordered crystalline structure consisting of unit cells containing 8-, 6- and 4-membered rings (8MR, 6MR and 4MR). The pore opening of 8MR varies with different cation compositions between 3 Å and 5 Å (being only marginally larger than 2.6 Å, the kinetic diameter of water), making it suitable for the selective water removal from organic solutions. LTA zeolite, therefore, has been widely used as dehydration agent in separation processes (*e.g.*, adsorptive solvent drying and methyl acetate purification)^[9, 10] as well as water scavengers to shift thermodynamic equilibria (*e.g.*, germantranes synthesis and polymerization of BPA with CO).^[11, 12] The uptake capacity and the diffusion kinetics are strongly dependent on the water concentration and temperature. In the case of DMC formation from methanol and CO₂, it is especially complicated, since water is required to be selectively removed from a methanol-abundant reaction mixture, so that a competitive adsorption / diffusion system needs to be rigorously controlled. Therefore, adsorption and diffusion properties of water and methanol were accurately analyzed, in order to find a viable technical solution for DMC yield enhancement by using LTA zeolites.

Herein, a detailed temperature-dependent analysis of various well-ordered LTA zeolitic materials was performed in order to ensure a selective water adsorption.

Direct measurements of mass transportation (DMMT) reveal that 3A zeolite, among all, has the highest diffusion coefficient ratios of water and methanol as well as the highest water uptake capacity at low temperature (-25 °C). Based on these experimental results, a new technological design consisting of an operational unit next to a reaction zone was developed. Within this study, it was successfully shown that by using a 3A sorbent operated at low temperature for the selective water removal from the reaction mixture, a 10-fold increase in DMC production can be achieved.

4.1.2 Experimental

4.1.2.1 *Structural and composition analysis*

The crystal structure of LTA zeolites was analyzed by X-ray diffraction measurements. Philips X'Pert Pro diffractometer equipped with an X'celerator module using Cu-K α radiation operating at 40 kV / 45 mA was applied. The samples were measured with a scan rate of 3 °min⁻¹ from 5 ° to 70 °(2 θ).

In order to determine the elemental compositions of K, Na, Ca, Si and Al in LTA zeolites, AAS measurements were conducted. All zeolites were calcined at 450 °C for 4 hours in air flow, for elimination of adsorbed water. Then the samples were analyzed by atomic absorption spectrometer (AAS Unicam Solar 939).

4.1.2.2 *Adsorption isotherms*

3A, 4A and 5A zeolites (pellets) were used for the adsorption isotherm measurements. All zeolites were calcined in a tube furnace in air flow (100 mL min⁻¹) for 4 hours at 450 °C to remove adsorbed water and organic molecules. Before use, the calcined

zeolites were kept in a Schlenk tube in order to prevent further contamination.

For the determination of water adsorption isotherm, isobutanol was selected as an appropriate solvent based on the fact that the kinetic diameter of isobutanol is much larger than the pore opening of any of the considered zeolites. For analysis, in several conical beakers, a series of solution containing water and isobutanol (0.1 ~ 5.0 wt. % water content, each of 25 g) was prepared. The temperature was controlled by a Fisherbrand FBC 740 thermostat, where the glass conical beakers containing liquid solutions were placed inside, and the temperature was set to 25, 0 and -25 °C, respectively. After the solutions were tempered, 5 g of dried zeolite were added to each beaker and the solution was further equilibrated for 48 hours under isothermal conditions. Then, the liquid samples were taken and analyzed by Karl-Fischer titration (Metrohm KF-Coulometer 831). From the residual water in the liquid samples, the amount of adsorbed water was calculated.

In the case of methanol adsorption isotherm, the same approach, as in the case of water, was employed. Liquid solutions of methanol / isobutanol with 0.1 ~ 5.0 wt. % methanol were prepared by using conical glass beakers. Following the addition of the selected zeolitic materials and the equilibration of the solution, gas chromatography (Fisons GC 8160 equipped with a fused silica column Rtx-5AM) was applied for the determination of residual methanol concentration.

In another experiment mimicking the adsorption properties of LTA zeolites in the presence of methanol, a methanol solution containing various amounts of water was used for the determination of water adsorption isotherm in the presence of methanol. In these experiments, a series of water / methanol solutions with 0.1 ~ 5.0 wt. % water content were prepared, and the same procedure described above was applied to determine the adsorption behavior of water in the presence of methanol. From the residual water concentrations in liquid mixtures, the amounts of adsorbed water by

zeolites were calculated. ^[13]

4.1.2.3 Diffusion kinetics

For the analysis of time dependent adsorption of water, 3A, 4A and 5A zeolites (pellets) were used. The pretreatment of zeolites was the same as described in Section 4.1.2.2.

For the measurements of water diffusion kinetics, isobutanol was selected as solvent. A solution of isobutanol with 5 wt. % water was prepared (total weight 25 g) prior to the measurements. The temperature was controlled by a Fisherbrand FBC 740 thermostat, where the glass conical beakers containing liquid solutions were placed inside, and the temperature was set to 25, 0 and -25 °C, respectively. Afterwards, 5 g of dried zeolite were added to each beaker and the kinetic measurements were started under isothermal conditions. During the kinetic measurement, liquid samples with volume of 0.05 mL were collected at short time intervals and analyzed by Karl-Fischer (KF) titration (Metrohm KF-Coulometer 831). The amount of adsorbed water was calculated based on the experimental results obtained following the KF titration. Based on the plot of adsorbed water amount vs. time, important parameters of diffusion kinetics were determined.

For the determination of methanol diffusion kinetics, the same experimental approach was applied. Liquid solution of methanol / isobutanol (5.0 wt. % methanol) was prepared and the time-dependent change of the liquid mixture in the presence of the selected LTA zeolites was finally analyzed by GC (Fisons GC 8160 equipped with a fused silica column Rtx-5AM).

In order to determine the values of mass transportation coefficient, the average size of

secondary zeolitic particles is required. Before measurements, all zeolites were dried and grounded to fine powder and treated in ultrasonic bath for 0.5 hour. Afterwards, the size distribution of all zeolitic materials was measured by laser scattering analyzer (Coulter LS 230).

4.1.2.4 Catalyzed DMC synthesis from methanol and CO_2

For optimizing the process for DMC production, a new process design with high operational flexibility was considered. The schematic representation of the device consisting from a reaction zone and a separation unit is shown in Figure 4-1.

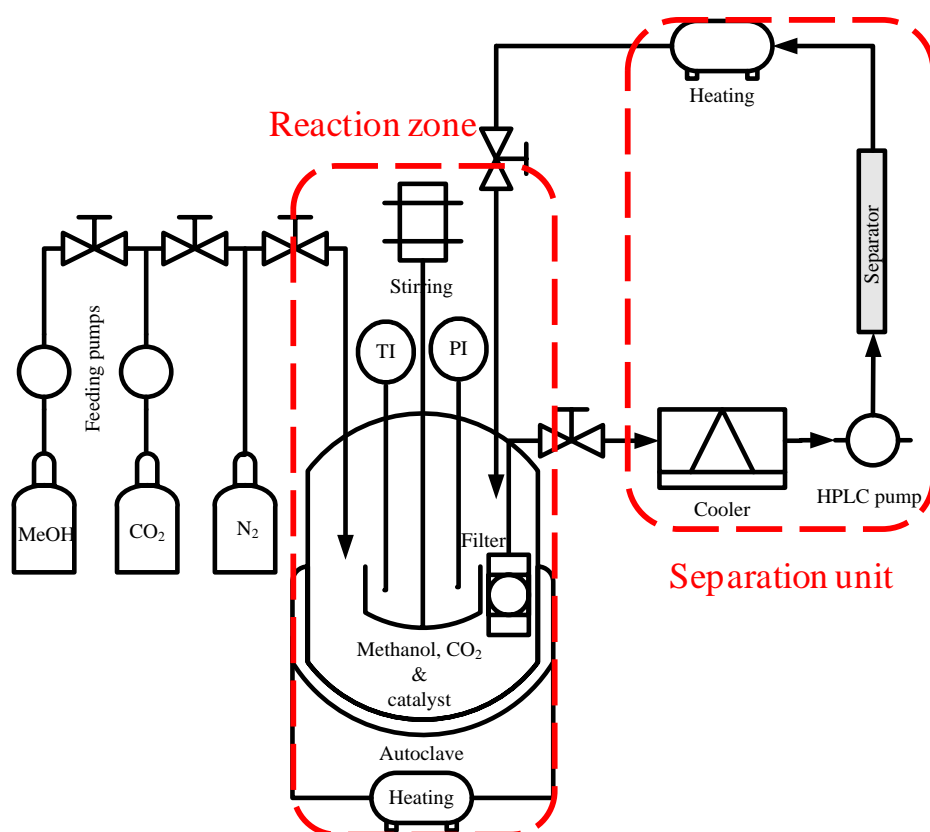


Figure 4-1 Sketch of the reactor and the dehydration unit employed for DMC synthesis

The catalytic reaction was carried out in a 70 mL stainless steel jacketed autoclave

attached to a stainless steel sample cylinder with an inner volume of 50 mL (Swagelok) to ensure constant pressure during the entire reaction duration. The dehydration unit was tempered by circulation of the cold liquid (aqueous solution of ethylene glycol) between the thermostat (Fisherbrand FBC 740) and the jacketed tube. The internal recirculation of the reaction mixture was ensured by an HPLC pump (Gilson 303). This construction allowed outstanding operational flexibility to achieve superior catalytic conversion.

In the catalytic DMC synthesis, ZrO_2 was used as a catalyst. For the preparation of ZrO_2 catalyst, solutions of zirconyl nitrate and ammonium hydroxide were mixed together and the formed hydrous ZrO_2 was aged at room temperature overnight. Afterwards, the resulted gel was washed with bi-distilled water and dried at 110 °C overnight. Finally, obtained sample was calcined at 400 °C for 4 hours in air flow. The method for the catalyst preparation was the same as reported in previous literature.^[14] For the sorbents used in the separation unit, prior to reaction, the zeolitic materials were calcined in a tube furnace in air flow (100 mL min^{-1}) at 450 °C for 4 hours.

For a typical reaction, the dehydration unit was filled with 18 g of dried zeolite sorbent and the temperatures were systematically varied from -25 to 25 °C. Subsequently, 2 g of ZrO_2 catalysts and 39.6 g of methanol were added to the autoclave. The reactor was then sealed and intensively purged with N_2 in order to maintain inert conditions during the catalytic reaction. As soon as the temperature of reaction zone reached 160 °C (monitored by Eurotherm 2132 temperature controller), 10 g of liquid CO_2 were introduced with a flow rate of 5 mL min^{-1} by using a syringe pump (Teledyne Isco, model 500) and the catalytic reaction was started. During the entire reaction course, the mixture was stirred with a rate of 1200 rpm. Before recirculation, the reaction mixture was filtered by using an in-line particulate filter with 0.5 micron element kit (Swagelok SS-2F-K4-05) and cooled to the temperature at which the selective water removal in the dehydration unit is favored (-25 ~ 25 °C).

The composition of the liquid samples was analyzed by Karl-Fischer titration (Metrohm KF-Coulometer 831) and gas chromatograph (Fisons GC 8160 equipped with Rtx-5AM column). The yield of DMC was calculated based on initial amount of CO₂, as shown in Eq. 4-1.

$$\text{DMC Yield (mol. \%)} = \frac{n(\text{DMC})}{n_0(\text{CO}_2)} \times 100\%$$

Eq. 4-1

4.1.3 Results

4.1.3.1 Adsorption isotherms

XRD and AAS analysis were performed to characterize the crystalline phase and chemical composition of the selected solid sorbents, respectively. All the selected LTA zeolites have a well-ordered crystalline structure with different cation composition (details are shown in Section 4.5). As a first attempt to understand the structural requirement on the selective water uptake in methanol abundant solution, the water and methanol adsorption capacities in different LTA zeolites and the adsorption isotherms were determined (with the use of isobutanol as solvent). Noteworthy, methanol and water are quite similar in molecular size, polarity and in many other chemical properties, rendering them difficult to be separated. Detailed water adsorption isotherms in LTA zeolites at low temperature (-25 °C) and at ambient temperature (25 °C) are shown in Figure 4-2.

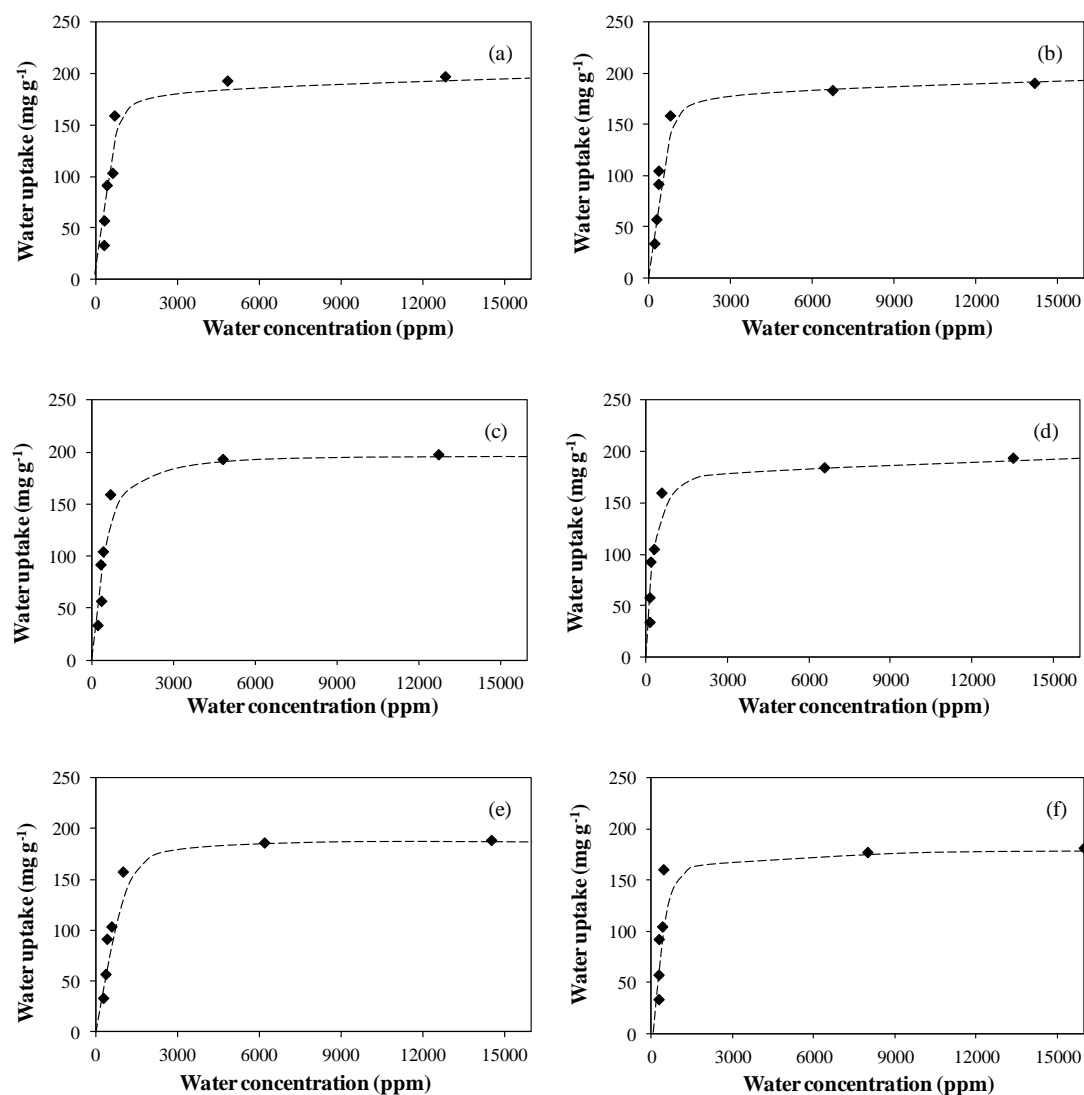


Figure 4-2 Water adsorption isotherms (isobutanol was used as solvent) on LTA zeolites at different temperatures (a: 3A at -25 °C, b: 3A at 25 °C, c: 4A at -25 °C, d: 4A at 25 °C, e: 5A at -25 °C, f: 5A at 25 °C)

Considering the adsorption model, isobutanol was selected as solvent molecule in order to exclude the co-adsorption of solvent and water in the zeolites, thus, the adsorption isotherm was fitted into Langmuir's model, which is normally used for the determination of a single component adsorption. The only difference on experimental conditions between the performed measurements and an ideal Langmuir's model is that the experiments were conducted in liquid phase instead of gas phase which is assumed in Langmuir's model. In this case, the term of partial pressure is substituted by the term of concentration as illustrated in Eq. 4-2 and 4-3.

$$\theta = \frac{[A_{\text{ads}}]}{[S_0]} = \frac{K_{\text{eq}}C}{1 + K_{\text{eq}}C}$$

Eq. 4-2

$$\frac{C}{[A_{\text{ads}}]} = \frac{C}{[S_0]} + \frac{1}{K_{\text{eq}}[S_0]}$$

Eq. 4-3

Here θ represents adsorption coverage, $[A_{\text{ads}}]$ is concentration of adsorbed water, $[S_0]$ stands for the total number of positions (the sum of occupied and available positions). In Eq. 4-2 and 4-3, K_{eq} represents adsorption equilibrium constant in Langmuir's model and C is the concentration of water in liquid phase. Eq. 4-3 was derived from Eq. 4-2 for fitting of experimental data.

Based on Eq. 4-3, the experimental results were fitted by using Langmuir's model ($C/[A_{\text{ads}}]^{-1}$ was plotted against C), as shown in Figure 4-3.

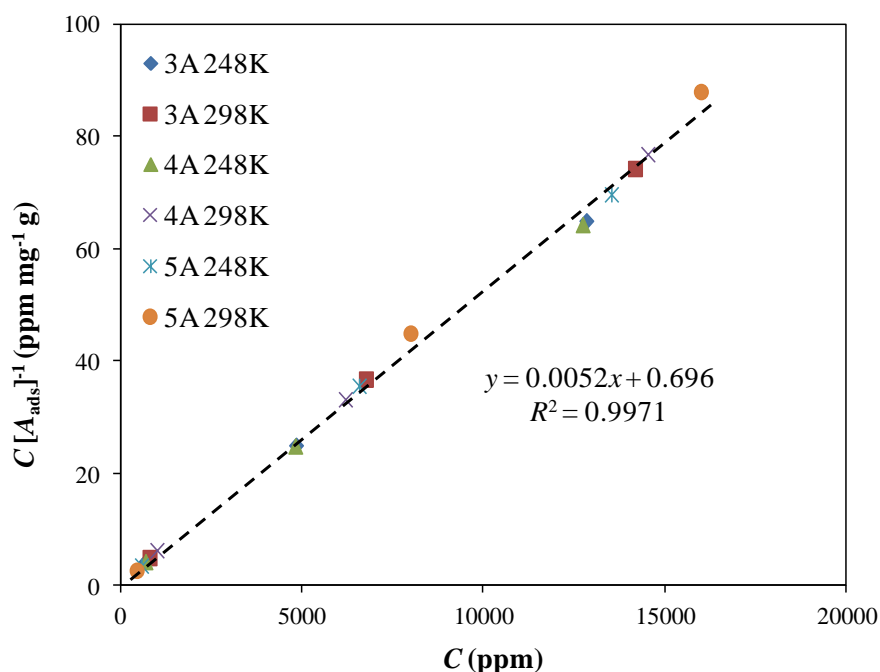


Figure 4-3 Experimental data point fitting of water adsorption isotherms (with the use of isobutanol as solvent) on all LTA zeolites at different temperatures using Langmuir's model

It was shown that water adsorption on all selected LTA zeolites followed the Langmuir's adsorption model, when isobutanol was used as a solvent. Expectedly, all measured adsorption isotherms, independent from zeolites and temperatures, possessed the same adsorption features. This investigation reflected the fact that all LTA zeolites have identical inner volumes for water uptake so that a maximum concentration of water adsorption was determined as *ca.* 200 mg g⁻¹ for all the materials. It is also worth mentioning that other classical adsorption models, *e.g.*, Freundlich's model and Temkin's model, were also attempted to fit the experimental results. However, none of them could describe the experimental data with sufficient accuracy.

Methanol adsorption isotherms and their fittings, according to Langmuir's adsorption model, are shown in Figure 4-4, respectively. All other classical adsorption models failed to describe the experimental results.

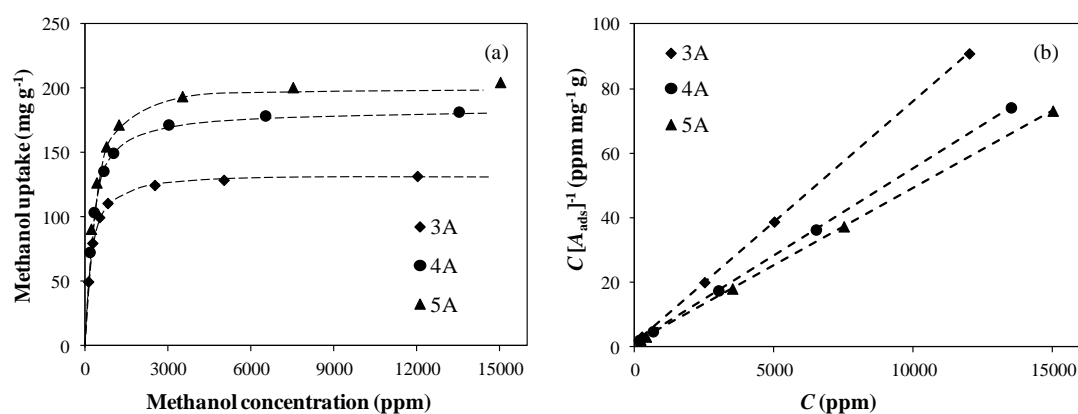


Figure 4-4 Methanol adsorption isotherms (a) and their Langmuir fittings (b) on LTA zeolites at 25 °C (with the use of isobutanol as solvent)

Different from water adsorption in LTA zeolites, the methanol uptake varied with different pore size of the LTA zeolites. Among the selected LTA zeolites, 5A zeolite having the largest mean pore opening had the largest uptake capacity for methanol (208 mg g⁻¹), while the smallest uptake was determined for 3A zeolite (133 mg g⁻¹).

The adsorption of water and methanol on different LTA zeolites was further analyzed to fully understand their unique behaviors towards selective adsorption of water from a methanol abundant solution.

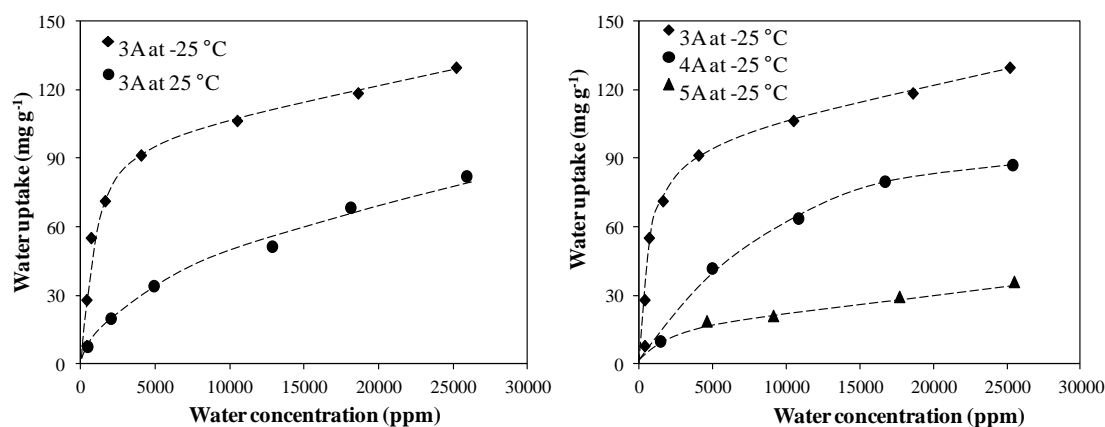


Figure 4-5 Water adsorption isotherms (with the presence of methanol) on 3A zeolite at different temperatures (a) and on different zeolites at -25 °C (b)

As shown in Figure 4-5 (a), under the condition that the water content was *ca.* 2.5 wt. %, significantly higher amounts of water (132 mg g⁻¹) were adsorbed from a methanol abundant solution in 3A zeolite operated at -25 °C than that at 25 °C (80 mg g⁻¹). Similar trends were observed when the water content in the liquid solution was even lower (*ca.* 500 ~ 5000 ppm). 4A and 5A zeolites had a considerably lower selectivity for water at -25 °C (Figure 4-5 (b)), indicating the co-adsorption of methanol.

4.1.3.2 Diffusion kinetics

Time-dependent measurements on water and methanol diffusion in the selected LTA zeolites were conducted at different temperatures. For the determination of important kinetic parameters, the uptake of water or methanol was measured and plotted against

adsorption time. Under the conditions employed for the present study, the adsorption course comprised the inter- and intra-particle diffusion, which included, more specifically, surface diffusion, Knudsen diffusion, bulk diffusion and intra-crystalline diffusion. Among them, the intra-crystalline diffusion has the lowest diffusion coefficient that is, at least 2 ~ 3 orders of magnitude smaller than Knudsen diffusion and bulk diffusion (Figure 1-2). Based on this consideration, the overall diffusion kinetics was simplified to one diffusion step with one single diffusion coefficient (D). In a previous study, a model for diffusion in ideal rectangular particles was proposed (Eq. 4-4).^[15]

$$\ln \frac{[S_0] - [A_{\text{ads}}](t)}{[S_0] - [A_{\text{ads}}](0)} = C_0 - \frac{\pi^2 D t}{4} \cdot \left(\frac{1}{a^2} + \frac{1}{b^2} + \frac{1}{c^2} \right)$$

Eq. 4-4

Here $[S_0]$ represents the maximum uptake of adsorbate, $[A_{\text{ads}}]$ is a function of time (t), representing the time dependent concentration of adsorbed amount of water or methanol, C_0 is a constant depending on the particle shape, D represents the diffusion coefficient, a , b , c represent edges of rectangular parallelepipeds, with $2a$, $2b$, $2c$ in length.

In Eq. 4-4, based on the fact that initial water content of the zeolite is negligible since all the zeolites were calcined at high temperature (450 °C) prior to use, $[A_{\text{ads}}](0)$ was regarded to be equal to 0. Together with the cubic shape of LTA zeolites, the model was adapted as Eq. 4-5.

$$-\ln \left[1 - \frac{[A_{\text{ads}}](t)}{[S_0]} \right] = \frac{3\pi^2 D}{4a^2} \cdot t + C_0$$

Eq. 4-5

Here a represents the edge of a cubic particle with $2a$ in length.

In a rigorous analysis, the diffusion coefficient also depends on the concentration of adsorbate. However, at the beginning of the adsorption course, the concentration of adsorbate is low and, therefore, has little impact on the diffusion coefficient. The diffusion coefficient was calculated from the slope of linear region of the plot $-\ln\left[1 - \frac{[A_{\text{ads}}](t)}{S_0}\right]$ vs. t , where a was determined by the particle size distribution analysis (Table 4-1).

Table 4-1 Average particle size of LTA zeolites

Zeolites	Average particle size (μm)*
3A	2.47
4A	2.30
5A	1.82

* The measured average particle size equals to $2a$ in Eq. 4-5.

In Eq. 4-5, the value of C_0 was not considered in the calculation and could vary with various systematic and random errors. Furthermore, intra-crystalline diffusion in porous crystalline materials obeys Arrhenius plot, as illustrated in Eq. 4-6.

$$\ln D(T) = \ln D_0 - \frac{E_a}{RT}$$

Eq. 4-6

Here $D(T)$ is the diffusion coefficient which depends on temperature, D_0 represents the pre-exponential constant, E_a is the diffusion activation energy, R represents the ideal gas constant and T is the absolute temperature.

The calculated diffusion coefficients of water and methanol on different LTA zeolites at different temperatures and corresponding activation energy values are listed in Table 4-2 and 4-3.

Table 4-2 Water diffusion kinetic parameters in LTA zeolites

Zeolites	E_a (kJ mol ⁻¹)	Diffusion coefficient of water (10 ⁻¹⁴ cm ² s ⁻¹)		
		-25 °C	0 °C	25 °C
3A	29.2	2.37	9.35	25.3
4A	30.6	2.95	13.2	35.3
5A	25.6	3.46	9.21	27.1

Table 4-3 Methanol diffusion kinetic parameters in LTA zeolites

Zeolites	E_a (kJ mol ⁻¹)	Diffusion coefficient of methanol (10 ⁻¹⁴ cm ² s ⁻¹)		
		-25 °C	0 °C	25 °C
3A	91.6	0.02*	0.12	6.98
4A	62.6	0.17*	0.89	14.3
5A	53.5	0.22	2.19	17.1

* At -25 °C, the amount of methanol uptake on both 3A and 4A zeolites is very small. Compared to total adsorption, the adsorption of methanol on the outer surface of the LTA zeolites cannot be neglected. In contrast to that, methanol adsorption on 5A zeolite and water adsorption on all LTA zeolites is negligibly small. The diffusion coefficient D was determined over a temperature range, at which the diffusion mechanism is identical. The temperature dependent variation of the pore size might induce a change in the diffusion mechanism for 3A and 4A zeolites. Therefore, these values for diffusion coefficient obtained at -25 °C on 3A and 4A zeolites are not considered in the determination of diffusion activation energies.

It is observed that the temperature has a greater impact on the methanol diffusion as compared to water, leading to higher diffusion activation energy of methanol than in the case of water.

Table 4-4 Ratio between diffusion coefficients of water and methanol

Zeolites	$D_{\text{water}} / D_{\text{methanol}}$		
	-25 °C	0 °C	25 °C
3A	119	77	3.6
4A	17	15	2.5
5A	15	4.2	1.6

From results listed in Table 4-2 and 4-3, a direct comparison between diffusion coefficient of water and methanol was made, and the ratios of D (water) to D (methanol) were calculated (Table 4-4). The ratio of D (water) to D (methanol) indicates the ability of selective water adsorption from a methanol abundant mixture. In this context, the 3A zeolite operated at low temperature displayed the highest selectivity on water diffusion than any other selected zeolites as well as itself operated at higher temperatures.

In order to have direct evidence on the selectivity of water adsorption under selected operational conditions, the co-adsorption of water and methanol on zeolites was studied in detail (Figure 4-6).

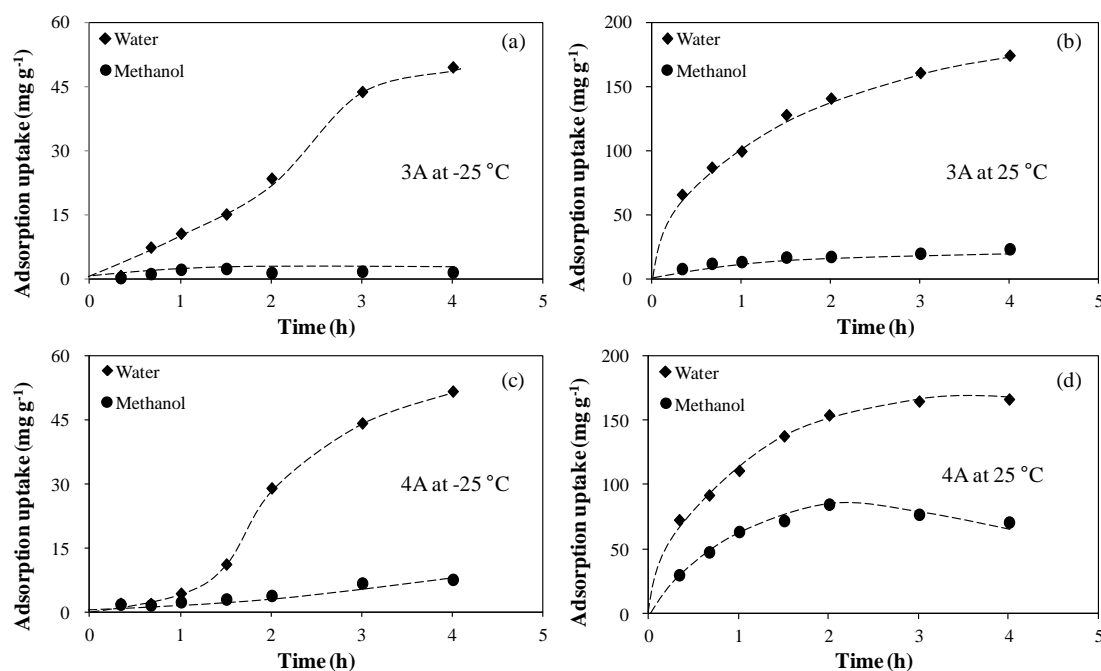


Figure 4-6 Co-adsorption of water and methanol (with the use of isobutanol as solvent) on LTA zeolites at different temperatures (a: 3A at -25 °C, b: 3A at 25 °C, c: 4A -25 °C, d: 4A 25 °C)

Experimental results indicate that water uptake increase was faster than the increase in methanol uptake. 3A zeolite operated at low temperature (-25 °C) showed the highest selectivity on water diffusion and displayed the best competence on selective adsorption of water, among all tested zeolites and operational conditions. In the case of the co-adsorption on 4A zeolite at ambient temperature, the uptake of both water and methanol increased fast in quantity at the beginning followed by decrease of methanol uptake and continuous increase of water uptake owing to higher polarity of water molecule compared to that of methanol. Similar phenomena were observed in the case of benzene and *n*-paraffin co-adsorption on NaX zeolite. ^[16]

4.1.3.3 Catalyzed DMC synthesis from methanol and CO₂

ZrO₂-catalyzed DMC synthesis from methanol and CO₂ was performed by using LTA zeolites as heterogeneous sorbents to reduce the thermodynamic constraints of the reaction. To improve the overall DMC formation, two comparative studies were

conducted, *i.e.*, 1) different crystalline LTA zeolites were used at same operational temperature in order to identify the most adequate solid sorbent for the process and, 2) the most efficient zeolite was further studied at different temperatures to maximize the adsorption / diffusion performance of the material. The yield-time profiles of DMC obtained under different experimental conditions are shown in Figure 4-7.

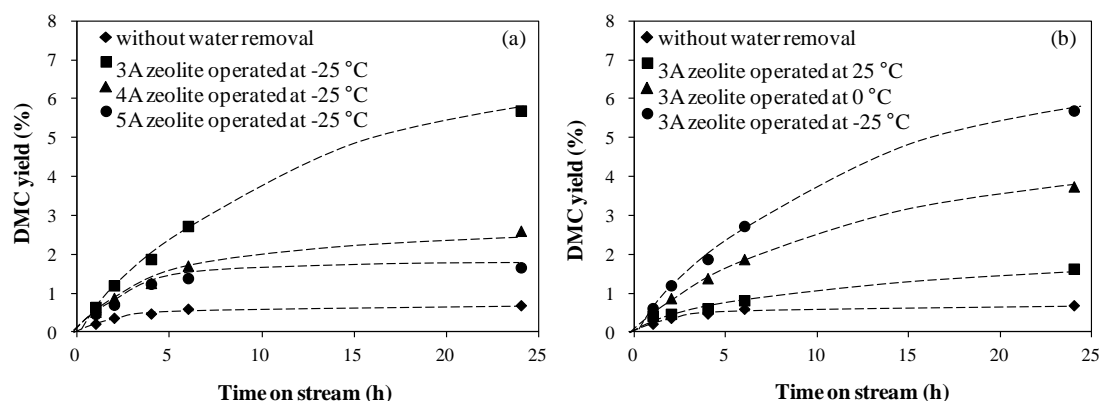


Figure 4-7 DMC formation in the presence of different LTA zeolites operated at -25 °C (a) and in the presence of 3A zeolite operated at different temperatures (b) (Reaction conditions: zeolites 18 g in separation zone, ZrO₂ catalyst 2.0 g, CO₂ 10 g, methanol 39.6 g, total pressure 42 bar, temperature of reaction zone 160 °C, liquid mixture circulation rate 2.0 mL min⁻¹.)

DMC synthesis from methanol and CO₂ is a thermodynamically limited reaction and the DMC yield in the absence of a water scavenger is lower than 1 % at 160 °C (Figure 4-7 (a) and (b)). Among all the tested LTA zeolites, 3A zeolite showed the best ability in shifting the thermodynamic equilibrium. In addition, lowering the operation temperature of the dehydration agent favored the DMC production, owing to the enhanced uptake capacity and water diffusion selectivity of 3A zeolite at lower operational temperatures. The highest DMC yield was achieved when 3A zeolite was operated at -25 °C. Under this condition, by using a 3A sorbent for the selective water removal from the reaction mixture, a 10-fold increase in DMC production was achieved.

4.1.4 Discussion

ZrO₂-catalyzed DMC synthesis is a thermodynamically constrained reaction. The maximal attainable extent of the reaction is pointed out by the corresponding equilibrium constant (K) of the reaction. A comparison between theoretical (calculated based on the data available in NIST Chemistry Web Book and literatures [17, 18]) and experimentally determined equilibrium constants is shown in Table 4-5.

Table 4-5 Theoretical and experimental determined equilibrium constants

Temperature (°C)	Experimental determined K	Theoretical determined K
140	8.8×10^{-6}	9.0×10^{-6}
160	7.1×10^{-6}	7.6×10^{-6}
180	6.1×10^{-6}	6.5×10^{-6}

Both theoretical and experimental values of equilibrium constants indicate that the equilibrium limitation in this reaction is very strong. From the aspect of industrial feasibility, an economic and facile strategy is required to shift the chemical equilibrium and to favor the formation of desired DMC.

Crystalline LTA zeolite was synthesized in its sodium form having chemical formula of Na₁₂Al₁₂Si₁₂O₄₈. All LTA zeolites share the same structural topology and the only difference among 3A, 4A and 5A is in their cations content compensating the overall electrons resulting in different pore openings (Section 4.5). Precisely because of it, these materials show huge differences on the adsorption properties, especially when water removal from low molecular weight alcohols was considered. In former times, various attempts were already made in previous contributions on the evaluation of the impact of different cations on the adsorption capacities of LTA zeolites. [19, 20] However, a convincing evidence of a shape selective material with high performance

is still missing.

The water uptake capacity from isobutanol solutions of different LTA zeolitic sorbents was nearly identical at the studied temperatures (Figure 4-2 and 4-3). However, under these conditions, the presence of large excess of methanol will strongly hinder the adsorption of small amounts of water in the zeolitic cages. Thus, the only conceptual possibility to selectively adsorb water is to block the access of methanol using shape selective properties of narrow pore zeolites.

In the crystalline LTA zeolitic framework, some of the cations are located at the pore opening (8MR), directly influencing the molecular diffusion. In order to study the molecular transportation in zeolitic materials, several advanced technologies have been utilized, *e.g.*, pulsed-field gradient nuclear magnetic resonance (PFG-NMR),^[21] neutron scattering,^[22] zero-length column,^[23] Fourier transformed infrared spectroscopy (FT-IR)^[24] and frequency response technology (FR).^[25] However, there is no approach able to provide a straightforward description of diffusion process, except direct measurement of mass transportation (DMMT). DMMT allows an accurate evaluation of thermodynamic and kinetic parameters on molecular diffusion in porous materials, especially in the case of small diffusivity and small crystal particle size (between 1 and 10 μm).^[15]

Considering the competitive adsorption of water and methanol, water uptake in the presence of methanol in LTA zeolites (maximum 130 mg g^{-1} , Figure 4-5) is much lower than the water uptake when solely isobutanol was used as a solvent (*ca.* 200 mg g^{-1} , Figure 4-2). Since the available positions for water uptake are identical in all the LTA zeolites, the lower water uptake in the presence of methanol is due to the competitive adsorption of methanol inside the zeolitic cages. The direct comparison of the uptake capacity in different LTA zeolites at different temperatures (Figure 4-5) evidenced that 3A zeolite, having the smallest mean size of pore opening compared to

the others, has the highest shape selectivity for water removal with the aspect of water uptake capacity.

At ambient temperatures, the flexibility of the zeolitic crystal lattice and the energy of molecular diffusion do not allow a selective adsorption of water from a methanol abundant mixture due to the marginal difference in the kinetic diameter of the two molecules. The competitive diffusion of water and methanol via the 8MR of LTA zeolites at ambient temperature leads to a modest improvement on the DMC production. However, lowering the operational temperature of the molecular diffusion in LTA zeolites to $-25\text{ }^{\circ}\text{C}$ will lower the flexibility of the crystalline lattice and considerably increase the shape selectivity of the zeolite. The smaller the mean pore opening of the zeolite is, the higher the shape selective water removal will be and, consequently, more DMC is yielded (Figure 4-7 (a)). At low conversion, the ZrO_2 catalyzed DMC synthesis from methanol and CO_2 is kinetically controlled. As soon as the reaction approaches to the region that water needs to be removed from the reaction mixture, the overall rate of DMC formation is limited by the competitive uptake kinetics of water and methanol in the separation zone (Figure 4-7 (a) and (b)).

Overall, using a 3A zeolitic scavenger in a separation unit operated at $-25\text{ }^{\circ}\text{C}$ for the selective removal of formed water is an economical and facile strategy to enhance the yield of DMC.

4.1.5 Conclusion

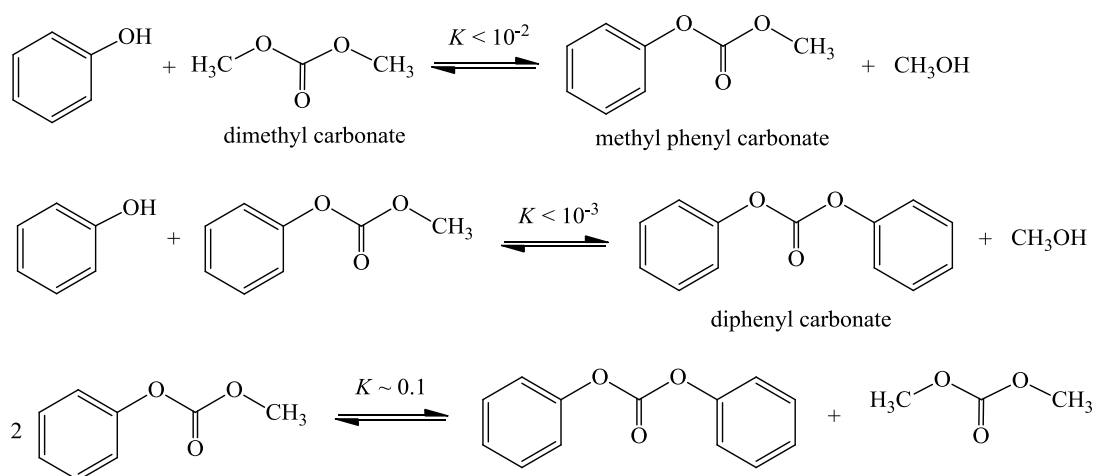
Selective water removal on solid zeolitic sorbents during the ZrO_2 -catalyzed DMC synthesis from methanol and CO_2 is a highly efficient approach to considerably increase the DMC yield. In a comparative study, various LTA zeolites were selected and tested for the selective dehydration of a methanol abundant solution at various operational temperatures. It was shown, that at ambient temperature, due to the high

flexibility of the zeolitic lattice, methanol adsorption / diffusion are similarly favored, lowering the water uptake capacity and the shape selectivity of the zeolite. However, operated at low temperature, 3A zeolite had the lowest methanol uptake capacity and the strongest hindrance of methanol diffusion. This temperature dependent shape selectivity of 3A zeolite makes it an outstanding candidate for the selective water removal agent to be used in a dehydration unit. By using a new technical design consisting of a reaction zone and an external separation unit, a 10-fold increase of the DMC production was achieved.

4.2 Reaction optimization of DPC synthesis from phenol and DMC by *in-situ* methanol removal

4.2.1 Introduction

In order to produce DPC without the use of phosgene, a two-step transesterification reaction from DMC and phenol is proposed. In the 1st step, DMC reacts with phenol to form methyl phenyl carbonate (MPC), while in the 2nd step, the transesterification of MPC with phenol or the disproportionation of MPC takes place (Scheme 4-2).



Scheme 4-2 Reaction network of DPC synthesis from DMC and phenol

Similar as in the case of DMC synthesis from methanol and CO₂, the complete reaction network that counts for the DPC synthesis from phenol and DMC consists of equilibrium-constrained reactions ($K_{eq} < 10^{-5}$). Considering MPC as the main intermediate compound in DPC synthesis, based on combined theoretical and experimental studies, an accurate thermodynamic analysis of each reaction step is given. ^[26] It is stated that the co-produced methanol minimizes the formation of MPC and DPC. In addition, the conversion of MPC to DPC is considerably enhanced if methanol is removed from the reaction system. Therefore, the 1st step transesterification towards MPC represents the major limitation in the two-step DPC synthesis and the methanol concentration needs to be reduced over the entire reaction course.

In order to overcome the thermodynamic constrains, separated reaction zones for different reaction steps involving methanol removal were previously considered. ^[27] A continuous process based on reactive distillation was developed and scaled-up for the titanium phenoxide catalyzed DPC synthesis from phenol and DMC. In this process, three successive reaction zones were designed in order to tune the reaction conditions aiming the maximization of the product yield. In the first two reaction zones, MPC formation via the transesterification is enabled. The vapors from the first two reaction zones were separated by distillation. The DPC formation was achieved in the third reaction zone. However, the complexity within this process design motivates to the development of a new technology, which allows an easier energy-efficient operation. The use of high-performance *in-situ* methanol scavengers is a promising method to reduce thermodynamic constrains and to enhance the product formation. With the concerns of reaction engineering and process technology, an ideal solid state methanol scavenger is expected to meet following requirements, 1) high methanol uptake capacity, 2) high rate of methanol diffusion and, 3) high chemical inertness and thermal stability under reaction conditions. The fundamental knowledge gained on the

study of selective water removal sorbents was used for the design of a high-performance material for methanol removal from the reaction mixture. The kinetic diameter of methanol is 3.6 Å, while the kinetic diameter of phenol is 6.6 Å, which is much larger than methanol and even larger than the pore opening of all commercial available LTA zeolites (5A zeolite is with the pore opening of 5 Å).^[28] Due to the shape selectivity of the crystalline zeolites, the diffusion of phenol inside the crystalline structure of LTA zeolites is hindered and, therefore, can be used for the efficient methanol separation.

In this section, high temperature DMMT was applied for the determination of methanol diffusion parameters and for the analysis of chemical inertness of different zeolitic sorbents. Finally, significant yield enhancement on transesterification of DMC with phenol is achieved with the use of 4A zeolite at high temperature (180 °C) without the use of an external separation unit.

4.2.2 Experimental

4.2.2.1 *Direct measurements of mass transportation at high temperature*

3A, 4A and 5A zeolites were selected for high-temperature diffusion kinetic measurements. All zeolites were calcined in tube furnace with air flow at 450 °C for 4 hours to remove adsorbed water and organic molecules. Before use, the calcined zeolites were kept in a Schlenk tube in order to prevent further contamination from atmosphere.

The high-temperature DMMT was conducted when 5 g of sorbent were introduced in a 70 mL autoclave and isobutanol was used as solvent and internal standard. Subsequently, the reactor was purged with N₂ at 1 MPa till inert conditions were

reached. When the temperature in the autoclave reached 160 °C, the magnetic stirring was started and 25 g of methanol / isobutanol mixture containing 5 wt. % methanol were introduced into the autoclave at a flow rate of 20 mL min⁻¹ by using a syringe pump. During the adsorption process, samples were taken at short time intervals and analyzed by GC. Based on the remaining methanol concentrations in liquid mixtures, the amounts of methanol adsorbed by the zeolites were estimated. Based on the DMMT results, the adsorption isotherms and diffusion kinetics were determined.

4.2.2.2 Catalytic reaction

The transesterification of DMC with phenol was carried out in a stainless steel autoclave (Parr instrument) with an inner volume of 300 mL. In a typical reaction procedure, 0.5 g of MoO₃/SiO₂ solid catalyst (20 wt. % loading of MoO₃ synthesized as described in Section 3.2.1.2), 20 g of zeolitic sorbents together with phenol and DMC were added in the autoclave (total volume of reactants was below 200 mL). The autoclave was then sealed and purged with N₂ several times. After the temperature in the autoclave reached the reaction temperature (160 ~ 180 °C), rigorous stirring was started with a rate of 700 rpm. During the catalytic reaction, the temperature and stirring speed were monitored and controlled by a reactor controller (Parr 4848). The final composition of reaction mixture was determined by GC, and yield of each product was calculated based on the starting amount of phenol.

4.2.2.3 Characterization of zeolitic sorbents

The methods used for the characterization of crystallinity and chemical composition are the same as described in Section 4.1 (results are available in Section 4.5, Figure 4-15 and Table 4-8).

The nature and concentration of surface acidic sites was analyzed by temperature programmed desorption (TPD) and NH_3 was used as a probe molecule. The measurements were performed by using a 6-fold parallel reactor system. For TPD experiments, 50 ~ 100 mg of samples were pretreated at 500 °C (5 °C min^{-1} ramp) in He stream for 1 hour in order to remove surface contaminants. After cooling at 100 °C, ammonia was adsorbed with a partial pressure of 1 mbar. Subsequently, the samples were purged with 30 mL min^{-1} He for 2 hours in order to remove all physisorbed molecules. Then 6 samples were sequentially heated from 100 to 770 °C with an increment of 10 °C min^{-1} to desorb NH_3 . For analysis of the surface bonded species, an attached mass spectrometer (Balzers QME 200) was used. The amount of desorbed NH_3 was determined by the integration of the MS signal calibrated to a standard material (H-ZSM-5 zeolite, Si / Al = 45, number of acidic sites $360\text{ }\mu\text{mol g}^{-1}$).

4.2.3 Results

The methanol adsorption isotherms on LTA zeolites at high temperature (160 °C) are shown in Figure 4-8.

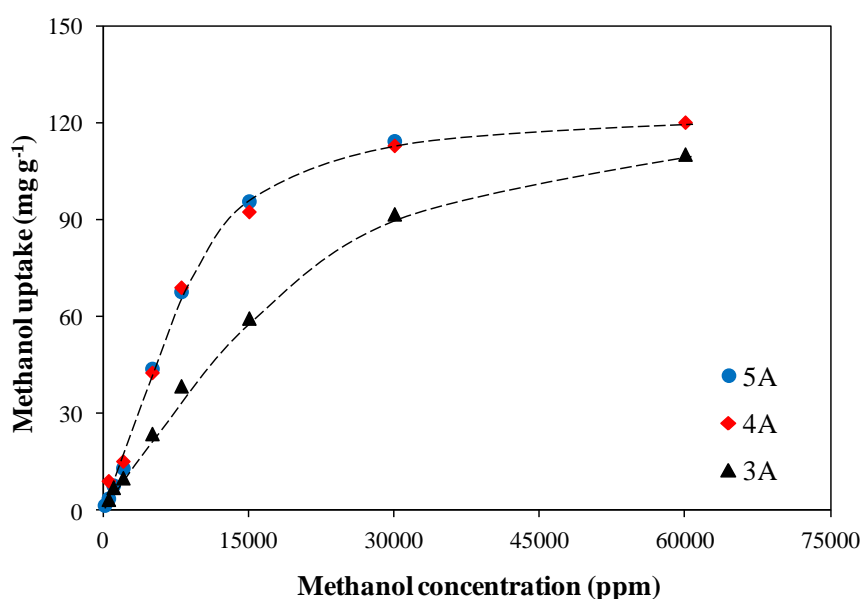


Figure 4-8 Methanol adsorption isotherms on LTA zeolites at 160 °C

It was successfully shown that the methanol adsorption isotherms for 4A and 5A zeolites are similar to each other, indicating that the pore openings of LTA zeolites up to 4 Å are large enough to enable efficient methanol diffusion and larger pore opening does not have any further advantages on it. In addition, the maximum uptake of *ca.* 120 mg g⁻¹, which is slightly lower than the value determined at temperatures lower than the ambient temperature (Section 4.1). The observed lower overall methanol uptake can be explained by Le Châtelier's principle, as methanol adsorption on LTA zeolites is an exothermic process. Compared to 4A and 5A zeolites, 3A zeolite showed a lower methanol uptake in each of measurement, especially at low concentration range of methanol (< 25000 ppm).

Since methanol is the only possible molecule in the reaction mixture that can diffuse into the pores of LTA zeolites, the methanol diffusion kinetics of different LTA zeolites was studied for 3A, 4A and 5A zeolites (Figure 4-9).

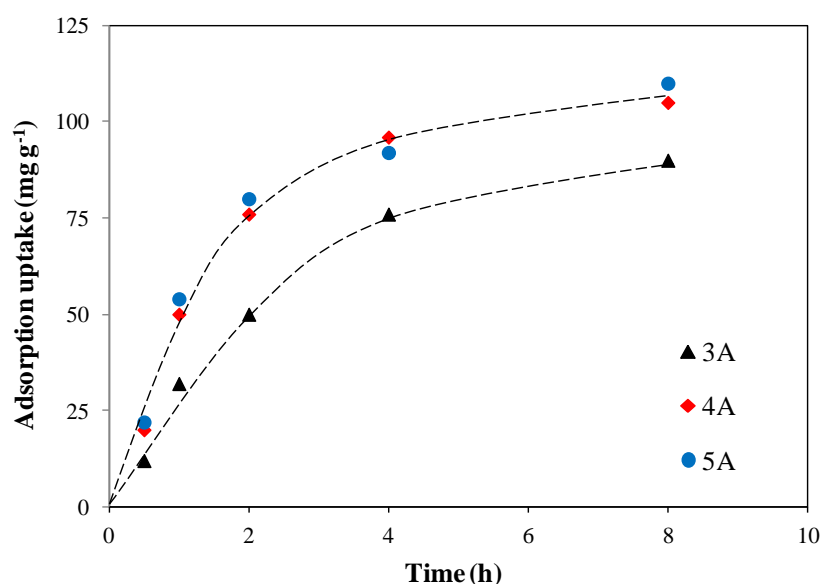


Figure 4-9 Diffusion kinetics of methanol on LTA zeolites (Conditions: reactor volume 70 mL, sorbent 5.0 g, methanol / isobutanol 25.0 g, initial concentration of methanol 5 %, $T = 160$ °C.)

It is clearly evidenced that 4A and 5A zeolites showed comparable diffusion rate (*ca.*

51 mg g⁻¹ h⁻¹ at the initial stage) while the diffusion rate of 3A zeolite was considerably slower (*ca.* 26 mg g⁻¹ h⁻¹ at the beginning).

The transesterification reaction from phenol and DMC was catalyzed by 20 wt. % MoO₃/SiO₂ catalyst. The excellent catalytic performance of MoO₃/SiO₂ was already shown and discussed (Chapter 3). In order to enhance the yield of transesterification products (MPC and DPC), the zeolitic sorbents were loaded concomitantly with the catalysts and reactants and the whole system was operated at high temperature (160 °C). The results are listed in Table 4-6.

Table 4-6 Yield enhancement of transesterification by methanol removal (160 °C)

Condition	Conversion (%)	Yield (%)			
		MPC	DPC	Anisole	Others
Without methanol removal	15.4	13.2	0.2	trace	trace
Methanol removal by 3A zeolite	24.9	24.6	0.3	trace	trace
Methanol removal by 4A zeolite	38.0	37.5	0.4	trace	trace
Methanol removal by 5A zeolite	38.7	38.1	0.3	0.2	trace

Conditions: DMC / phenol = 5, $T = 160$ °C, 20 wt. % MoO₃/SiO₂ 0.5 g, zeolite 20 g (if used), reaction time 6 hours, conversion and yield were calculated on phenol basis.

From the data presented in Table 4-6, it is evidenced that at least 52 % higher phenol conversion was realized in the presence of LTA zeolites. Among all the LTA zeolites, 4A and 5A zeolites showed an increased methanol uptake capability compared to 3A zeolite and had an even higher impact (60 % increase in phenol conversion compared to 3A zeolite). This observation is in good agreement with the adsorption isotherms and diffusion kinetics (Figure 4-8 and 4-9), demonstrating that the continuous methanol removal has a direct influence on the overall product yield. In addition, the transesterification selectivity is high, so that anisole, the main by-product formed via

alkylation of phenol and DMC or decarboxylation of MPC, and other compounds (mainly cresol isomers), are formed with very small percentages. Since $\text{MoO}_3/\text{SiO}_2$ catalyst is a selective catalyst for transesterification at 160 °C, as described in Chapter 3, the use of methanol scavengers did not influence the by-products formation, suggesting that all LTA zeolites have an outstanding chemical inertness under the reaction conditions. In order to further investigate the impact of critical parameters of the reaction system, the same reaction was operated at higher temperature (Table 4-7).

Table 4-7 Yield enhancement of transesterification by methanol removal (180 °C)

Condition	Conversion (%)	Yield (%)			
		MPC	DPC	Anisole	Others
Without methanol removal	18.4	17.3	0.9	0.2	trace
Methanol removal by 3A zeolite	32.5	30.4	1.5	0.6	trace
Methanol removal by 4A zeolite	53.4	48.9	3.3	1.1	trace
Methanol removal by 5A zeolite	53.6	45.7	2.9	1.5	~ 3

Conditions: DMC / phenol = 5, $T = 180$ °C, 20 wt. % $\text{MoO}_3/\text{SiO}_2$ 0.5 g, zeolite 20 g (if used), reaction time 6 hours, conversion and yield were calculated on phenol basis.

When the system was operated at 180 °C, the yield of each product was higher than that obtained at 160 °C, and the conversion of phenol was very close to the equilibrium level (*ca.* 18 %, as estimated from Figure 1-1). At higher temperature, it is not surprising that 4A and 5A zeolites led to comparable phenol conversion which was much higher than that obtained in the presence of 3A zeolite. However, it is also observed that the formation of by-products became even more favorable at 180 °C, compared to the results obtained at 160 °C. Especially the use of 5A zeolite resulted in the formation of considerable amount of alkylation / decarboxylation products (with the selectivity of *ca.* 8 %), reducing the final yield of MPC and DPC. The formation of by-products can be attributed to the thermally favored secondary

reactions, since the catalytic reaction without any methanol removal similarly gave an increased yield of anisole compared to 160 °C. The transesterification selectivity with the use of 3A and 4A zeolites was *ca.* 98 %, which is very close to the observed selectivity for the reaction performed in the absence of a sorbent (~ 99 %). When 5A zeolite was operated at 180 °C, the selectivity of the transesterification products (MPC and DPC) was *ca.* 90 %. In order to investigate the influence of the sorbents on by-product formation, the acidity of different LTA zeolites was determined by NH₃-TPD (Figure 4-10).

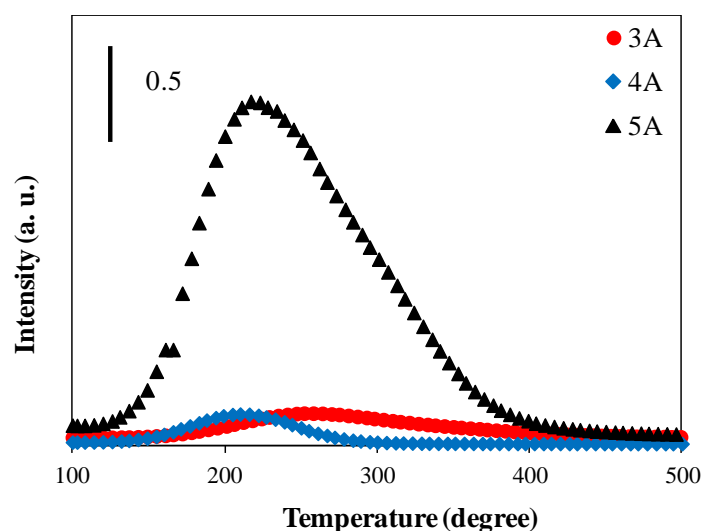


Figure 4-10 NH₃-TPD profiles of LTA zeolites

As shown in NH₃-TPD profiles, 5A zeolite presents distinct surface acidity, while the acidity of 3A and 4A zeolites is negligible. The concentration of surface acidity on 5A zeolite was determined as 285 $\mu\text{mol g}^{-1}$. These surface acidic sites might promote the acid catalyzed anisole and cresol formation.

4.2.4 Discussion

In the aspects of methanol uptake and diffusion rate, 4A and 5A zeolites showed higher performance compared to 3A zeolite (and the performances of 4A and 5A

zeolites are comparable). The lack of adsorption capacity as well as diffusion rate of 3A zeolite is attributed to its smaller mean pore opening (smaller than the kinetic diameter of methanol molecule) hindering the methanol diffusion, as discussed in Section 4.1.4.

With the respect of chemical inertness, 3A and 4A did not contribute to by-product formation, while 5A led to distinct undesired alkylation products. LTA zeolites are normally first produced in Na-form (4A zeolite), followed by cation exchange in order to tailor the size of pore opening (partial K^+ and Ca^{2+} exchange of Na^+ towards 3A and 5A zeolites, respectively). With the presence of crystalline water, Ca^{2+} leads to the generation of $Ca(OH)^+$ together with proton at the intersection of two cages in the LTA framework.^[29] The observed acidity of 5A is responsible for the decomposition of DMC, forming methanol and dimethyl ether (DME), which further undergo alkylation with phenol resulting in anisole formation.^[30] In contrast, similar transformation does not take place when LTA zeolites have only mono-valence cations, reflected by the chemical inertness of 3A and 4A zeolites.

Not as in the case of DMC synthesis, where a competitive complex transportation of water and methanol is involved, the DPC synthesis with methanol removal displayed a much simpler model for the methanol diffusion, allowing the efficient product separation without the use of an external separation unit. From industrial points of view, the *in-situ* methanol scavenger reduces huge energy consumption, as no temperature gradient exists in the reaction system so that extra controlling of different temperatures in different reactor parts (for DMC synthesis, the temperature gradient is 185 °C) is not necessary.

4.2.5 Conclusion

Methanol can be successfully removed under the experimental condition where transesterification of DMC with phenol takes place, leading to an increased MPC / DPC formation. Among all tested zeolites, 4A zeolite is the most suitable candidate for its excellent methanol uptake capacity and high diffusion rate as well as for its chemical inertness. The performance of 3A zeolite is low, due to its narrow pore openings hindering methanol diffusion, while 5A shows a low chemical inertness and enhances secondary undesired reaction paths, due to the presence of additional Lewis acidic sites. From the consideration of process design, the use of methanol scavenger provides the possibility of reducing the number of reaction zones, compared to the traditional MPC process with two reaction zones.

4.3 Further development on process technology

4.3.1 Zeolitic sorbent for *in-situ* water removal

In the process of DMC synthesis from methanol and CO₂, an external separation unit filled with LTA zeolites for water removal is designed, as presented in Section 4.1. However, the high demand on energy consumption for the recycling and temperature adjustment limited its industrial feasibility. Hence, it is highly desired to develop new sorbents that can selectively remove water from methanol-abundant reaction mixture at high temperatures (ideally the same temperature as that of the catalytic reaction). Nonetheless, all commercial available LTA zeolites failed on this issue. As an example, the diffusion kinetics of water and methanol in commercial available 4A and 3A zeolite are comparatively shown in Figure 4-11.

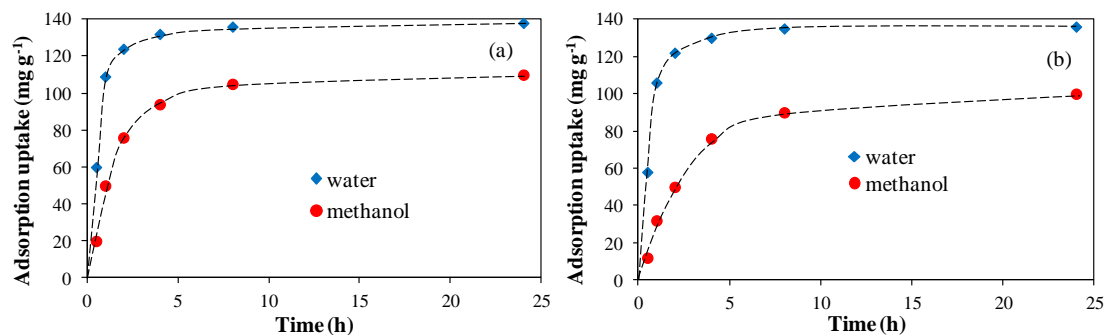


Figure 4-11 Diffusion kinetics of water and methanol on 4A (a) and 3A (b) zeolites (Conditions: reactor volume 70 mL, sorbent 5.0 g, methanol / isobutanol (or water / isobutanol) 25.0 g, initial concentration of methanol (or water) 5 %, $T = 160$ °C.)

Besides the crystalline network of the zeolitic framework, it was revealed that the location of different cations has a crucial effect on the size of zeolite pore opening. With this respect, recently, new chemical modification has been made on commercial available zeolites. The resulted materials have high separation selectivity for water compared to methanol at 160 °C. ^[31] Under the same conditions of high-temperature DMMT measurements in Section 4.2, the diffusion kinetics of water and methanol is comparatively shown in Figure 4-12.

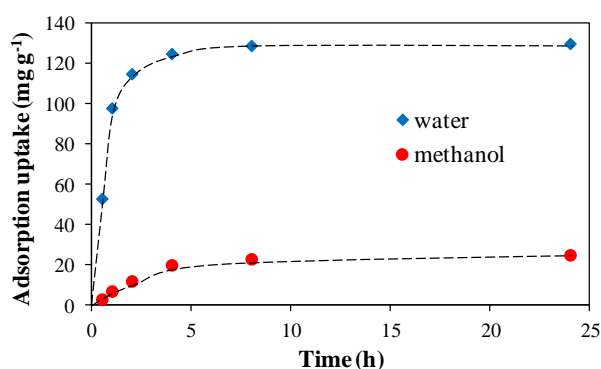


Figure 4-12 Diffusion kinetics of water and methanol on new zeolitic sorbent (Conditions: reactor volume 70 mL, sorbent 5.0 g, methanol / isobutanol (or water / isobutanol) 25.0 g, initial concentration of methanol (or water) 5 %, $T = 160$ °C.)

In the catalytic reaction, when zeolitic sorbents were suspended together with reactants and catalysts (at 160 °C), 3A zeolite was not able to enhance the yield of DMC. In contrast, the newly developed zeolitic sorbent significantly improved the

DMC yield by one order of magnitude as shown in Figure 4-13.

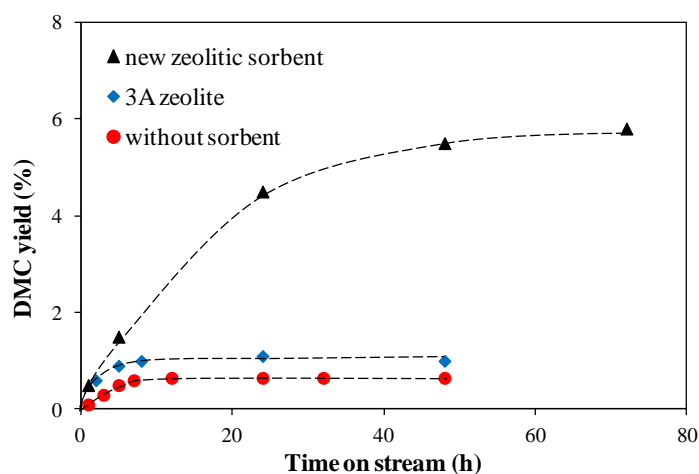


Figure 4-13 DMC yield enhancement with the use of zeolitic sorbents (Conditions: 39.6 g methanol, 10 g CO₂, 18 g zeolitic sorbent (if used), 2.0 g ZrO₂ used as catalyst, $T = 160$ °C for both catalytic reaction and operation of sorbents.)

In sum, it was shown that the newly developed zeolitic sorbents successfully fulfill the requirements for an industrial application, *i.e.*, 1) high selectivity, 2) high reusability, 3) high temperature operational stability. Therefore, the new zeolitic sorbents can be similarly applied as dehydration agents in various separation processes (*e.g.*, removing trace amounts of water present in organic solvents), demonstrating the overall importance of the new engineering material for the sustainable process design. Furthermore, the new zeolitic sorbents could also be used as a main component for the membrane preparation in order to achieve energy-saving continuous operation under a broad range of operational conditions.

4.3.2 Zeolitic membrane for high-performance water / methanol separation

As proposed after the development of new zeolitic sorbents with excellent performance on water / methanol separation (Section 4.3.1), a new zeolitic membrane based on the transportation features of basic operation units in the zeolitic sorbent is

further developed. ^[32] The separation factor of water to methanol is higher than 1000 at 160 °C with the water permeance in an industrial feasible range (*ca.* 10^{-6} mol m⁻² s⁻¹ Pa⁻¹). ^[33] As a benchmark for comparison, a commercial available LTA zeolitic membrane is only able to separate methanol and water with the factor < 10 under the same condition. ^[34] Compared to the new zeolitic sorbents presented in Section 4.3.1, the present zeolitic membrane not only possesses all the advantages of the sorbents, but also provides the advantages required for continuous operation (Figure 4-14).

Based on the new zeolitic membrane, a process of continuous DPC production is finally proposed, as shown in Figure 4-14.

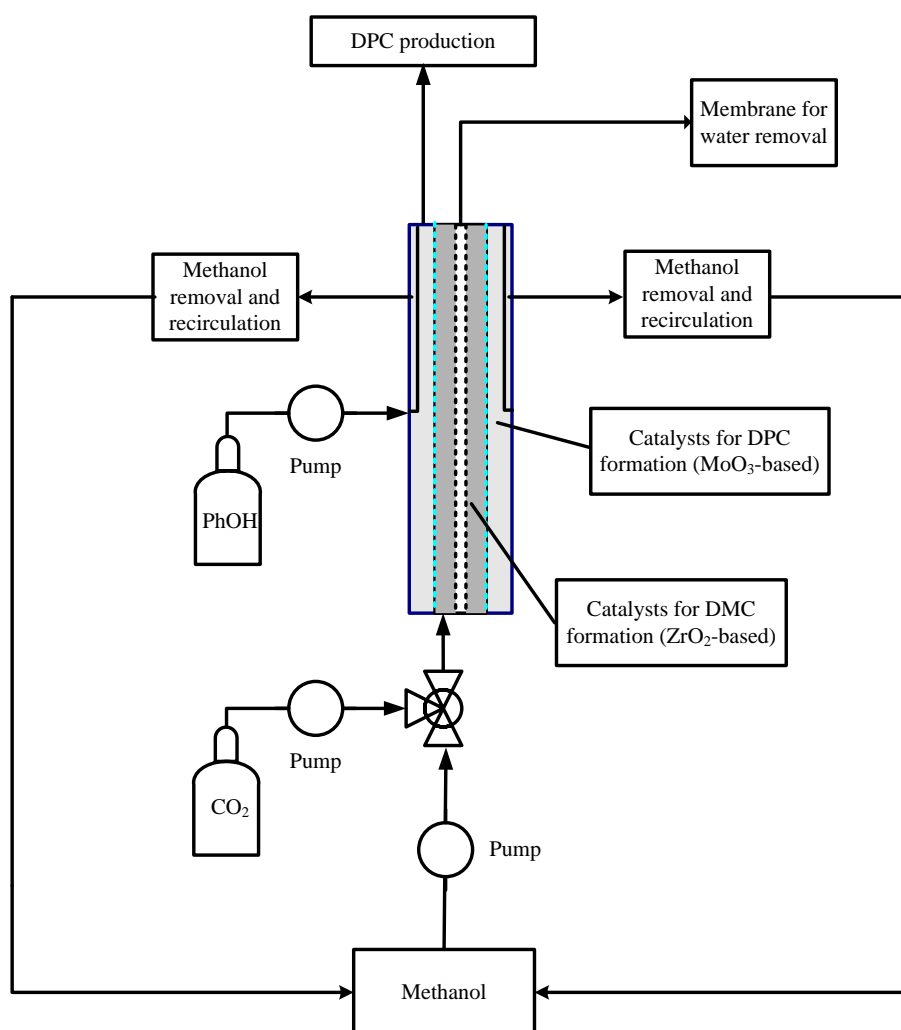


Figure 4-14 Schematic representation of an operational unit for the continuous DPC production based on membrane reactor

As proposed in Figure 4-14, methanol and CO₂ are first fed into the reactor. In the 1st step, ZrO₂-catalyzed DMC formation from methanol and CO₂ takes place. Simultaneously, the co-produced small amount of water in the reaction mixture is diffused and removed via the zeolitic membrane with high separation factor.^[32] As a result, high-purity DMC is produced. In the presence of phenol introduced in the 2nd part of the reactor, the formation of MPC is enabled on the active surface of MoO₃ catalyst. To reduce thermodynamic constrain of the transesterification reaction, methanol is separated from the reactor and recycled. Finally, the outcome of the operation is high concentration of high-purity MPC, which is in the last reaction step, can be readily converted into DPC via disproportionation. One main advantage of the proposed operational unit is the high energy-efficiency of the process, since the temperature gradient among different reaction / separation zones is very small thus an internal heat exchange demanding high energy consumption is not required.

4.4 References

- [1] H. Babad, A. G. Zeiler, *Chem. Rev.* **1973**, 73, 75
- [2] U. Romano, R. Tesei, M. M. Mauri, P. Rebora, *Ind. Eng. Chem. Prod. Res. Dev.* **1980**, 19, 396
- [3] K. Tomishige, T. Sakaihorii, Y. Ikeda, K. Fujimoto, *Catal. Lett.* **1999**, 58, 225
- [4] K. Tomishige, Y. Furusawa, Y. Ikeda, M. Asadullah, K. Fujimoto, *Catal. Lett.* **2001**, 76, 71
- [5] M. Aresta, A. Dibenedetto, E. Fracchiolla, P. Giannoccaro, C. Pastore, I. Pápai, G. Schubert, *J. Org. Chem.* **2005**, 70, 6177
- [6] J. Weitkamp, L. Puppe, *Catalysis and Zeolites: Fundamentals and Applications*, Springer, Berlin, **1999**

- [7] D. W. Breck, W. G. Eversole, R. M. Milton, *J. Am. Chem. Soc.* **1956**, 78, 5963
- [8] R. M. Milton, *US Patent*, **1959**, 4534947
- [9] S. M. Ben-Shebi, *Chem. Eng. J.* **1999**, 74, 197
- [10] M. Goyal, R. Nagahata, J. Sugiyama, M. Asai, M. Ueda, K. Takeuchi, *Polymer*, **1999**, 40, 3237
- [11] Q. Wang, R. Huang, *Tetra. Lett.* **2000**, 41, 3153
- [12] C. F. Fillers, K. H. Maness, D. J. Olsen, C. E. Outlaw, B. T. Smith, *WO Patent* **2000**, 29366
- [13] One should note that methanol was used as internal standard for determination of water amount in the liquid mixtures. However, methanol was also able to be retained in the zeolites, leading to experimental deviation. Fortunately, it was further stated that this deviation has no significant influence on the final conclusion, as the simultaneously retained methanol amount was below 5 wt. % of the initial methanol amounts (maximum methanol uptake on LTA zeolites is *ca.* 200 mg g⁻¹ determined by intrinsic methanol adsorption isotherm, so that the retained methanol cannot be more than 1 g, which was under 5 % compared to the initial methanol amount).
- [14] G. K. Chuah, S. Jaenicke, B. K. Pong, *J. Catal.* **1998**, 175, 80
- [15] R. M. Barrer, *Zeolites and clay minerals as sorbents and molecular sieves*, Academic Press, London, **1978**
- [16] J. Kärger, M. Bülow, W. Schirmer, *Zeitschrift für Physikalische Chemie* **1975**, 256, 144
- [17] P. W. Atkins, *Physical Chemistry*, 15th edition, Oxford University Press, **1994**
- [18] M. A. Pacheco, C. L. Marshall, *Energy Fuels*, **1997**, 11, 2
- [19] R. Maachi, M. J. Boinon, J. M. Vergnaud, *J. Chim. Phys. Phys.-Chim. Biol.* **1978**, 75, 116
- [20] N. Tessa, B. Tyburce, G. Joly, *J. Chim. Phys. Phys.-Chim. Biol.* **1991**, 88, 603
- [21] J. Kärger, D. M. Ruthven, *Zeolites* **1989**, 9, 267

-
- [22] L. E. Cohen, R. Kahn, F. Mezei, *J. Chem. Soc. Faraday Trans. I* **1983**, 79, 1911
- [23] D. M. Ruthven, S. Brandani, *Membr. Sci.* **2000**, 6, 187
- [24] G. Mirth, J. A. Lercher, *J. Catal.* **1993**, 139, 24
- [25] L. V. C. Rees, *Stud. Surf. Sci. Catal.* **1994**, 84, 1133
- [26] J. Haubrock, M. Raspe, G. F. Versteeg, H. A. Kooijman, R. Taylor, J. A. Hogendoorn, *Ind. Eng. Chem. Res.* **2008**, 47, 9854
- [27] G. E. Harrison, A. J. Dennis, M. Sharif, *WO Patent*, **1992**, 18458
- [28] M. V. Opanasenko, M. V. Shamzhy, C. Jo, R. Ryoo, J. Čejka, *ChemCatChem* **2014**, 6, 1919
- [29] M. Misk, G. Joly, P. Magnoux, M. Guisnet, S. Jullian, *Microporous Mesoporous Mater.* **2000**, 40, 197
- [30] S. A. Anderson, S. Manthata, T. W. Root, *Appl. Catal. A: Gen.* **2005**, 280, 117
- [31] B. Peng, H. Dou, E. E. Ember, J. A. Lercher, *EP Patent*, **2016**, 16000363.8
- [32] B. Peng, H. Dou, E. E. Ember, J. A. Lercher, *EP Patent*, **2016**, 16000517.9
- [33] K. Sato, K. Aoki, K. Sugimoto, K. Izumi, S. Inoue, J. Saito, S. Ikeda, T. Nakane, *Microporous Mesoporous Mater.* **2008**, 115, 184
- [34] N. Wang, Y. Liu, A. Huang, J. Caro, *Microporous Mesoporous Mater.* **2015**, 207,

4.5 Appendix

4.5.1 XRD patterns of LTA zeolites

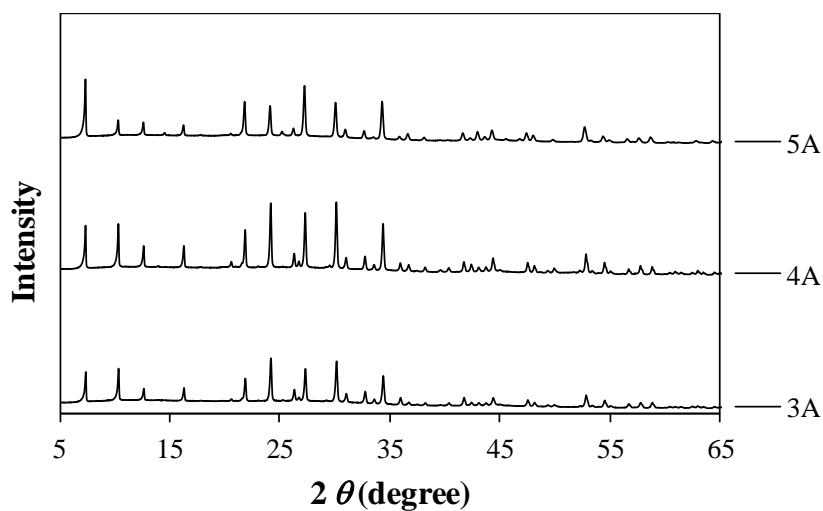


Figure 4-15 XRD patterns of all LTA zeolites

4.5.2 Chemical composition of LTA zeolites

Table 4-8 Elemental composition of LTA zeolites

Zeolites	Composition formula
3A	$\text{K}_{4.65}\text{Na}_{6.88}\text{Al}_{11.53}\text{Si}_{12.47}\text{O}_{48}$
4A	$\text{Na}_{11.68}\text{Al}_{11.68}\text{Si}_{12.32}\text{O}_{48}$
5A	$\text{Ca}_{7.79}\text{Na}_{7.83}\text{Al}_{11.72}\text{Si}_{12.28}\text{O}_{48}$

Chapter 5

Summary

Summary

Innovative pathways for sustainable DPC production without the usage of highly toxic and corrosive reagents are required. In order to fulfill the demands of green chemical production, a two-step reaction pathway has been proposed, combining methanol carboxylation to dimethyl carbonate (DMC) followed by its transesterification with phenol, where CO₂ is used as C₁ building block. The research conducted for catalyst development and considerable efforts dedicated to shift the thermodynamic equilibrium towards enhancement of product yield are identified as the two major objects in the present thesis.

The rate of ZrO₂-catalyzed DMC formation from methanol and CO₂ has been considerably improved by using newly developed catalysts. Homogeneous distribution of the new active sites created by heteroatom insertion on a highly crystalline ZrO₂ surface was proved to have an important impact on the optimization of the catalyst performance. It has been shown that new basic active sites considerably favor CO₂ adsorption and activation on the surface. Following methanol adsorption and formation of reactive methoxide species, monomethyl carbonate, a key intermediate, is formed, via a reaction with a surface bicarbonate or carboxylate. Higher activity of MgO-ZrO₂ catalyst is attributed to the higher CO₂ coverage caused by stronger basic sites as well as to the higher efficiency of nucleophilic attack from oxygen to carbon.

Active nanocrystalline α -MoO₃ supported on SiO₂ was synthesized and tested for transesterification of DMC with phenol. Raman spectroscopy enabled to distinguish among terminal Mo=O sites, Mo-O-Mo and Mo-(O)_n-Mo ($n > 1$) units. The surface coordinatively unsaturated Mo-O-Mo unit, stabilized on an orthorhombic crystal lattice, is responsible for the catalytic transesterification between phenol and DMC.

Based on the observed negative reaction order of phenol, a Langmuir-Hinshelwood mechanism with competitive adsorption of two reactants is proposed. Results from detailed *in-situ* spectroscopic measurements further support these mechanistic assumptions and enable to propose a reaction sequence that would account for MPC formation, a crucial intermediate in the process of DPC synthesis.

Selective water removal by using solid state zeolitic sorbents is an efficient approach for yield enhancement of DMC formation from methanol and CO₂, which is thermodynamically not favored. Compared to water, the diffusion of methanol is more severely influenced by temperature on LTA zeolites, indicated by observed higher temperature dependence of intra-crystalline methanol diffusion. In contrast, water diffusion on different LTA zeolites varies only in limited extent. At different temperatures, the ratio of water diffusion coefficient to methanol diffusion coefficient directly reflects the ability of selective water removal from methanol of LTA zeolites. The highest value of above ratio is achieved with 3A zeolite operated at -25 °C. A dehydration unit operated at low temperature with the use of LTA zeolite is applied for shifting thermodynamic equilibrium of DMC formation accordingly and one order of magnitude enhancement on DMC yield is obtained. Similar concept is applied for transesterification of DMC with phenol. 4A zeolite is the most suitable candidate as *in-situ* methanol scavenger, for its excellent methanol uptake capacity and high diffusion rate as well as for its chemical inertness. As a result, an overall transesterification product yield is achieved over 50 %. Finally, based on the newly developed zeolitic membrane, a continuous process model of the entire reaction route is proposed. The above study allows further developments of sustainable DPC production.

Curriculum vitae

Bo Peng was born on 20th October 1985 in Beijing, P. R. China. After accomplishing his high school education in 2nd High School attached to Beijing Normal University (Beijing, China) in 2003, he started the study in *Department of Materials Science and Engineering* at *Tsinghua University* (Beijing, China) and received his bachelor degree in 2007. Starting from September 2007, he moved to *School of Chemistry and Chemical Engineering* at *Nanjing University* (Nanjing, China), pursuing his master study with the focus of advanced materials and applied catalysis, under the supervision of Prof. Yi Chen and Prof. Dr. Weiping Ding. In 2010, he received his master degree after defending the thesis titled “*Exploration based on conventional ammonia synthesis catalysts*”. From the end of 2010, he started the research in *Chair II of Chemical Technology* at *Technical University of Munich* (Munich, Germany) on the topic of innovative pathways towards sustainable diphenyl carbonate synthesis, under the supervision of Prof. Dr. Johannes A. Lercher. Some representative results of the work in Munich are summarized in the present thesis.

Publications and patents

1. N. K. Gupta, B. Peng, E. E. Ember, J. A. Lercher, γ -Al₂O₃ catalyzed Cl₂ activation and phosgene synthesis. To be submitted to *ACS Catal.* **2016**
2. B. Peng, N. K. Gupta, E. E. Ember, J. A. Lercher, Mechanistic insight on transesterification of dimethyl carbonate with phenol over MoO₃ catalysts. To be submitted to *ACS Catal.* **2016**
3. B. Peng, H. Dou, H. Shi, E. E. Ember, J. A. Lercher, High yield direct synthesis of dimethyl carbonate from methanol and CO₂. To be submitted to *Angew. Chem. Int. Ed.* **2016**
4. N. K. Gupta, B. Peng, G. L. Haller, E. E. Ember, J. A. Lercher, Nitrogen modified carbon nano-materials as stable non-metal catalysts for phosgene synthesis. To be submitted to *ACS Catal.* **2016**
5. B. Peng, N. K. Gupta, G. L. Haller, E. E. Ember, J. A. Lercher, Rate enhancement of dimethyl carbonate formation from methanol and CO₂ over ZrO₂-based catalysts by heteroatom doping. To be submitted to *Green Chem.* **2016**
6. B. Peng, H. Dou, E. E. Ember, J. A. Lercher, Preparation and use of zeolitic membranes for selective removal of water. *EP Patent*, **2016**, 16000517.9
7. B. Peng, H. Dou, E. E. Ember, J. A. Lercher, Preparation and use of zeolitic sorbents for selective removal of water. *EP Patent*, **2016**, 16000363.8
8. L. Wang, B. Peng, L. Peng, X. Guo, Z. Xie, W. Ding, Mesoporous Bi-Mo-O catalyst: correct structure leading to high performance. *Sci. Rep.* **2013**, 3, 2881
9. L. Wang, B. Peng, X. Guo, W. Ding, Y. Chen, Ferric molybdate nanotubes synthesized based on Kirkendall effect and their catalytic property for propene epoxidation by air. *Chem. Commun.* **2009**, 12, 1565

Congress contributions

1. B. Peng, E. E. Ember, J. A. Lercher, Mechanistic understanding on MoO₃-catalyzed transesterification between phenol and dimethyl carbonate. *12th European Congress on Catalysis*, Kazan, Russia, **2015**
2. B. Peng, E. E. Ember, J. A. Lercher, Mechanistic understanding towards diphenyl carbonate synthesis over metal oxide catalysts. *48. Jahrestreffen Deutscher Katalytiker*, Weimar, Germany, **2015**
3. B. Peng, E. E. Ember, J. A. Lercher, Mechanistic understanding of dimethyl carbonate synthesis from methanol and CO₂ over ZrO₂-based catalysts. *46. Jahrestreffen Deutscher Katalytiker*, Weimar, Germany, **2013**
4. B. Peng, E. Ember, J. Lercher, Innovative pathways to sustainable dimethyl carbonate production - process optimization and catalysts development. *45. Jahrestreffen Deutscher Katalytiker*, Weimar, Germany, **2012**
5. B. Peng, S. Meier, E. Ember, J. Lercher, Innovative pathways towards sustainable polycarbonate production. *Joint Workshop on Energy and Sustainability*, Garching, Germany, **2011**
6. B. Peng, N. Liu, W. Ding, Y. Chen, Composite nitride catalyst Fe-Al-N for ammonia synthesis. *12th National Youth Congress on Catalysis*, Jinhua, China, **2009**
7. L. Wang, B. Peng, X. Guo, W. Ding, Preparation of ferric molybdate nanotubes based on Kirkendall effect. *14th National Congress on Catalysis*, Nanjing, China, **2008**